Conformational and UV Photochemistry Studies of Amino Acids in Matrix-Isolation FTIR Spectroscopy

by

Cindy Shin Yi Toh

B.Sc. Chemistry, The University of British Columbia, 2012

A THESIS SUBMITTED IN PARTIAL FULFILLMENT
OF THE REQUIREMENTS FOR THE DEGREE OF

Master of Science

in

THE FACULTY OF GRADUATE AND POSTDOCTORAL STUDIES
(Chemistry)

The University of British Columbia
(Vancouver)

July 2016

Abstract

The existence of amino acids in interstellar space has been a hot topic among researchers in astronomical science because of the biological molecules relevance to the origin of life. One of the most popular tool employed for the study of amino acids in relation to interstellar chemistry is matrix-isolation spectroscopy, as the cold and isolated environment provided by the matrix crystal mimics various astrophysical media such as interstellar ice. In the presented work, we reported the conformational and UV photochemistry studies of β-alanine and α-alanine via matrix-isolation Fourier transform infrared (MI-FTIR) spectroscopy in solid parahydrogen. These are the first time β-alanine and α-alanine being registered in parahydrogen matrices, and the crystal has proven to be a more beneficial host over argon matrices for conformational analysis and *in-situ* UV irradiation experiment. Our claim on the superiority of solid parahydrogen is supported by the detection of high energy amino acids conformers in solid parahydrogen, in which are previously unobserved in noble gas matrices. These conformers are conformer III for β-alanine, and conformer VI and V for α-alanine. As for UV irradiation experiment in solid parahydrogen, we obtained predominantly conformational change for β-alanine. However, α-alanine underwent complete photodestruction to give CO_2 and other unknown photoproducts we are attempting to identify. Finally, we have succeeded in producing β-alanine zwitterions in parahydrogen matrix, and reported the first formation and detection of amino acid zwitterions in solid parahydrogen.

Preface

All the work presented henceforth was conducted under the supervision of Dr.Takamasa Momose in the Chemistry Department of University of British Columbia, Point Grey campus.

The parahydrogen converter used in this project was designed and built in the year 2008 by Dr.Momose and his associates Dr.Brian A. Tom, Mr.Siddharta Bhasker, and Dr.Benjamin J. McCall from University of Illinois, and Dr.Yuki Miyamoto from University of British Columbia. The figures of the converter in Chapter 3. Figures 3.1 and 3.2 are used with the permission from Tom *et al.* [1] on the groups detailed publication of the converter design. The cryogenic sample chamber, the Knudsen cell, and the housing for deuterium lamp used in this project were designed and built by our lab technician, Mr.Pavle Djuricanin. The FTIR spectrometer used in the project is from the company Bruker Cooperation, and was assembled and calibrated by Dr.Momose and Mr.Djuricanin in the year 2011.

Ms.Angel Ying-Tung Wong and I were the lead investigators for the projects located in Chapter 5. Sections 5.1 and 5.2. where we designed the experiments, collected the data, performed the major analysis and quantum computations, and composed the manuscripts, with equal responsibilities. Ms.Ellen Chua has assisted us in some of the computational works for the projects. A version of Chapter 5. Section 5.1 has been published [2], and the preliminary analysis of the project was included in Ms.Wong's bachelor's thesis [3]. A journal manuscript of the result from Chapter 5. Section 5.2 has also been written for publication in the near future [4].

The projects presented in Chapter 5. Sections 5.3 and 5.4 were my original works. I was responsible for the major areas of experimental design, data collection, spectra analysis, quantum calculations, and manuscript composition. Mr.Brandon Moore has assisted me in some computation and analysis works for these projects.

The project described in Chapter 7. Section 7.2 was a collaboration work with Dr.Shang-Chen Huang from National Chiao Tung University. The liquid He cooled cryogenic sample chamber were designed and built by Dr.Momose, and was modified by Mr.Djuricanin. Dr.Huang and I has input some set-ups modification and reconstruction ideas, and were responsible for the experimental design, data collection, spectra analysis, quantum calculations, and manuscript composition, with equal contributions. Ms.Janet Leung has assisted us in some computation and analysis works for this project.

Table of Contents

List of Tables

List of Figures

List of Abbreviations

B3LPY/6-31++G** Becke 3-Parameter (Density Functional Theory) with 6-31G Split Valance Basis Set plus Diffuse Functions plus Polarization

B3LYP/6-311++G** Becke 3-Parameter (Density Functional Theory) with 6-311G Triple Split Valance Basis Set plus Diffuse Functions plus Polarization

B3LYP/aug − cc − p**VDZ** Becke 3-Parameter (Density Functional Theory) with an Augmented Double-Zeta Basis Set

B3LYP/aug − cc − p**VTZ** Becke 3-Parameter (Density Functional Theory) with an Augmented Triple-Zeta Basis Set

BaF$_2$ Barium Fluoride

ccm Cubic Centimetre per Minute

CCSD(T)/aug − cc − p**VTZ** Coupled Cluster Calculation with Single and Double Subtitutions from Hartree-Fock plus Triple Excitations Non-Iteratively plus an Augmented Triple-Zeta Basis Set

CFI Canadian Foundation for Innovation

CRUCS Center for Research on Ultra-Cold Systems

DC Direct Current

DCN Deuterated Hydrogen Cyanide

ESR Electron Spin Resonance

fcc Face-Centered Cubic

FTIR Fourier Transform Infrared

H-bond Hydrogen-Bond

H$_2$C=NH Methylimine

H$_3$C-CH$_2$-NH$_2$ Ethylamine

HCN Hydrogen Cyanide

hcp Hexagonal-Closed Packed

He-Ne Helium-Neon

HF/4-31G Hartree-Fock Theory with a 4-31G Split-Valence Basis Set

HF/6-31G* Hartree-Fock Theory with a 6-31G Split-Valence Basis Set plus Polarization

HF/6-31+G* Hartree-Fock Theory with a 6-31G Split-Valence Basis Set plus Diffuse Functions plus Polarization

HWHM Half Width at Half Maximum

I Nuclear Spin Angular Momentum

IR Infrared

J Rotational Quantum Number

KBr Potassium Bromide

LA-MB-FTMW Laser-Ablation Molecular-Beam Fourier Transform Microwave

MCD Magnetic Circular Dichorism

MCT Mercury Cadmium Telluride

MgF_2 Magnesium Fluoride

MI Matrix-Isolation

MI-IR Matrix-Isolation Infrared

MI-FTIR Matrix-Isolation Fourier Transform Infrared

MIR Mid-Infrared

MP2/6-31+G* Møller-Plesset Perturbation Theory with 6-31G Split Valance Basis Set plus Diffuse Functions plus Polarization

MP2/6-311++G** Møller-Plesset Perturbation Theory with 6-311G Triple Split Valance Basis Set plus Diffuse Functions plus Polarization

MP2/aug – cc – p**V5Z** Møller-Plesset Perturbation Theory with an Augmented Quintuple-Zeta Basis Set

MP2/aug – cc – p**VDZ** Møller-Plesset Perturbation Theory with an Augmented Double-Zeta Basis Set

MP3/aug – cc – p**VQZ** Møller-Plesset Perturbation Theory at the Third Order with an Augmented Quadruple-zeta Basis Set

NBS National Bureau of Standards

NIR Near-Infrared

NIST National Institute of Standard and Technology

OFHC Oxygen Free High Conductivity

PES Potential Energy Surface

ppm Parts per Million

p$\mathbf{H}_2$ Parahydrogen

RHF/6-31G* Restricted Hartree-Fock Theory with a 6-31G Split-Valence Basis Set plus Polarization

SLM Standard Liter per Minute

UV Ultraviolet

VEEL Vibrational and Electronic Energy Level

vs Versus

ZPE Zero-Point Energy

Acknowledgements

I would like to thank everyone who has helped me over the past couple years on my work here at UBC. Thank you to Dr.Takamasa Momose for taking me on as a student and for providing me with constant support and guidance throughout my work here. Special thanks to my partner in experiment, Ms.Angel Ying-Tung Wong, for being the most remarkable researcher I have ever work with, and our lab technician, Mr.Pavle Djuricanin for designing, building, and maintaining most of the machines used for this project. Thank you to Dr.Jun Miyazaki, Dr.Watheq Al-Basheer, and Dr.Shang-Chen Huang for their expertise advice and mentorship on the field of my work. Thank you to my students, Ms.Ellen Chua, Mr.Brandon Moore, and Ms.Janet Leung for assisting me in the analysis and computational works for this project. Thank you to Mr.Tony Mittertreiner and Mr.Milan Coschizza for their technical support on the FTIR spectrometer. Thank you to all my fellow colleagues in the Momose Group, especially Mr.Thomas Prescott, Dr.Eric Miller, Dr.Yang Liu, Dr.Manish Vashihta, Dr.Omid Nourbakhsh, Dr.Mario Michan, and Dr.Polly Yu, with whom I have the honoured to worked alongside during my academic years in the laboratory. And lastly, thank you to my parents, who have supported me throughout my years of education, both morally and financially.

This research was supported by an NSERC Discovery Grant and funds from CFI to the Centre for Research on Ultra Cold Systems (CRUCS) at UBC.

Chapter 1

Introduction

Amino acids have been subjected to multiple fundamental researches due to their importance in basic anatomy, and their relevance to the origin of life. Amino acids are the building blocks of biological molecules, prompting the investigation of their physical and chemical properties essential for the understanding of their functions in biological system. In addition, the existence of amino acids in interstellar space has been discussed for many years, but it is still under intense debate. The search of glycine, the simplest amino acid, in interstellar space is a good example of the controversies encountered by this field of exploration. In 2003, Kuan *et al.* [5] claimed the observations of 27 glycine lines in 19 different millimeter-wave bands from three astronomical sources, Sgr B2(N-LMH), Orion KL, and W51 e1/e2. The discovery, however, was later disconfirmed by Snyder *et al.* [6] in 2004 with their rigorous but unsuccessful attempt on verifying Kuan *et al.* reported glycine assignments, and by Cunningham *et al.* [7] in 2007 with their fruitless detection of interstellar glycine in the Sgr B2(N-LMH) and Orion KL using the Mopra Telescope.

The origin and formation of interstellar amino acids are particularly hot topics of scientific investigations. Several extraterrestrial amino acids have been found in various type of carbonaceous chondrite meteorites [8–12], with over eighty distinct amino acids have been identified in Murchison meteorite alone [13]. However, the amino acids exact location of origin and the mechanism of synthesis are yet to be discovered. Some researchers have suggested the formation of these organic compounds through Strecker-type synthesis on the meteorite parent body, in which involved the reaction of hydrogen cyanide, ammonia, and aldehyde in the aqueous astrophysical media [14, 15]; while others argued that interstellar amino acids are the products of interstellar ion-molecule reactions [16, 17].

Another focus of investigations on interstellar amino acids involve the stability of these organic compounds in extraterrestrial environments, specifically their photostability against UV radiation. The effect of UV radiation on amino acids is one of the keys for their search in interstellar space. Amino acids might undergo chemical degradation, racemization [18], or conformational change [19] when being exposed to UV rays. Several research groups have demonstrated that gas phase amino acids might be highly susceptible to UV photodestruction, and would most likely not survive in the space medium in which strong UV radiation exists [20, 21]. However, the possibility of observing interstellar amino acids in their full forms should not be ruled out completely. Thus, it is especially essential to check the conformational behavior and racemization properties of amino acids upon UV-irradiation, and also identify the photoproducts resulting from the

photodecomposition of amino acids.

Matrix-isolation (MI) spectroscopy technique has been widely used for extraterrestrial prebiotic molecules studies due to its ability to stimulate conditions close to that of an extraterrestrial environment, such as in interstellar gas or on interstellar grains [20]. This high resolution spectroscopy technique allows for the observation of higher energy conformer molecules and intermediary photoproducts due to its capability of sustaining reactive molecules in the ice crystal [22]. Matrix-isolation method has also provided a simpler platform for researchers to conduct photochemistry experiments, by allowing *in-situ* irradiation of isolated sample trapped within the matrix cage [22].

For the work presented in this thesis, my collaborators and I had explored the conformational properties and UV photochemical behaviours of two simple amino acids, namely β-alanine and α-alanine, by employing matrix-isolation Fourier transform infrared (MI-FTIR) spectroscopy using parahydrogen as our matrix. We compared our findings in solid parahydrogen to those of argon matrix. We also attempted to produce and investigate these amino acids in their zwitterion forms using matrix-isolation method. The observed spectra and associated analysis were discussed in relation to interstellar chemistry.

Chapter 2

Background

2.1 Matrix-Isolation Spectroscopy

Matrix-isolation method involves the trapping of active molecules in solid matrix with inert properties [23]. The technique is achieved by rapid condensation of the mixed guest sample - host matrix gas onto a surface of cryogenic temperature [22]. Under this extremely cold temperature, the non-reactive matrix environment will inhibit diffusion of the molecules, keeping individual analyte encaged within the isolated pockets of the crystalline matrix, and preventing intermolecular interaction between the active molecules [23].

The incorporation of matrix-isolation method with infrared spectroscopy was first thought out by George C. Pimentel and his two colleagues, Eric Whittle and David A. Dows, in the early 1950's [23]. They theorized that inert solids, made out of rare gases and nitrogen, are transparent over a wide range of spectral region from the far infrared to the vacuum UV, allowing the direct infrared detection of the trapped molecule within the matrix. The group tested the application of matrix-isolation infrared (MI-IR) spectroscopy on unstable molecules, such as free radicals and reaction intermediates, and succeed in producing infrared spectra of the reactive samples with good quality [23]. The low temperature environment of the matrix evidently prohibits intramolecular reactions of the molecule with an appreciable amount of activation energies [22]. And with the absent of quantum diffusion, intermolecular interactions are minimized due to the isolation of analyte as mention above. With the lack of both intra- and intermolecular reactions, the lifetime of unstable molecules are lengthened, thus making the physical and chemical studies of the reactive species easily accessible through matrix-isolation spectroscopy techniques [22].

Soon after the development of MI-IR spectroscopy, Marilyn E. Jacox and Dolphus E. (Dick) Milligan expanded the study of free radicals in cold inert matrix at the Mellon Institute, and then under the Surface Chemistry Section at the National Bureau of Standards (NBS) [24]. From their researches, Jacox and Milligan realized the occurrence of limited atomic diffusion within the matrix media, which aids in stabilizing the encaged free radicals by migration of the lighter atoms through the matrix to react with other trapped species [25]. They also worked intensively on the photochemistry of free radicals in matrix environment, using lamps of vacuum UV-region as their irradiation sources [24]. Despite the early death her associate Milligan, Jacox, considered now as a pioneer in infrared spectroscopy, continued with their researches in

matrix-isolation. She extended the application of MI-IR spectroscopy to molecular ions [24, 26], and utilized the method to compile vibrational and electronic energy-level data of neutral and ionic polyatomic transient molecules under the VEEL project with the National Institute of Standard and Technology (NIST) [24, 27–29].

One of criticism received by researchers in matrix-isolation field is that the trapped species are not truly isolated or free due to some perturbation by the medium [30]. The interaction energy between the inert matrix host and the active guest molecule is minimal but non-zero, and will affect the structure and dynamics of the encaged molecule resulting in spectral shift [30, 31]. However, Jacox had addressed this drawback of matrix-isolation by comparing spectra of gas-phase spectroscopy to that of inert, rigid matrix, and found that the infrared absorption of the trapped active molecules in solid argon and neon appeared within 1 % of the corresponding gas-phase band centers [24, 31]. With this generalization, MI-IR spectroscopy has proved to be a step-up in gas-phase spectroscopy, allowing for the qualitative and quantitative spectral observations of gaseous sample with high accuracy.

Aside from its application on reactive species, matrix-isolation technique is also widely used in spectroscopy studies of stable molecules [22, 30]. Molecules trapped within inert matrices could be detected with a higher resolution as compared to other condensed phases and the vapour phase [22]. The lack of intermolecular interactions due to sample isolations in solid matrices results in a great sharpening of solute absorptions, giving spectra signals of smaller bandwidths than those obtained in the liquid and solid phases; whereas the absence of rotation within the matrix cages (with the exception of very small molecules) causes the bands to be much narrower as contrasted to gas phase absorptions. The low temperature itself is also contributing to the reduction in bandwidths, producing a more defined spectra than those taken at room temperature [22]. With the advantage of producing sharper signals, matrix spectral can be used to resolve near-degenerate bands, which overlap completely even in the gas phase or in dilute solution [22]. As matrix-isolation spectroscopy allows for more accurate vibrational assignments of near-degenerate fundamentals, the application is especially popular in conformational isomerism studies, where difference of vibrational frequencies between two or more conformers could be minuscule [22].

Matrix-isolation method is now used in various fields of spectroscopy, like vibrational, electronic (absorption and emission), MCD, ESR, and Mossbauer spectroscopy, just to name a few [22]. The technique is most widely coupled with infrared and Raman spectroscopy due to its ability of providing vibrational spectral with more detailed features than those taken in the liquid, solid, and gas phases, as mentioned above [22]. As for the matrix host, rare gases such as argon and neon are the predominant choices due to their chemical inertness and physical simplicity, as compared to molecular matrix like nitrogen [32, 33]. However, all combinations of spectroscopic tools and matrix materials have their own strengths and weaknesses, depending on the nature of the experiments. For our conformational isomerism studies of simple amino acids, we employed parahydrogen as our matrix host, and combined the matrix isolation application with FTIR spectroscopy. We believed that this combination, known as solid parahydrogen MI-FTIR spectroscopy, would give us vibrational spectra of the highest achievable resolution, allowing us to proceed with spectral assignments with the greatest confidence.

2.1.1 Fourier Transform Infrared (FTIR) Spectroscopy

The design of the optical pathway has produced a pattern known as an interferogram. This wave-like signal contains frequency information that would make up a time-domain infrared spectrum. However, spectroscopists prefer spectra of frequency-domain, which is easier to read and interpret than its time-domain counterpart. Thus, the creation of a mathematical operation called a Fourier transform, that can extract individual absorption frequencies from the interferogram and translate the obtained information from an intensity versus time plot to an intensity versus wavenumber (or wavelength) spectrum [34].

Fourier transform infrared (FTIR) spectrometer is based on the Michelson interferometer. The spectrometer is equipped with a beam splitter that splits the incoming IR beam into two beams of equal power intensity, and directs the separated beams to a movable and a fixed mirror, respectively. The movable mirror oscillates at a constant speed with a known position at all instant, giving consistently spaced periodic beams of varied path lengths upon each beam reflection. The two split beams are then being reflected back to the beam splitter, recombined as a beam of interference pattern, and sent through the sample towards the detector [35]. This dual mirror design allows for precise signal sampling and signal averaging, resulting in an overall more improved signal than that obtained by dispersive spectrometers [35].

A way to further improve the signal sampling and averaging aspects of a FTIR instrument is to incorporate two or three interferometers, rather than just one, into the spectrometer. For a triple interferometer system arrangement, the instrument contains a laser-fringe reference system and a white-light system, on top of an IR system that carries the analytical information to produce the final interferogram [35]. The laser-fringe reference system consists of a He-Ne laser, and the system function is to provide sampling-interval information to the spectrometer. With a static cosine output wave from the laser feedback, the system gives highly reproducible and regularly spaced sampling interval. The laser signal is also used to control the motor-drive of the movable mirror, keeping the speed of oscillation to be at a constant level [35]. The white-light system is equipped with a tungsten source, and the purpose of the system is to trigger the start of data sampling for each sweep at a highly reproducible point. The system is arranged in a way that its zero retardation appears as a strong maximum at a position prior to that for analytical signal, indicating it as the starting point of a measurement sweep [35].

The instrument (Bruker, IFS 125HR) we employed for our experiment is a single beam FTIR spectrometer with a double interferometer system. Our FTIR spectrometer applies a He-Ne laser system to provide reference signal for acquiring data, and a IR source system to give the ultimate interferogram and to establish zero retardation [36]. The maximum in the IR interferogram could be considered as an excellent reference point, because it is the only point at which all wavelengths interfere constructively [35]. Figure 2.1 illustrated the design and optical pathway of our FTIR spectrometer.

FTIR spectrometer poses multiple advantages over dispersive infrared instruments, making it a preferable tool for infrared region analysis. The first advantage imposed by FTIR spectrometer is the throughput advantage. With fewer optical elements and no narrow width slits to attenuate the radiation beam, the radiant power reaching the detector in a FTIR instrument is much greater, thus producing better signal-to-noise ratio than that of dispersive instruments by more than an order of magnitude [35]. FTIR instrument provides extremely high resolving power and wavenumber reproducibility, revealing previously unsuspected

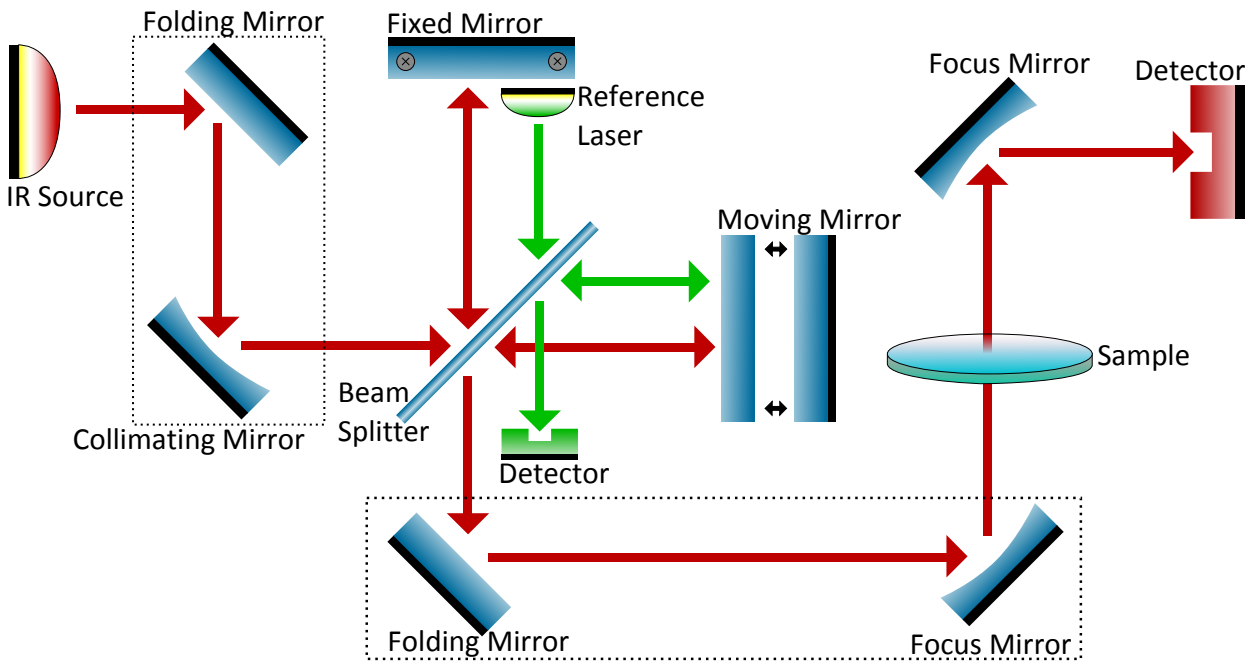

Figure 2.1: Set-ups and optical pathways of a Bruker FTIR spectrometer. The instrument consists of two interferometer systems, which are the IR system and the laser-fringe reference system. The red arrows indicate the path of the IR beam; whereas the green arrows indicate the path of the He-Ne laser beam.

fine structures on many spectra bands, and allowing for the determination of molecular signals with higher accuracy and precision [35]. As all the elements of the source reach the detector simultaneously in an FTIR spectrometer, the instrument possesses multiplex advantage, indicating a faster data collection time as compared to dispersive spectrometers [35]. Finally, FTIR spectrometer tends to be free from problem of stray radiation, as each IR frequency is chopped at a different frequency before being sent through for detection [35].

2.1.2 Solid Parahydrogen as Matrices

As previously mentioned, noble gases are most commonly used as matrix host for matrix-isolation spectroscopy due to their chemical inertness [32, 33]. However, rare gas matrices pose some disadvantages that make them not as practical to be applied in high resolution spectroscopy. One of these disadvantages is the observation of undesirable spectral broadening as a result of homogeneous and inhomogeneous interactions in the matrices [32, 33, 37, 38]. Homogenous line broadening arises from the weak but considerable perturbation of the isolated guest molecules on the surrounding matrix host atoms, due to the close physical proximity of the two in the rigid noble gas solid [22]; on the other hand, inhomogeneous line broadening is a consequence of the mixed hexagonal-closed packed (hcp) and face-centered cubic (fcc) caging structures of such matrices, in which the ratio of hcp to fcc structures can varies with the concentration of dopant and the procedure of deposition [22]. The matrix-guest interaction also manifests another major matrix effect, namely multiple trapping sites effect [22, 39]. Molecules occupy into a matrix cage through substitution pro-

cess via the removal of one or more matrix atoms, and more than often the amount of removed atoms varies among different substitution sites within the same matrix [22]. Even though the different trapping sites only differ slightly from each other, this effect still leads to the observation of multiple bands which could point to the same vibrational behaviour, thus further complicates the process of spectral analysis [22, 39]. In terms of photochemistry investigations in matrix environments, rare gas matrices inherently hard and rigid cage effect inhibits effective *in-situ* photolysis on the trapped species. This drawback often leads to the utilization of photoirradiation or photoexcitation techniques prior to the sample deposition step, which most likely causes complication to the system to be studied [32]. The limitation imposed by noble gas matrices on matrix-isolation spectroscopy, however, can be overcome by employing parahydrogen matrices.

Normal hydrogen consists of ortho- and parahydrogen in a ratio of three to one at room temperature [32, 40]. The two classes of molecular hydrogens arise from the symmetric and antisymmetric nuclear spin state of diatomic hydrogen, with orthohydrogen associates with spin angular momentum of one ($I = 1$) and rotational states of odd quantum number (J = odd), and parahydrogen is characterized by spin angular momentum of zero ($I = 0$) and rotational states of even quantum number (J = even) [32]. As the smallest mass molecule, hydrogen possesses a large rotational constant, giving an exceptionally big energy gap between the first excited and the ground rotational states for both ortho- and parahydrogen. Therefore, at cryogenic temperature as in solid matrix, ortho- and parahydrogen exist exclusively in their rotational ground states, which is $J = 1$ and $J = 0$, respectively [32]. With the spherical nature of its rotational ground state, parahydrogen has a permanent multipole moment of zero, making it behaves electrostatically as a noble gas atom [32]. On the other hand, orthohydrogen has a permanent quadrupole moment of the lowest multipole moment as a result of its rotational ground state anisotropic nature in charge distribution [32, 40]. From a spectroscopic point of view, the presence of orthohydrogen is unwanted, as the inhomogeneity of internal electrostatic field implied by orthohydrogen would lead to undesirable spectral line broadening [32, 37]. Fortunately, the transitions between odd and even rotational states are forbidden, making it possible to prepare and keep sample of highly pure parahydrogen for high resolution matrix-isolation spectroscopy [40]. Moreover, the concentration of thermal equilibrate orthohydrogen appears to decrease with decreasing temperature, with approximately 75 % at room temperature, 0.4 % at the boiling point of liquid helium (20.28 K at 1 atm), and down to 0.0045 % at the triple point of hydrogen (13.8 K). Thus, the purity of parahydrogen can be hyped up to more than 99.995 % by using an ortho-parahydrogen converter operating at a temperature of 13.8 K and lower [32]. However, the conversion of ortho- to parahydrogen is slow by itself. Therefore, magnetic catalysts are often used to apply magnetic perturbation on the cooled hydrogen sample and speed up the interconversion rate between the two nuclear spin angular momenta [32].

In 1989, Okumura, Chan, and Oka discovered the linewidth of $J = 6 \leftarrow 0$ transition is as narrow as 0.003 cm^{-1} HWHM in 99.8 % pure solid parahydrogen [41], which is much smaller than the Doppler-broadened and Dicke-narrowed spectral lines of gaseous hydrogen by one order of magnitude [38]. Their discovery took the field of spectroscopy by surprise as such large ΔJ rotational transitions are highly forbidden in gas phase, better yet with such high resolution observation [38]. Following the work of Okumura *et al.*, the exploration on spectral linewidth of solid parahydrogen was extended into impurities doped parahydrogen experiments, and the sharpest spectral lines observed thus far are from the rotation-vibration transitions of

deuterated hydrogen in parahydrogen matrices, with linewidth as narrow as 2 MHz (= 0.0000667 cm^{-1}) HWHM [42]. The breakthrough achievement of Okumura and his colleagues has thus revolutionized the utilization of solid parahydrogen in high resolution matrix-isolation spectroscopy, as the technique allows for the study of intermolecular and crystal-field interactions with exceptional clarity and precision, indicating the solid to be a superb medium over other gas matrix alternatives [38].

What makes solid parahydrogen so remarkable is its categorization as a quantum crystal [32, 38, 40]. Parahydrogen molecules are assembled by van der Waals forces into a crystal of purely hcp structure belonging to the D_{3h} point group. The nearest neighbour distance, *i.e.*, lattice constant, of the crystal structure is 3.783 Å, with a large zero-point lattice vibrational amplitude of approximate 18 % of the lattice constant. Such large zero-point motion causes quantum effect to dominate over classical lattice dynamic [40]. As quantum solid of exceptionally large intermolecular distance as compared to the atomic distance of other noble gas crystals (*e.g.*, Ne = 3.16 Å, Ar = 3.76 Å), solid parahydrogen supplies more free space to the guest molecules which in term causes weaker guest-host interaction, resulting in sharper spectral lines than those of rare gas matrices [37]. The pure hcp structure of solid parahydrogen offers a homogeneous environment for the trapped sample, eliminating inhomogeneous line broadening effect which arise from the mixed hcp and fcc structural arrangement in rare and other molecular gas matrices [37]. Parahydrogen matrix is also free from multiple trapping sites effect due to its quantum properties. The large zero-point lattice vibration amplitude of parahydrogen allows for self-reparation of defected crystal around the trapped analyte, providing the same trapping site features spanning across the whole matrix [37].

In addition, the spacious and less-perturbative parahydrogen matrix allows the encaged molecules to have almost free vibrational and rotational quantum states, opens up to the possibility of trapping and stabilizing higher energy states molecules [32, 38]. The energy density of solid parahydrogen is relatively dispersed for a molecular solid due to its exceedingly large rotational constant of 60.853 cm^{-1}, fundamental vibrational frequency of 4401.2 cm^{-1}, first excited electronic energy of 91700 cm^{-1}, and Debye temperature of 100 K ($\simeq$ 70 cm^{-1}), as compared to the parameters of other molecules [40]. These features further prolong the lifetime of excited molecules encaged in solid parahydrogen by bringing down the reactive species' relaxation process to an extraordinarily slow rate [32].

Lastly, the spacious characteristic of solid parahydrogen has featured the matrix as a soft medium opposing the hard and rigid non-quantum solids such as rare gases [32]. The large lattice constant and amplitude zero-point lattice vibration experienced in parahydrogen crystal also results in a higher than usual value for compressibility χ_T (defined as $\chi_T = -\frac{1}{v}(\delta V/\delta P)_T$) of approximately 50×10^{-10} Pa^{-1} at temperature below 5 K [40]. Moreover, highly pure parahydrogen crystal appears to have exceptionally large thermal conductivity value, with approximately 50 $Wm^{-1}K^{-1}$ for a sample of 0.2 % orthohydrogen at liquid helium temperature [40]. The soft and compressible features of parahydrogen matrix has thus make it the most suitable medium for *in-situ* photochemistry studies, as the photoproduct fragments can be separated easily via diffusion, and the separated fragments are quickly froze out by the high thermal conductivity nature of the quantum solid [32].

2.2 Conformational Isomerism Studies of Amino Acid with Matrix-Isolation Spectroscopy

Spectral bands of molecular conformers often differ by only a few wavenumbers. Therefore, a spectroscopy technique of high resolution is required to perform qualitative and quantitative conformational analysis on a molecule. Matrix isolation infrared (MI-IR) spectroscopy is one of the most powerful tools for conformational isomerism studies [22]. The cryogenic and inert matrix environment rapidly cools the sample mixed with the matrix gases upon contact with the cold window, preventing equilibration of the conformational mixture with energy barrier higher than 3 6 kJ·mol^{-1}, thus preserving the gas phase equilibrium composition of the sample that is present prior to deposition [43, 44]. As mentioned previously (see Section 2.1), MI-IR spectroscopy is capable of producing high resolution spectra with exceptionally sharp bands, resolving the typically overlap spectra signals of two and more conformers when taken in gas, liquid, or solid phase [22]. However, despite the high resolution provided by MI-IR spectroscopy, conformational spectra still suffer from superposition of bands, appearing as unresolved low intensity signals and shouldering peaks. Nonetheless, these congested bands can be distinguished by altering the conformational ratio of the trapped molecule with techniques such as matrix annealing [19, 43, 45, 46], *in-situ* photoirradiation [2, 19, 47–51], and sample deposition temperature variation [4, 52–54].

Numerous conformational studies in noble gas matrices have shown to be effective. Nevertheless, rare gases are not the best host materials for conformational isomerism analysis with MI-IR spectroscopy because of the varies matrix effect drawbacks imposed by the non-quantum solids, as highlighted in the previous Section 2.1.2 . Moreover, different matrices have been shown to have different capabilities in capturing the gas phase conformational equilibrium population of a system [2, 4, 53, 55, 56]. In a set of xenon, krypton, and argon matrices, the ability of each type of matrix to maintain the gas phase population was found to increase with decreasing atomic radii and mass [56]. In fact, our group has observed a complete depletion of some high energy conformers in argon matrices as a result of collisional relaxation imposed by the bulky argon gas atoms to the relatively unstable molecular conformers [2, 4] (see Sections 5.1 and 5.2). Subsequently, the use of inert gases as matrix materials could lead to a loss of conformational information, as the produced results might deviate from the actual gas phase conformational equilibria of a molecule.

Solid parahydrogen might come out as a better contender against rare gas matrices for conformational isomerism studies with MI-IR spectroscopy. Because of the quantum nature of solid parahydrogen, the vibrational spectra provided by solid parahydrogen MI-IR spectroscopy appear to be less complex than those by noble gas matrices, free from multiple trapping sites and spectral line broadening effects (see Section 2.1.2). In addition, parahydrogen matrix is expected to be more prominent in stabilizing higher energy states due to its small molecular size and light mass. In a conformational study of acetylacetone in solid parahydrogen, a higher abundance of keto/enol ratio was observed in solid parahydrogen than in rare gas matrices, in which the keto-form is the less stable state between the enol and keto tautomers of the sample [55].

Even though solid parahydrogen seems like a more suitable medium, most, if not all, of the conformational composition studies of amino acids with MI-IR spectroscopy were achieved using classical noble gas matrices. With the outstanding advantages provided by parahydrogen matrices, we have implored the

worth to reinvestigate the conformational stability of amino acids using solid parahydrogen MI-IR spectroscopy, and we started our case study with two of the simplest amino acids, namely β- and α-alanine. We also attempted to extend our investigation on the zwitterion forms of simple amino acids. The following subsections highlighted some previous computational and experimental works done on the conformational isomerism studies of β-alanine, α-alanine, and amino acids zwitterions, plus summarized the relation of these samples to interstellar space.

2.2.1 β-alanine

β-alanine (Figure 2.2) is the only naturally occurring β-amino acid, and it is an organic compound of particular importance in interstellar space. β-alanine was found in various classes of carbonaceous meteorites [8, 9, 14], and is the most abundant type of amino acid in the CI chondrites [8, 14]. It was also demonstrated that synthesis of gas-phase alanine can be achieved via ion-molecule reactions with smaller molecules found in interstellar medium, in which β-alanine was formed preferentially over α-alanine [16]. Such discovery has implied that the β-alanine found in the CI chondrites could be product of pure interstellar reactions, which in terms gives us an insight to the origin of life in space.

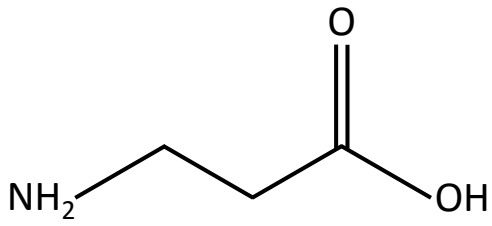

Figure 2.2: Structure of β-alanine.

β-alanine has been subjected to multiple conformational investigations, both computationally and experimentally. The conformational study of β-alanine began with Ramek, who performed computational calculation on the conformers of β-alanine at the HF/4-31G level of theory and found twenty stable conformers [57]. The list of twenty were reduced down to nineteen after McGlone and Godfrey recalculated the stable β-alanine conformers deduced by Ramek with a slightly higher level of theory at HF/6-31G*. Furthermore, McGlone and Godfrey have experimentally observed two gaseous β-alanine species of gauche conformations using free-expansion jet spectrometry, and identified them as conformer I and conformer V [58]. A decade after their study, Sanz *et al.* refined McGlone's and Godfrey's theoretical calculations on the nineteen conformers using MP2/6-311++G** level of theory, and confirmed their observation of conformer I and V using Fourier transform microwave spectroscopy coupled with pulsed supersonic jet and laser ablation. Sanz *et al.* have also identified two additional β-alanine conformers through their experimental procedures, namely conformer II and III [59].

The first conformational investigation of β-alanine with MI-IR spectroscopy was reported by Rosado and his colleagues in 1997 [60]. The group utilized argon gas as their matrix host, and compared the resulting MI-IR spectra to calculated values at RHF/6-31G* level of theory, FTIR spectra from KBr pellet method, and Raman spectra using a 514.5 nm argon laser with 220 mW power as excitation source. Even

though only one conformer was confidently assigned by Rosado *et al.*, the group suggested the presence of multiple different conformers within solid argon, attributed by the observation of several well structured spectra bands at the same vibrational frequency region [60]. Since then, a number of follow-up studies have been performed with the attempt to identify the conformational forms of β-alanine trapped in inert matrices. Most recently are the research performed by Dobrowolski and his group in 2008 [61], and two studies done by Stepanian and his company in 2012 [19] and 2016 [62]. Dobrowolski *et al.* isolated β-alanine in argon matrices, and determined the presence of at least three conformers, which were conformer I, II and IV following Ramek's nomenclatures. They accomplished the spectral assignments by matching the experimental vibrational numbers and intensities to that of high accuracy theoretical calculations at $\mathrm{B3LYP/aug-cc-pVDZ}$ level of theory. Their results also further indicated the possible presence of other higher energy β-alanine conformers in matrix environment [61]. Stepanian *et al.* expanded the search of high energy β-alanine conformers in solid argon by coupling MI-FTIR spectroscopy with matrix annealing and *in-situ* UV-irradiation techniques, with the intend to resolve the overlapping spectra bands of β-alanine. They also performed an extensive potential energy surface (PES) scan at $\mathrm{MP2/aug-cc-pVDZ}$ level of theory and found twenty stable conformational states of β-alanine. Through these exhaustive computational and experimental works, Stepanian *et al.* were able to identify and assign five β-alanine conformers in argon matrices, namely conformer I, II, IV, V, and VII [19]. The group then provided additional confirmation on their observation of conformer V, a highly unstable β-alanine conformer, in solid argon by performing the same experiment on the deuterated analog of β-alanine (β-alanine-d_3) [19, 62].

2.2.2 α-alanine

α-alanine (Figure 2.3) is the smallest amino acids with a chiral carbon atom. The search of chiral amino acids, and other chiral biological molecules, in interstellar space has been intensive due to their relevance to the origin of homochirality of life [63]. Many mechanisms have been proposed on the formation of chiral homogeneity organic molecules in the prebiotic Earth since the discovery of homochirality effect in the 19^{th} century [64]. However, due to the complications and the limitations imposed by the formation mechanisms, most of the proposed processes seemed highly improbable to be carried out terrestrially on the chaotic environment of the prebiotic Earth. To overcome these difficulties, Bonner has suggested that the production of chiral biomolecules on Earth to be an extraterrestrial origin [64], and his concrete view was supported by the discovery of an enantiomeric excess of L-amino acids in the Murchison meteorite [65, 66].

α-alanine has been the subject of many theoretical conformational studies. One of the first computational study of α-alanine was performed by Gronert and O'Hair who derived ten stable conformational states of the amino acid using HF/6-31G*, HF/6-31+G*, and MP2/6-31+G* levels of theory [67]. Around the same period of time, another group led by Sch*ä*fer was conducting a similar computational investigation on α-alanine but with larger basis sets of 6-31G** and 6-311G**, and was able to identify three additional conformers [68]. The most detailed theoretical analysis of α-alanine was carried out by Cs*ászár* [69]. He employed various levels and basis sets for his computational calculations, and obtained the same thirteen stable conformers of α-alanine as located by Sch*ä*fer and his co-workers. These thirteen α-alanine conformers were conformer I, IIA, IIB, IIIA, IIIB, IVA, IVB, VA, VB, VI, VII, VIIIA, and VIIIB according to Cs*ászár*'s

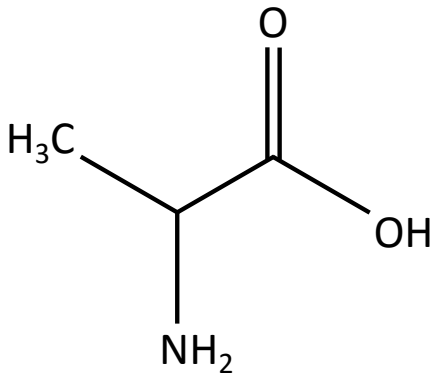

Figure 2.3: Structure of α-alanine.

nomenclatures, in which the notation "A" and "B" represent the L- and D- enantiomer pairs, respectively [69]. Recently, Balabin performed an *ab initio* analysis of α-alanine with the highest level of computation parameters thus far, using CCSD(T)/aug − cc − pVTZ, MP3/aug − cc − pVQZ, and MP2/aug − cc − pV5Z calculations at B3LYP/aug − cc − pVTZ geometries. Contrary to his predecessors, Balabin was only able to derive twelve stable α-alanine configurations, with conformer IIIB (from Cs*ászár*'s list as stated above) being undetected through Balabin's highly accurate calculations [70].

α-alanine has also been the interest of multiple experimental conformational studies, being analyzed with methods ranging from gas-phase electron diffraction [71, 72] to various spectroscopic techniques [45, 47, 60, 73–80]. The following accounts highlight a few selected experimental conformational characterizations of gas phase α-alanine performed since the early 90's until recent years. In 1991, Iijima and Beagley performed a gas phase electron diffraction study on α-alanine and observed only one conformer of the neutral species [71]. Two years later in 1993, a millimeter-wave spectroscopy of α-alanine was reported by Godfrey *et al.*, in which the group was able to identify the two most stable forms of α-alanine conformations, namely conformer I and IIA (according to Cs*ászár*'s nomenclatures), in the 54.2 - 65.4 GHz region by using a Stark-modulated free-expansion jet spectrometer [73]. Godfrey's and his co-workers' observation was later confirmed by Blanco *et al.* in 2004 with laser-ablation molecular-beam Fourier transform microwave (LA-MB-FTMW) spectroscopy in the 6 - 18 GHz region [75], and by Hirata *et al.* in 2008 with millimeter-wave spectroscopy in 80 - 99 GHz and 160 - 180 GHz regions by applying a continuous molecular beam [76]. More recently in 2010, Balabin carried out a jet-cooled Raman spectroscopy study on α-alanine and detected two additional conformers, conformer IIB and IIIA, together with the two previously identified conformer I and IIA [78].

MI-IR spectroscopy is another popular spectroscopy technique used for conformational studies of α-alanine [45, 47, 60, 80]. Together with its isomer β-alanine (see Section 2.2.1), the first MI-IR spectroscopy of α-alanine was executed by Rosado *et al.* in 1997 with only one conformer, conformer I, found by the group [60]. In the subsequent year, Stepanian *et al.* performed a similar argon MI-IR analysis on α-alanine and reported the observation of two conformers, conformer I and IIA, in their matrix. They characterized their spectra using B3LYP/aug − cc − pVDZ and MP2/aug − cc − pVDZ geometry and frequency theoretical calculations [45]. The presence of conformer IIIA in argon environment was identified by Lambie *et al.*

in 2002, along with the previously observed conformer I and IIA. The group combined high resolution MI-FTIR spectroscopy with highly accurate theoretical calculations at B3LYP/6-311++G** level of theory to accomplish their spectral assignments [80]. Nevertheless, conformer IIIA was undetected in the most recent MI-FTIR experiment by Bazsó *et al.*, where α-alanine was isolated in argon, krypton and nitrogen crystals [47]. The group utilized near-infrared (NIR) laser irradiation to distinguish the overlapping conformers' bands and induce conformational change of α-alanine. They also performed quantum calculations at B3LPY/6-31++G** and MP2/6-311++G** level of theories on selected conformer candidates to aid them in spectral analysis. Both conformer I and IIA were found to be present in the prior-irradiated matrices. Interestingly, Bazsó *et al.* observed the production of the short lived conformer VI at the expense of conformer I upon short NIR laser irradiation. Conformer VI was absent in the as-deposited matrices, indicating it as a product purely by photoirradiation. They also detected the slow conversion of conformer I to conformer IIA after a prolonged irradiation process [47].

2.2.3 Amino Acids Zwitterions

Amino acids exist predominantly in their zwitterionic forms in the aqueous and crystalline media, but in neutral forms in gas phase. Zwitterion is the result of solvent effect on an amino acid, where a proton from the acidic group is transferred to the amino group of the molecule (Figure 2.4). Water is considered to be the main culprit in inducing zwitterion formation. In fact, only a small amount of water molecules is required to drive the ionic transformation of amino acid. Xu *et al.* reported in their hydration studies that the lower limit of five water molecules were required to transform glycine into its zwitterion, while only four each were needed for phenylalanine and tryptophan [81]. In terms of interstellar chemistry, water is one of the most abundant species present in astronomical media, especially in astrophysical ices. Thus, it is highly possible that amino acids in extraterrestrial frozen particles interact with the trapped water molecules, resulting in the production of zwitterions in interstellar space [82].

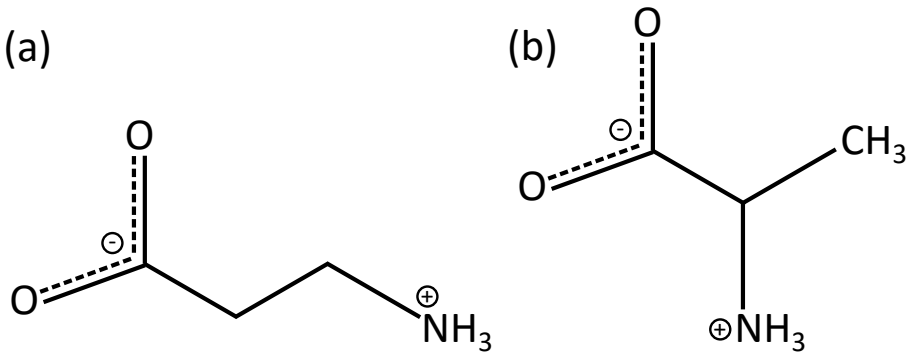

Figure 2.4: Structure of (a) β-alanine and (b) α-alanine zwitterions.

Many computational [83–90] and experimental[81, 82, 91–95] studies have been performed on various amino acids in their zwitterionic forms to investigate the structural properties and chemical stabilities of the ionic molecules. However, only a few of these investigations were carried out with MI-IR spectroscopy technique [82, 92, 94]. In 2004, Ramaekers *et al.* reported an argon MI-FTIR spectroscopy study of neutral

and zwitterion glycine·H_2O complexes. The aim of their research was to investigate the H-bond interaction between glycine and water in matrix environment, and they registered the observation of zwitterionic H-bond complexes at a higher stoichiometry complexes glycine·$(H_2O)_n$ with n larger than 3. The experiment has also provided the first IR evidence of zwitterion formation in cryogenic isolated condition [94]. Ramaekers's and his colleagues' observation was supported by Espinoza *et al.*, where the group performed a similar hydration of glycine experiment in argon crystal. Although Espinoza *et al.* did not purposely produce zwitterion in their study, the group observed clear geometrical alterations as the first, and then the second, water molecule was introduced to the bare glycine. They have also pinpointed the mode of H-bonding as glycine interacted with the surrounding water [92]. Recently, Rodríguez-Lazcano *et al*. recorded the IR spectra of pure α-alanine crystal grown in cryogenic temperature of 25 K, and slowly warmed to 200 K. The group also co-deposited α-alanine with H_2O, CO_2 or CH_4 onto the cold substrate to create ice mixtures of different polarity analogous to astrophysical ices. From their experiment, Rodríguez-Lazcano *et al.* observed neutral/zwitterion ratio of 60 % for pure alanine and H_2O mixtures, and 90 % for the non-polar matrices of CO_2 and CH_4 crystals, as deposited at 25 K. The ratio was shown to drop as the temperature of the crystals rose, leaving only the ionic species at 200 K. The rate of neutral to zwitterion conversion also appeared to be environment-dependent, with sample in non-polar matrices acquired a slower conversion rate than those in pure sample crystals and polar matrices [82].

Chapter 3

Method

3.1 Experimental

3.1.1 Making Enriched Parahydrogen Gas

Normal hydrogen gas of 99.99 % purity (Praxair Canada Inc.) was converted into parahydrogen gas of 99.9955 % purity using a parahydrogen converter. This specific device was designed and built by my supervisor, Dr.Takamasa Momose, and his associates from University of Illinois and University of British Columbia during the year of 2008 [1]. The system is an improvement to the converter developed by Tam and Fajardo in the year of 1999, which used a closed-cycle He cryostat, thus liquid He instead of the conventional liquid N_2 or liquid H_2 as cryogen [96].

Briefly on the parahydrogen converter design, the converter consists of a commercial closed-cycle He cryostat (APD Cryogenics Inc., Daikin Cryotec He Compressor Unit U104CW) modified to mount an ortho-para reactor coil onto its cold head (Figure 3.1). The coil is a solid piece of oxygen free high conductivity (OFHC) copper around which a 6.35 mm diameter copper tubing has been wound and permanently attached to it. The copper tubing was filled with 3.3 grams of a 30 $\times$ 50 mesh hydrous ferric oxide catalyst (Sigma-Aldrich, catalyst grade), which is the main component for conversion of orthohydrogen to parahydrogen. The copper tubing loops around the OFHC core 14 times in an upward helical fashion, providing approximately 1.3 m of conversion path length. The last segment of the tubing passes through the center of the core, thus ensuring that the final portion of the conversion process happened at the coldest temperature of the assembly. Two 1.59 mm austenitic stainless steel tubings are bended and arranged transverse to the length of the cryostat with their ends connected to the head and tail of the reaction coil (Figure 3.2), providing hydrogen gas with an incoming and outgoing routes to and from the coiled conversion section. The entry and exit ports of the cryostat chamber are each connected to a flow counter (Kojima Instruments Inc., Kofloc mass flow meter 3720, Gas H_2, range 10 SLM) in order to read the incoming and outgoing controlled flow rates of hydrogen gas. Two separate silicon diode temperature sensors (Cryogenic Control System, Inc., Temperature Sensor S900-BB) and controller systems (Cryogenic Control System, Inc., Temperature Controller Cryo.CON 34) are attached to each ends of the reactor coil to act as temperature monitors and

control devices for the apparatus. The whole instrumentation is operated under high vacuum, and the system is evacuated by a roughing oil pump (Alcaltel Pascal 2021 SD) backed-up with a diffusion oil pump (Diavaclimited Diffusion Pump DPF6Z) to get the pressure down to $\leq 10^{-4}$ torr range.

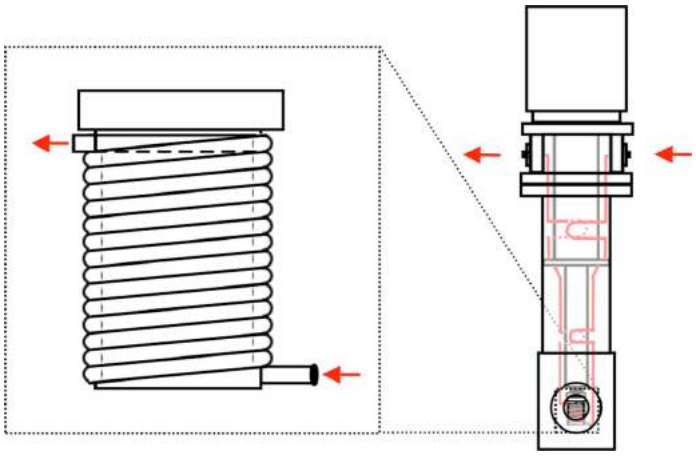

Figure 3.1: Diagram of the parahydrogen converter with a close-up of the reactor coil in which is mounted on the cold head of the closed-cycle cryostat refrigerator and is filled with hydrous ferric oxide catalyst. The image is used with the permission of Tom *et al.* [1].

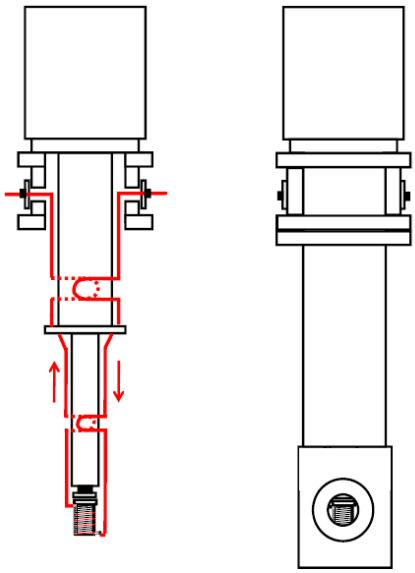

Figure 3.2: Diagram of parahydrogen converter with (right) and without (left) the vacuum shroud. The traces of hydrogen gas flowing into and out of the reaction coil section (red trace) is shown in the schematic with the shroud removed. The image is used with the permission of Tom *et al.* [1].

On the procedure, we first set the temperature controllers to 13 K from the coldest chamber temperature of 7 K. It typically took only 5 min for the system to reach 13 K, but we added another 30 min to our heating time to ensure thermal equilibrium across the entire coil. As previously mentioned, the temperature of 13 K is close to the triple point of hydrogen at 13.8 K in which corresponds thermodynamically to 99.9955 %

of parahydrogen (see Section 2.1.2). Note that as it took 5 hrs for the cryogenic chamber to be cooled from room temperature to the coldest point of 7 K, we always kept our cryostat on and running, and only shut it down on a monthly basis for maintenances purposes.

Once the chamber temperature was stabilized at 13 K, we slowly flowed hydrogen gas into the converter with a flow rate of 0.8 SLM. Hydrogen gas underwent a phase change to liquid upon entering the cold coil section, and we waited 30 min for the entire coil to be filled with liquid hydrogen. After the whole coil was filled, we let gas flowed through and out of the converter for at least 10 min (which equates to almost a standard litre) with a flow rate of 0.4 SLM to (a) ensure that any residue gas from the previous experiment will be purged out of the system, and (b) clean the stainless steel gas lines involved in routing the gas from the converter to the storage cylinders with pure parahydrogen gas. This gas was then evacuated using the roughing oil pump. Note that a reasonably slow flow rate was applied to give sufficient time for the conversion of ortho- to parahydrogen via magnetic perturbation by the catalyst. However, if the flow rate was too slow, we might encounter an issue with the backing pressure, which might cause a back flow of gas from the exit port of the converter back into the coil system. For our system, we found that the flow rate of 0.4 SLM seemed to supply ample of time for the conversion process in the converter, and yet gave enough pressure to push the gas moving forward.

After an appropriate amount of purging was completed, we allowed the freshly produced parahydrogen gas to flow into the 1 L storage tank, and the vessel was being filled up to 700 - 900 torr. Parahydrogen was known to undergo back conversion when being exposed to stainless steel surface or impurities such as paramagnetic O_2 molecule [1]. To minimize this back conversion occurrence, we used a teflon-lined stainless steel gas cylinder (D01-3A1800 Whitey P-5EK086-304L-HDF4-1000CC), with a stainless steel quarter turn plug valve (Swagelock S-43S4) sealed to its opening end, as our storage vessel. The back conversion rate of parahydrogen in this storage system was calculated by Tom *et al.* to be 1.7 % per week, and was most likely due to the exposure of the gas to a small stainless steel area at the end cap of the cylinder [1]. We also never stored our parahydrogen gas for more than 24 hrs, and made a new badge for every experimental run to ensure that the sample used as matrix gas was in its purest and cleanest available form.

3.1.2 Preparing Argon Matrix Gas

99.99 % purity argon gas (Praxair Canada Inc.) was employed with no further modifications. Prior to deposition procedure, we flowed and stored the required amount of argon gas (700 - 900 torr), into another 1 L teflon-lined stainless steel gas cylinder equipped with a stainless steel metering valve (Swagelock SS-DSS4) at its opening end. The gas was flowed from the gas cylinder source through a leak-free nylon tubing (Freelin-Wade: A Coil Hose Co.) followed by the stainless steel gas lines routing to the storage vessel.

3.1.3 Sublimation of Amino Acid with a Knudsen Cell

Most samples used for matrix-isolation spectroscopy experiment are high vapour pressure solvents, and they are introduced into the matrices simply by pre-mixing the matrix gas with an appropriate amount of vapour sample. However, this method of doping is inapplicable on our powdered amino acid stocks. Amino acids

exist only as neutral forms in the gas phase. Whereas in the condense phases, amino acids exist mainly as zwitterions (see Section 2.2.3). To dope neutral amino acid into the matrices, we need a mechanism that allow us to sublime the solid sample into gas, and a Knudsen effusion cell is the most efficient device to do so.

We used an built in-house Knudsen cell (Figure 3.3) to sublimate our amino acid sample directly into the matrix chamber. Our design is that of a simple resistance-heated Knudsen cell. The copper cell body is 42 mm long and 8 mm wide, with its threaded cap connected to an 18 mm long and 1.6 mm wide copper nozzle, giving an orifice of 1 mm in diameter. The cell is heated with a ceramic heater (Thorlabs, HT15W Cartridge Heater) attached to the rear end of the cell. A DC power supply (Takasago, LTD. Japan, GP0110-1 Regulated DC Power Supply) is used to regulate the heating power of the heater, and the temperature of the cell is monitored by a temperature sensor (Thorlabs, TH10K NTC Thermistor) situated behind the sample compartment of the cell. This set-up allows us to carefully control and maintain the temperature of the cell within an accuracy of ± 1 K.

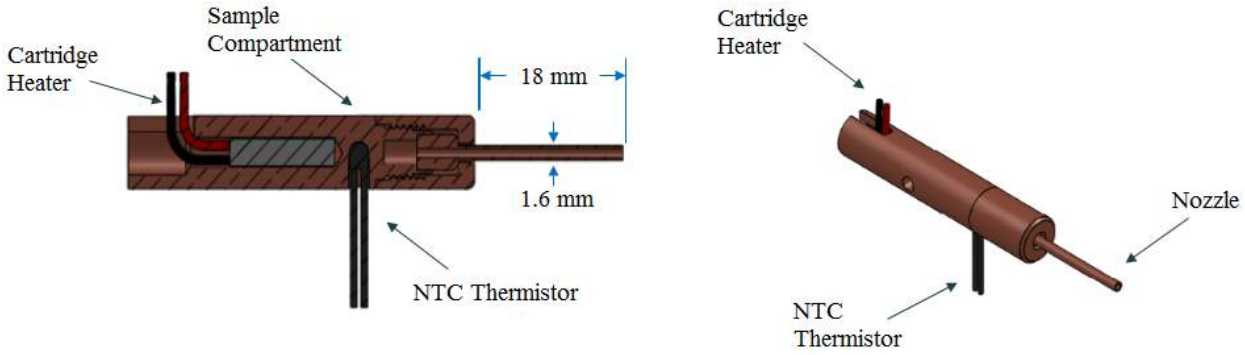

Figure 3.3: Diagram of the inner compartment (left) and outer shell (right) of our built in-house Knudsen cell which was employed to sublimate the amino acid samples.

As we were exploring the relation of amino acids' conformational populations with varying sublimation temperatures, we needed to employ a range of sublimation temperatures onto our samples. These temperatures must be high enough to ensure an ample amount of gaseous sample is produced for deposition, yet not too high to cause thermal decomposition of amino acids. To find these appropriate, but narrow, range of sublimation temperatures, we did a deposition test run in solid parahydrogen for each amino acid samples used in our project. The procedure for sample deposition was described in the following section (see Section 3.1.4). On these test runs, we started the deposition with the lowest predicted sublimation temperature. We then took a quick measurement on the sample crystal after 15 min of deposition at a specific temperature, and increased the Knudsen cell temperature by 10 K increment after each measurements. We continued with this process until we saw signs of fragmentations from amino acid, which were indicated by the present of additional peaks aside from the expected molecular signals in our spectrum. From the spectra taken, we could then deduce the minimum sublimation temperature from the first sight of amino acid signals, and the maximum sublimation temperature from the first indication of sample decomposition. Note that some fragmented products could be reactive, and they could interact with the molecular amino acids and the matrix environment, giving us undesired results.

3.1.4 Deposition of Amino Acid in Solid Parahydrogen

Our cryogenic chamber (Figure 3.4) is a 22 cm wide doubly shielded chamber, with a 1 cm thick and 20 cm inner diameter wide stainless steel outer shield, and a 1 cm thick and 14 cm inner diameter wide copper inner shield. A 10 cm wide copper cold plate is sitting on top of the cold head of a closed-cycle Gifford-McMahon refrigerator (Sumitomo Heavy Industries, Ltd., Helium Compressor Unit CKW-21A, Cryocooler SRDK-205) situated in the center of the chamber. The refrigerator can cool the cold plate down to 3.6 K, and the cold substrate to 4 K. The cold substrate is a BaF_2 wedged window (Pier Optics Co., Ltd., 25 mm in diameter, 2 mm in mean thickness) held by a 4 cm by 4 cm copper window holder mounted onto the cold plate. Two separate silicon diode temperature sensors (Cryogenic Control System, Inc., Temperature Sensor S900-BB) are attached each to the cold plate and the cold substrate, with a temperature controller (Cryogenic Control System, Inc., Temperature Controller Cryo.CON 34) coupled with the sensor on cold plate, to allow for careful monitoring of the chamber temperature. The matrix gas is introduced into the chamber through a 1.59 mm stainless steel inlet tubing with its tip positioned 3.5 cm away from the cold substrate at a 45° angle. A gas flow controller (Stec Inc., Mass Flow Controller SEC-4400M0-MK3, Gas H_2, Flow Rate 500 ccm) is installed on the stainless steel tubing outside the chamber to allow for controlled flow rate of matrix gas onto the cold substrate. The tip of the Knudsen cell is placed 2.5 cm away from the cold substrate at another 45° angle, making a 90° angle with the matrix gas feed-in tube. The chamber is kept under high vacuum by a turbo pump (Pfeiffer Vaccum D-35614 Assiar, HiCube 80 Eco), giving a pressure of 3×10^{-6} torr at room temperature, and 3×10^{-8} torr at cryogenic temperature of 4 K.

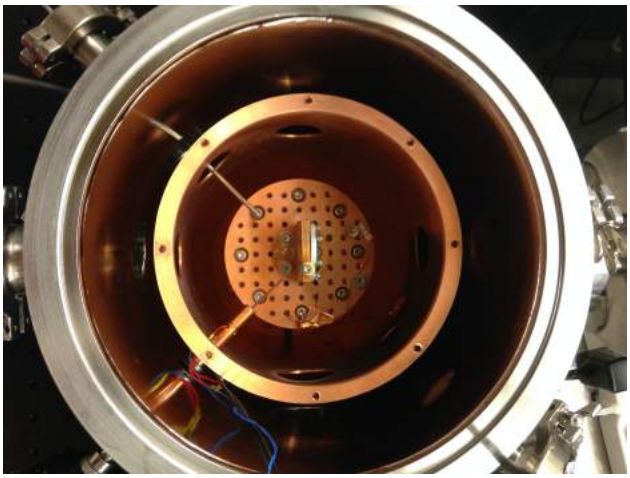

Figure 3.4: Picture of the cryogenic chamber used for sample deposition with the covers removed. The chamber is a doubly shielded chamber, with the a BaF_2 window positioned in the middle of the center copper cold plate. The line at the top left corner of the image, situated at a 45° angle to the cold window, is the stainless steel matrix gas feed-in tube; whereas the object at the bottom left corner of the image, situated at another 45° angle to the cold window, is the Knudsen cell used for amino acid sample sublimation.

Deposition was done at the coldest window temperature of 4 K. The crystal sample was grown directly on the cold substrate by simultaneously sending parahydrogen gas and the sublimated amino acid sample into the chamber, thus allowing gaseous amino acid to mix into the matrix gas before being deposited onto

the cold surface. To achieve this procedure, we heated the Knudsen cell up to the targeted sublimation temperature for the first 5 - 10 min, and stabilized the cell temperature within ± 1 K range. We then flowed parahydrogen into the chamber with a low flow rate of 4 - 5 ccm.

Ideally, the cold substrate temperature should remain at 4 K before, during, and after deposition. However, due to the introduction of hot matrix gas and thermal irradiation from the Knudsen cell, we noticed that our cold substrate temperature increased a little during deposition. The annealing temperature for parahydrogen is at 5 K, and deposition at the annealing temperature or higher will cause the formation of the opaque and hard amorphous crystal, instead of the soft and clear quantum crystal. To avoid the formation of amorphous crystal, we kept the cold substrate temperature at 4 ± 0.3 K, and never exciding 4.5 K, by ensuring that the flow rate of parahydrogen into the chamber and the heating power implemented on the Knudsen cell remain low throughout the whole deposition process. Note that the window temperature after deposition was typically around 4.15 ± 0.02 K.

The specificity of deposition procedure, such as the range of sublimation temperatures used and the duration of deposition, for each amino acid experiment was briefed in the Result portion under the individual samples' subsections (see Sections 5.1.1, 5.2.1, 5.3.1, and 5.4.1).

3.1.5 Deposition of Amino Acid in Argon Matrices

The procedure of depositing amino acid in argon matrices was similar to that of solid parahydrogen, aside for a few discrepancies. Instead of depositing at the coldest substrate temperature of 4 K, we grew our argon crystal sample on an 18 K window. After deposition, we also performed annealing on the solid argon to reduce the site slitting effects often associated with rare gas matrices. Annealing was done by slowing heating the argon crystal up to the annealing temperature of 35 - 40 K, stabilizing the matrix at the annealing temperature for 10 - 15 min, then slowly reducing the window temperature back down to 4 K to take measurement. We repeated these steps until no more site shifting was observed from the spectra.

3.1.6 *In-Situ* UV-irradiation of Amino Acid within the Solid Matrices

We used a modified deuterium lamp (Hamamatsu Photonics K.K., L_2D_2 Lamp L7295, Power 30 W, Spectral Distribution 160 - 400 nm), housed in a custom made lamp housing and controlled by its associated power supply (Hamamatsu Photonics K.K., Deuterium Lamp Power Supply C1518), as our UV-irradiation source (Figure 3.5). The light was sent in through a MgF_2 window (Thorlabs, WG61050, 25.4 mm in diameter, 5 mm thickness) installed at the side portal of the chamber, and hit the BaF_2 cold window from the back (Figure 3.6). Note that the matrix sample was grown on the front of the cold window. Thus, UV photons were transmitted through the cold window to reach the sample molecule. BaF_2 window has a transmission range of 200 nm - 12 μm, making it a suitable cold substrate for this irradiation set-ups.

We typically irradiated the deposited sample for a total of 3 - 4 hrs, and recorded a spectrum at each hour of irradiation. All UV-irradiation were done at 4 K. The specificity of UV-irradiation procedure for each amino acid experiment was briefed in the Result portion under the individual samples' subsections (see Sections 5.1.1, 5.2.1, and 5.3.1).

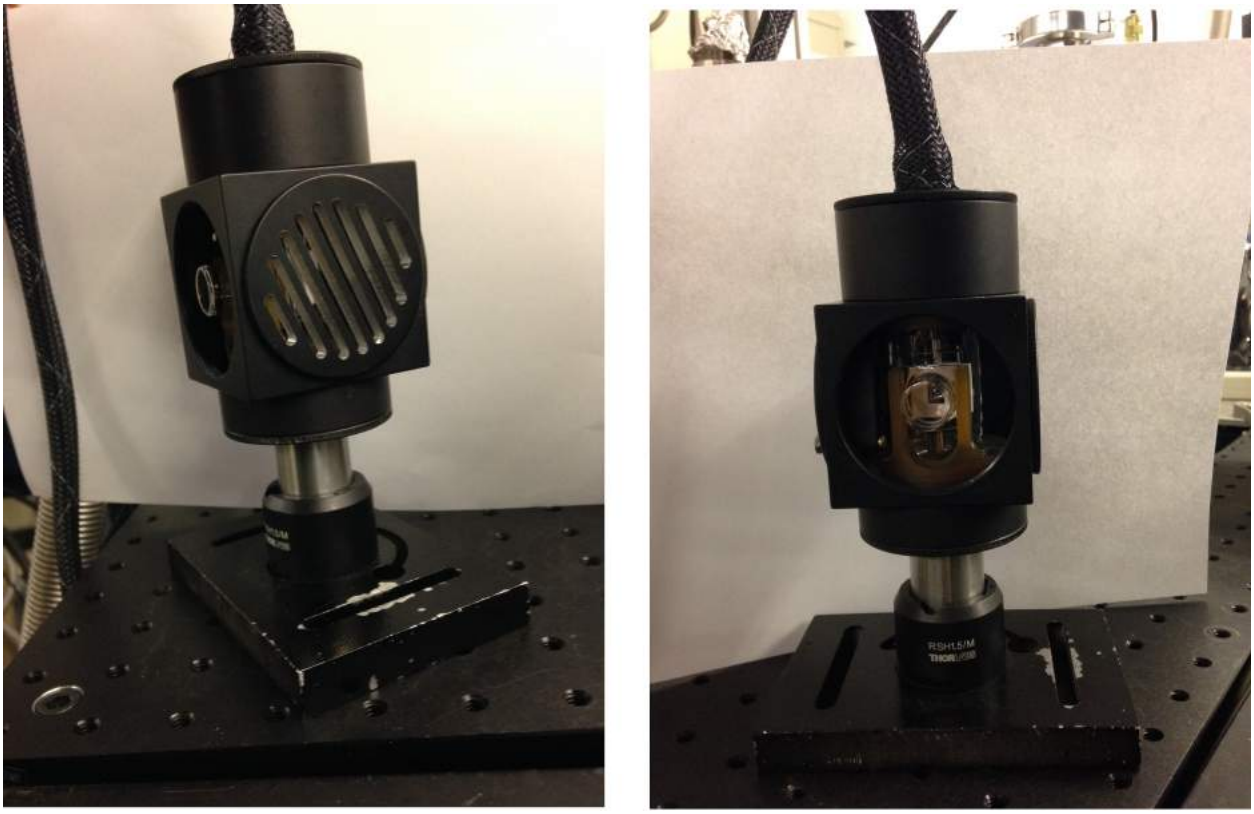

Figure 3.5: Pictures of the deuterium lamp enclosed within its housing used for the *in-situ* UV-irradiation experiments.

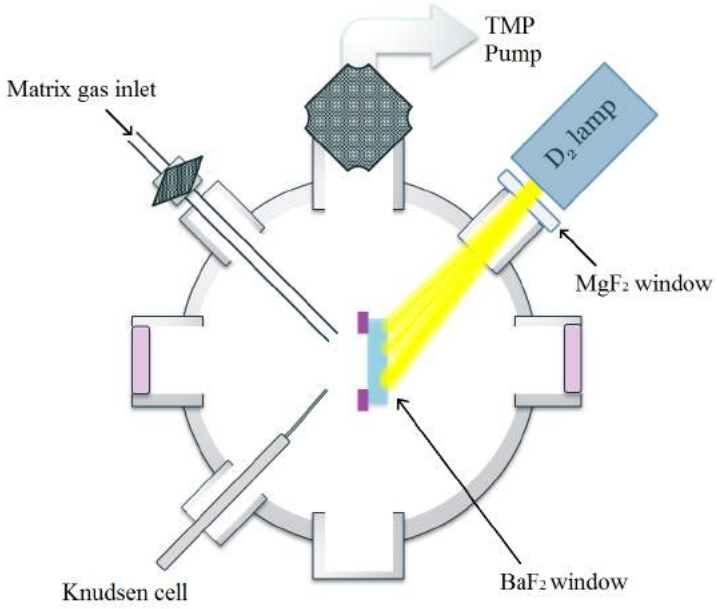

Figure 3.6: Diagram of cryogenic sample chamber with the portal of UV-irradiation from the deuterium lamp through the back MgF_2 window to the back-side of the BaF_2 cold window.

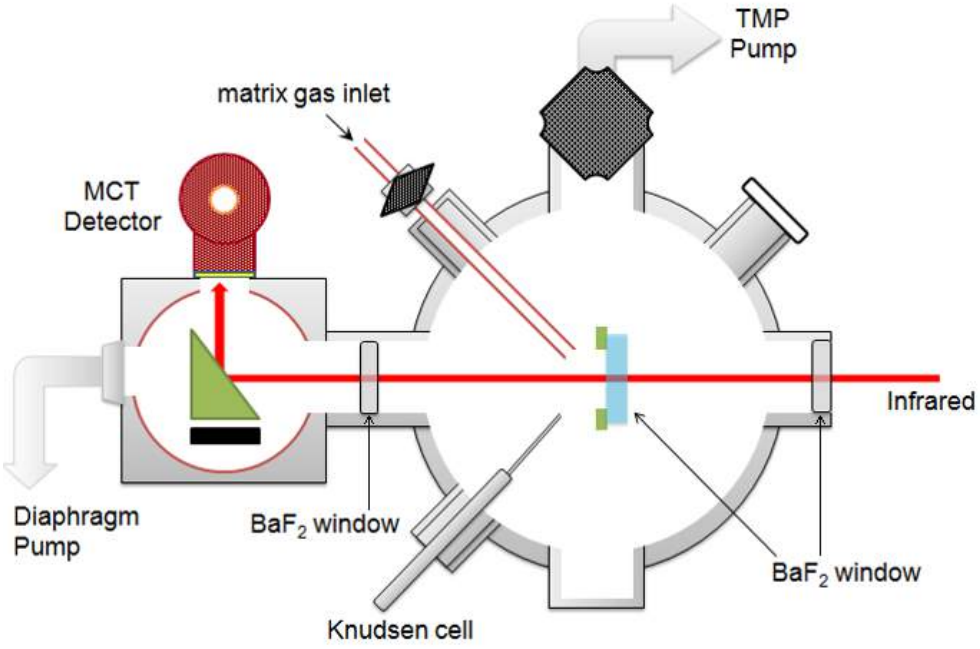

Figure 3.7: Diagram of the cryogenic sample chamber with the path of IR light from the FTIR spectrometer travelling through the three BaF_2 cold windows (with the middle window holds the sample crystal), and to the MCT detector by being deflected in the transfer optic chamber with a parabolic mirror.

3.1.7 FTIR Measurement Parameters and Detection System Set-ups

We used a FTIR spectrometer (Bruker, IFS 125HR), equipped with a KBr beam splitter, MIR globar light source, and a liquid nitrogen cooled MCT detector (InfraRed Associates. Inc., D316/2M), to attain all the optical measurements for our experiments. The instrumentation was maintained under low pressure of 0.05 hPa with a mechanic pump (Adixen OMF 40S). As the sample chamber was situated outside the spectrometer, the IR beam was sent into the cryogenic chamber by deflecting the light at an angle of 90° via a parabolic mirror. The beam passed through two separated BaF_2 windows (Pier Optics Co., Ltd., 25 mm in diameter, 2 mm in mean thickness) upon entering and exiting the chamber, and hit the sample substrate situated at the middle of the chamber from the back. The beam was then travelled to another parabolic mirror contained within an built in-house transfer optic chamber (11 cm $\times$ 11 cm), and being deflected at another 90° angle into the MCT detector (Figure 3.7). The transfer optic chamber was kept under low pressure with a small mechanical pump (Oerlikon Leybold Vacuum, DIVAC0.8LT).

All spectra were registered at 4 K in the range of 700 - 4800 cm^{-1}, with either 0.2 cm^{-1} or 0.05 cm^{-1} resolution, and a total of 1000 number of measurements. The specific measurement parameters for each amino acid experiment was briefed in the Result portion under the individual samples' subsections (see Sections 5.1.1, 5.2.1, 5.3.1, and 5.4.1).

3.2 Computational

3.2.1 Quantum Calculation with WebMO

We performed quantum calculations at $\mathrm{B3LYP/aug-cc-pVTZ}$ level of theory on the most stable conformers of our amino acid samples using WebMO [97]. The corresponding relative energies, relative Gibbs free energies, and theoretical vibrational wavenumbers and intensities were then derived from the calculations in order to interpret our experimental spectra. To ensure a calculated result with the highest obtainable accuracy, tight optimization was applied on each geometry used.

The amino acids' conformers chosen for quantum calculations must be local minimum conformers for the derived vibrational wavenumbers to be real. We explored published theoretical materials to determine the most appropriate conformational structures of amino acids to be used for calculations. Details on each amino acid configuration used for theoretical calculation was mentioned in the Result portion under the individual samples' subsections (see Sections 5.1.1, 5.2.1, and 5.3.1).

Chapter 4

Theory and Calculations

4.1 Relative Energy and Relative Gibbs Free Energy

A way to determine the stability of a molecular conformer is to check on the conformer's relative energies and relative Gibbs free energies. From thermodynamic perspective, conformer with the lowest relative energy and relative Gibbs free energy often attributed to the most stable configurations of the molecule [98]. This relation is thus applied by spectroscopists to predict the probability of detecting specific conformer configurations in their experimental spectra, in particular in IR spectra.

The acquire information for the calculation of relative energies and the relative Gibbs free energies of a molecule can be extracted from the sample output of quantum computing programmes such as Gaussian or WebMO [99]. The following subsections highlight the calculation steps to determine the relative energies and relative Gibbs free energies associated with our amino acids investigations, with WebMO being the quantum computing program utilized for our studies.

4.1.1 Calculation of the Relative Energy

The calculation of the relative energy of a specific conformer is fairly straightforward. It must be noted that WebMO uses the lowest possible energy state (*i.e.*, the zero-point energy (ZPE))of a system, instead of the minimum of the classical potential well, to determine many of the calculated thermodynamic quantities [99]. These computed quantities include the total electronic energy, E_{tot}, which is the energy of the molecule relative to the separated nuclei and electron [100]. Therefore, to obtained the real total energy of a molecule in its specific conformational state, E_j, we must correct the total electronic energy of the conformer, $E_{tot(j)}$ listed in the sample output of WebMO to the conformer's ZPE by

$$E_j = E_{tot(j)} + ZPE. \tag{4.1}$$

The relative energy of the conformer, ΔE_j, can then be computed by weighing E_j to the real total energy of the lowest energy conformer, E_1 (assuming Conformer I to be the conformational configuration with the lowest energy), as shown with

$$\Delta E_j = E_j - E_1. \tag{4.2}$$

4.1.2 Calculation of the Relative Gibbs Free Energy

Gibbs free energy, G, correlates with the temperature of the system through the relation

$$G \equiv H - TS \tag{4.3}$$

in which H is the expression for enthalpy, S is the expression for entropy, and T represent the temperature of the system [98]. For our amino acids studies, T would be the sublimation temperature of an amino acid sample for a particular deposition procedure.

The WebMO program carries out its thermodynamic computations by assuming an ideal gas at atmospheric pressure (1 atm) and room temperature (298.15 K) [97, 99]. This assumption does not align with our real experiment system of varying sublimation temperatures, which are in the range of 380 - 430 K depending on the sample employed. Therefore, to calculate the Gibbs free energies at a specific amino acid sublimation temperature, G_T, we must start our calculation from the very core of thermochemistry, *i.e.*, the molecular partition functions, q.

The first factors to be determined for G_T calculation are the thermal correction to the internal thermal energy, E_{corr}, and the entropy, S_{corr}, of a molecular system. E_{corr} and S_{corr} are given as the sum over all four components of contributions, which are the translational (*trans*), rotational (*rot*), and vibrational (*vib*) degrees of freedom, plus the electronically excited states (el) [99]. The relations of E_{corr} and S_{corr} to the four contributional components are represented by

$$E_{corr} = E_{trans} + E_{rot} + E_{vib} + E_{el} \tag{4.4}$$

and

$$S_{corr} = S_{trans} + S_{rot} + S_{vib} + S_{el}, \tag{4.5}$$

respectively. Note that the internal thermal energy contribution from partition function, E_q, is given by

$$E_q = Nk_BT^2(\frac{\delta lnq}{\delta T})_V \tag{4.6}$$

where k_B is the Boltzmann constant; whereas the entropy contribution, S_q is given by

$$S_q = R(lnq + T(\frac{\delta q}{\delta T})_V) \tag{4.7}$$

where R is the gas constant [101].

The electronic partition function, q_{el}, of a molecule is defined as

$$q_{el} = \omega_0 e^{-\varepsilon_0/k_BT} + \omega_1 e^{-\varepsilon_1/k_BT} + \omega_2 e^{-\varepsilon_2/k_BT} + ... \tag{4.8}$$

in which ω is the degeneracy of the the energy level and ε_n is the energy of the nth level [101]. In WebMO, an assumption is made on the energies of the first and higher electronic excitation states to be much greater than k_BT, thus making these states inaccessible at any temperature [99]. Plus, the energy of the ground

electronic state is set to be the ZPE of the system, equating ε_0 to zero [99]. These assumptions have simplify q_{el} to

$$q_{el} = \omega_0, \tag{4.9}$$

and simplify the entropy due to electronic motion, S_{el} to

$$S_{el} = R(lnq_{el} + 0) = R(ln\omega_0) \tag{4.10}$$

which equates to zero (S_{el} = 0). Furthermore, as there are no temperature dependent terms in the assumed electronic partition function (Equation 4.9), the contribution to the internal thermal energy due to electronic motion, E_{el} is also equates to zero (E_{el} = 0).

The translation partition function, q_{trans}, of a molecule is defined as

$$q_{trans} = (\frac{2\pi mk_BT}{h^2})^{3/2}V = (\frac{2\pi mk_BT}{h^2})^{3/2}\frac{k_BT}{P} \tag{4.11}$$

in which m is the mass of the molecule and h is the Planck constant [101]. Translational entropy, S_{trans} is thus

$$S_{trans} = R(ln(q_{trans}\kappa) + T\frac{3}{2T}) = R(lnq_{trans} + 1 + 3/2) \tag{4.12}$$

in which κ is the factor originate from Stirling's approximation, and the contribution to the internal thermal energy due to translation, E_{trans} is

$$E_{trans} = \frac{3}{2}RT. \tag{4.13}$$

The rotational partition function, q_{rot}, of a non-linear polyatomic molecule is defined as

$$q_{rot} = \frac{\pi^{1/2}}{\sigma_r}(\frac{T^{3/2}}{(\Theta_{r,x}\Theta_{r,y}\Theta_{r,z})^{1/2}}) \tag{4.14}$$

in which σ_r is the rotational symmetry number and Θ_r is the rotational temperature of the molecule in relation to the molecular axis [101]. The values of σ_r and Θ_r are provided in the WebMO output [97, 99], allowing us to quickly calculate the rotational entropy, S_{rot}, and the contribution to internal thermal energy due to rotation, E_{rot}, through the equations

$$S_{rot} = R(lnq_{rot} + \frac{3}{2}) \tag{4.15}$$

and

$$E_{rot} = \frac{3}{2}RT, \tag{4.16}$$

respectively.

The vibrational partition function, $q_{vib,K}$, of a specific vibrational mode is defined as

$$q_{vib,K} = \frac{e^{-\Theta_{v,K}/2T}}{1 - e^{-\Theta_{v,K}/T}} \tag{4.17}$$

where $\Theta_{v,K}$ is the vibration temperature given by $\Theta_{v,K} = h\nu_K/k_B$. The overall vibrational partition function of a molecule, q_{vib}, is thus

$$q_{vib} = \Pi_K \frac{e^{-\Theta_{v,K}/2T}}{1 - e^{-\Theta_{v,K}/T}} \tag{4.18}$$

[101]. In WebMo, the vibrational temperatures of all the calculated vibrations are listed in the output [97, 99], allowing us to calculate the vibrational entropy, S_{vib}, and the contribution to internal thermal energy due to vibration, E_{vib}, through the equations

$$S_{vib} = R\Sigma_K(\frac{\Theta_{v,K}/T}{e^{-\Theta_{v,K}/T} - 1} - ln(1 - e^{-\Theta_{v,K}/T})) \tag{4.19}$$

and

$$E_{vib} = R\Sigma_K\Theta_{v,K}(\frac{1}{2} + \frac{1}{e^{-\Theta_{v,K}/T} - 1}). \tag{4.20}$$

From the obtained E_{corr} and S_{corr}, we can determine the thermal correction to the enthalpy, H_{corr}, and the Gibbs free energy, G_{corr}, of the molecular system through the equations

$$H_{corr} = E_{corr} + k_B T \tag{4.21}$$

and

$$G_{corr} = H_{corr} - TS_{corr}. \tag{4.22}$$

G_T can then be obtained by correcting the total electronic energy, E_{tot}, to G_{corr} through

$$G_T = E_0 + G_{corr}. \tag{4.23}$$

Finally, the relative Gibbs free energy of a specific molecular conformer at a fixed sublimation temperature, $\Delta G_{T(j)}$ can be calculated by weighing the Gibbs free energies of the conformer at the indicated sublimation temperature, $G_{T(j)}$ to the Gibbs free energy of the lowest energy conformer at the same sublimation temperature, $G_{T(1)}$ (again, assuming Conformer I to be the conformational configuration with the lowest energy), as shown with

$$\Delta G_{T(j)} = G_{T(j)} - G_{T(1)}. \tag{4.24}$$

For our experiment, the relative Gibbs free energy, $\Delta G_{T(j)}$, would be a more accurate interpretation of the amino acids' conformational stability than the relative energy, ΔE_j. ΔE_j only considers the electronic component of the molecule, in which is independent from the temperature of the system [101]. However, for our experiments of varying sublimation temperatures, the temperature-dependent components in a molecular system are the keys to determine the stability of a molecular conformer at a specific system temperature as the partition functions between different systems change due to the difference in temperature. The vibrational degree of freedom is the largest contribution to a temperature-dependent molecular system [100] as described in Equations 4.17-4.20; whereas the rotational and translational degrees of freedom input a little of their contributions to the system as explained in Equations 4.14-4.16 for rotation and Equations 4.11-4.13 for translation. $\Delta G_{T(j)}$ is derived with the consideration on vibrational, rotational, and translational con-

tributions, meaning it is a component with a relation to the temperature of a specific system, thus a better representation of the energy of our conformational molecules.

4.2 Boltzmann Distribution Law

The distribution of conformers within a system of constant temperature is given by the Boltzmann distribution law

$$\frac{N_j}{N_{tot}} = \frac{e^{-\varepsilon_j/k_BT}}{\sum_i e^{-\varepsilon_i/k_BT}} \tag{4.25}$$

where N_j is the number of molecules corresponding to conformer "j", N_{tot} is the sum of all the conformer's molecules, ε is the energy of conformer state, k_B is the Boltzmann constant, and T is the temperature of the system [98]. For our amino acid studies, we employed T to be the sublimation temperature of the amino acids for a particular deposition procedure, and ε to be the calculated Gibbs free energy of the sample at specific sublimation temperature, ΔG_T, as highlighted above (see Section 4.1.2). From the Boltzmann distribution law, we can deduce that lower energy conformers would be more predominantly exist in the system as compared to higher energy conformers. We can also acquire a trend of increasing population in the higher energy conformers with the increase in the system temperature. Indeed, we have applied these conclusions to our experimental analysis on the relation of sublimation temperature to the population of gaseous amino acids (see Section 5.2.3).

Chapter 5

Results and Discussions

5.1 Conformational Analysis of Gaseous β-alanine in Solid Parahydrogen and Argon Matrices

We investigated the conformational stability of β-alanine in solid parahydrogen using FTIR spectroscopy, and compared the results to those in argon matrices. We also explored the behaviour of β-alanine conformers in an UV environment by performing *in-situ* photoirradiation.

We had published our results in the Journal of Molecular Spectroscopy on January 2015 [2]. The following subsections are mostly copies from our original paper, with minor editions and rearrangements to accommodate the format and coherency of this thesis.

5.1.1 Experimental and Computational Details for β-alanine Conformational Study

This section highlights the experimental and computational specificities applied in our β-alanine conformational study. The general set-ups and procedure have been described previously (see Chapter 3).

Similar to the general deposition procedures, the matrix gas was deposited onto the cold BaF_2 window simultaneously with β-alanine sublimation, with deposition being performed at 4 K for solid parahydrogen matrix experiments, and 18 K for argon matrix experiments. The gas flow rate was 5 ccm for parahydrogen. However, a much lower gas flow rate of 0.1 ccm was applied for argon. A typical deposition duration was 1.5 hrs for parahydrogen and 2 hrs for argon.

From the deposition test run, we observed that the β-alanine sample (Sigma Aldrich, 99 % purity, used as received) started to sublimate at around 360 K and decompose above 400 K with our Knudsen cell. In this study, β-alanine was sublimed at 390 ± 1 K for both solid parahydrogen and argon experiments. Sample was also introduced into the matrix at 340 K, below the reported sublimation temperature of β-alanine, in order to identify spectral peaks due to impurities in the samples. The flow of gaseous β-alanine was simply regulated by the temperature of the Knudsen cell. The concentration of β-alanine in the matrix was unknown for all experiments, but in general the concentration of sample in solid parahydrogen was ten times less than that in argon matrices due to the differences in gas flow rate and deposition time. Spectral lineshapes were monitored to ensure no clustering compounds were formed.

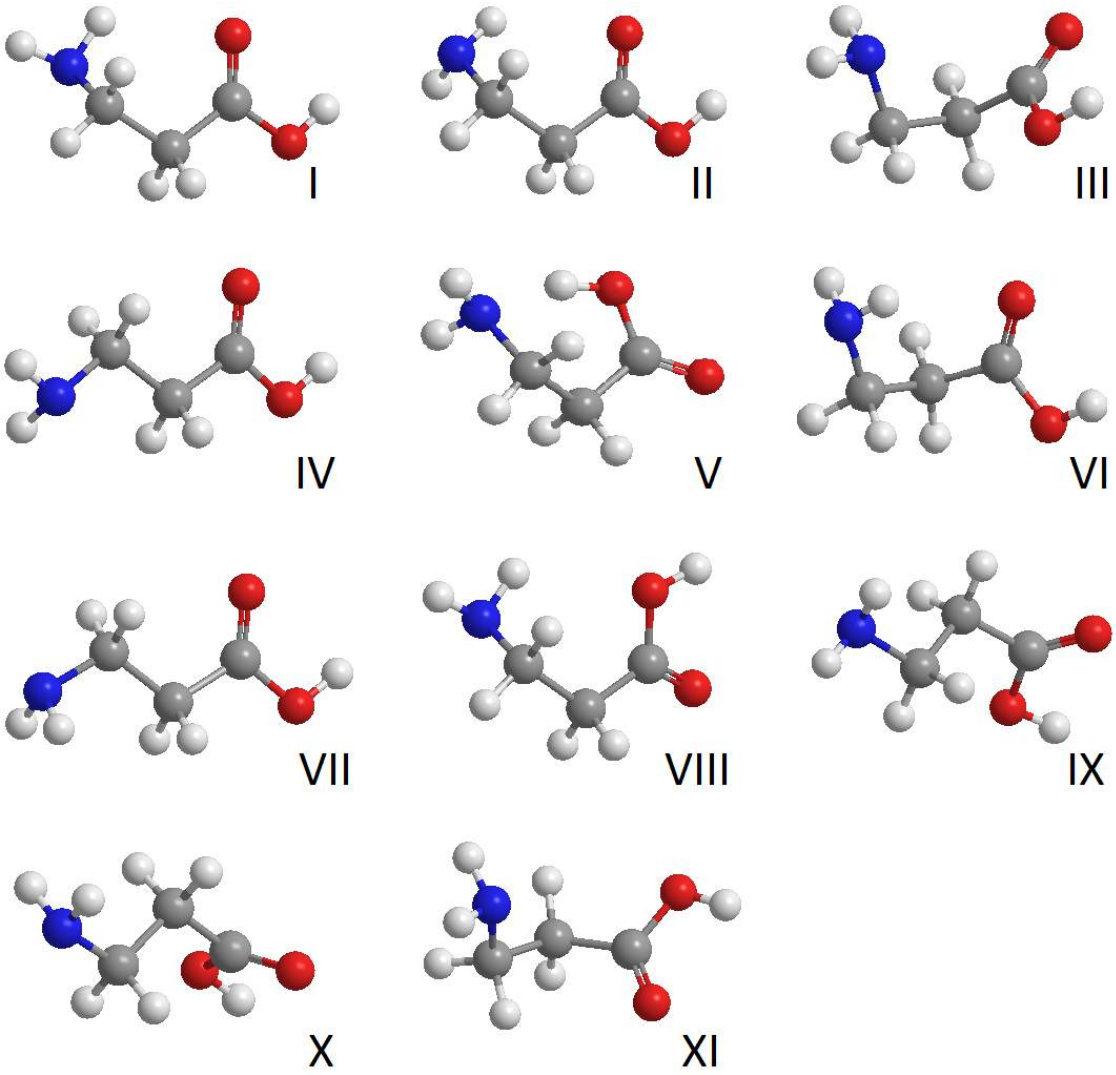

Figure 5.1: Structures of the eleven lowest energy β-alanine conformers using Ramek's nomenclatures. All conformers, except for VII, belong to the C_1 point group. Conformer VII belongs to the C_s point group.

For *in-situ* photoirradiation, the deposited samples were irradiated for 4 hrs straight, using a modified deuterium lamp. The results acquired were mainly employed to aid with spectral assignment, as β-alanine were shown to undergo conformational conversion upon UV-irradiation over an extended period of time.

The optical measurements were obtained using a FTIR spectrometer, with all spectra recorded at 0.2 cm^{-1} resolution and 1000 number of measurements. The obtained spectral bands were fitted with a Lorentzian function in order to obtain the corresponding band heights, widths and areas.

Quantum calculations were performed at the $B3LYP/aug-cc-pVTZ$ level of theory. The structures of the β-alanine conformers obtained by Stepanian *et al.* [19] were used as initial geometries for geometry optimizations of the eleven lowest energy conformers (Figure 5.1). Vibrational wavenumbers and IR absorption intensities were calculated analytically after tight optimization of each geometry. All calculated

vibrational wavenumbers were found to be real, which indicates that the eleven conformers were all local minimum conformers. In this paper, all β-alanine conformers are denoted using Ramek's nomenclatures [57].

5.1.2 Solid Parahydrogen Matrix-Isolated Spectra of β-alanine

In this section, we present the results regarding the conformational composition and the UV-irradiation behaviour of β-alanine in a solid parahydrogen matrix. The conformers of β-alanine were identified by comparisons between the experimental spectrum obtained (Figures A.1 and A.2 of Appendix) and the theoretical wavenumbers and intensities of the eleven lowest energy conformers (Table A.1 of Appendix). The ZPE corrected relative energies and the relative Gibbs free energies of the eleven conformers (Table 5.1) were also taken into consideration in the course of the assignments. The experimental and the theoretical wavenumbers and intensities of all observed β-alanine bands are listed in Table 5.2. Upon *in-situ* UV-irradiation, peak intensities were observed to change with different behaviours (Figures A.3 and A.4 of Appendix). Overlapping peaks contained within various wide bands were resolved after the UV-irradiation. Peaks which increased and decreased in intensity upon irradiation are shown by "+" and "-", respectively, in Table 5.2.

Table 5.1: ZPE-corrected relative energies, ΔE, and relative Gibbs free energies at 390 K, ΔG_{390K}, of the eleven lowest energy β-alanine conformers calculated by B3LYP/aug − cc − pVTZ.

Conformer	I	II	III	IV	V	VI	VII	VIII	IX	X	XI
ΔE, kJ mol^{-1}	0.00	1.98	7.43	3.90	1.53	6.38	5.36	7.89	7.73	7.07	6.10
ΔG_{390K}, kJ mol^{-1}	0.00	1.35	6.80	1.52	4.73	3.12	1.80	6.16	3.57	3.27	4.10

We expect conformer I to occur predominantly in the matrix as it is the lowest energy conformer. The stability of this conformer can be attributed to its intramolecular N-H—O bond. A comparison between experimental and theoretical spectra confirmed that some of the most intense experimental bands correspond to conformer I. These bands were observed to decrease in intensity upon UV-irradiation. Bands that also decreased in intensity but could not be assigned to conformer I were deduced to originate from conformers II and VII. Bands that increased in intensity upon irradiation agreed with the theoretical spectra of conformers III and IV.

A more detailed analysis is described below. The presence of certain conformers is explained based on the FTIR spectra in the spectral regions of the NH_2 wagging modes ($\omega(NH_2)$), the C-O stretching/OH bending modes (ν(C-O)/δ(OH)), the C=O stretching modes (ν(C=O)), and the OH stretching modes (ν(OH)), respectively. These are some of the most intense peaks in the derived spectra of β-alanine conformers. The assignment of other regions of the spectra can be found in Table 5.2.

Region of the $\omega(NH_2)$ Vibrational Mode (770 - 840 cm^{-1})

In this spectral region, five peaks were clearly resolved consisting of different UV-irradiation behaviours (Figure 5.2). This indicates that some or all peaks are due to different β-alanine conformers. According to

Table 5.2: Experimental wavenumbers (ν, cm^{-1}), peak heights (h, arbitrary unit) and spectral linewidths (w, cm^{-1}) of β-alanine sublimed at 390 K trapped in solid parahydrogen and argon matrices. The corresponding theoretical wavenumbers (ν, cm^{-1}) and intensities (I, $km \cdot mol^{-1}$) were calculated by B3LYP/aug − cc − pVTZ.

Experimental							Calculation[a]			
Parahydrogen			Argon			UV[b]	B3LYP/aug-cc-pVTZ		Conf.	Assignment[c]
ν_{pH2}	h_{pH2}	w_{pH2}	ν_{Ar}	h_{Ar}	w_{Ar}		ν_{B3LYP}	I_{B3LYP}		
3571.5[d]	0.65	0.10	3574.1	3.41	0.19	+	3573.8	65.04	III[e]	OH str
						+	3567.6	61.25	IV	OH str
			3569.2	0.41	0.17	-				
			3566.9	0.58	0.19	-				
			3564.5	0.63	0.25	-				
3569.3	2.82	0.26	3561.2	2.75	0.43	-	3567.2	62.66	I	OH str
							3564.2	60.16	II[f]	
							3563.9	55.74	VII[f]	
3567.8	5.85	0.22				-	3564.2	60.16	II	OH str
							3563.9	55.74	VII	OH str
			3557.3	0.31	0.31	-				
			3551.5	0.29	0.35	-				
			3549.2	0.39	0.23	-				
3525.5	0.04	0.67	3526.4	0.20	0.53	-				
			3515.0	0.65	0.80	-				
3416.2	0.05	0.26				-	3420.5	6.85	II	NH_2 str as
3412.2	0.30	0.52	3410.0	0.09	0.30	-	3418.0	8.12	I	NH_2 str as
3347.5	0.08	0.69				-	3345.2	3.25	I	NH_2 str s
2973.0	0.15	0.78				+	2961.0	19.47	III	$C\alpha H_2$ str as; $C\beta H$ str
2960.6	0.23	0.48				-	2942.2	21.51	II	$C\beta H_2$ str as
2956.3	0.91	0.54				-	2924.5	27.50	I	$C\beta H$ str
2937.5	0.11	0.42				+				
2929.3	0.36	0.42	2926.2	0.16	0.25	-	2903.2	29.52	II	$C\beta H$ str s
2920.0	0.35	0.34				-	2901.3	10.24	I	$C\alpha H_2$ str s
2891.2	0.09	0.61				-				
2883.7	0.08	0.31				+	2898.6	8.05	IV	$C\alpha H_2$ str s
2876.9	0.86	0.74				-	2840.2	60.14	I	$C\beta H$ str
2858.0	0.05	0.37				-				
2810.0	0.14	0.87				-				
2801.0	0.06	0.66				-				
2774.0	0.05	0.46				-				
			1785.2	0.49	0.32	-				
			1782.1	0.53	0.25	-				
1781.2	2.19	0.53				+	1782.0	339.53	III	C=O str
			1777.9	0.51	0.32	-				
1771.1	10.96	0.39	1771.4	7.85	0.21	-	1770.9	267.48	I	C=O str

Experimental							Calculation[a]			
Parahydrogen			Argon			UV[b]	B3LYP/aug-cc-pVTZ		Conf.	Assignment[c]
ν_{pH2}	h_{pH2}	w_{pH2}	ν_{Ar}	h_{Ar}	w_{Ar}		ν_{B3LYP}	I_{B3LYP}		
1762.3	1.22	0.65	1767.4	2.72	0.73	+	1776.9	297.79	IV	C=O str
			1758.1	0.97	0.85	-				
1734.3	2.80	0.52	1736.2	1.07	0.77	-	1752.7	282.32	II	C=O str
1733.7	0.65	0.52	1732.1	1.10	0.74	-				Fermi resonance
1717.3	0.19	0.52	1713.8	1.02	0.83	+				Association
1478.8	0.12	0.20				-	1481.3	4.38	I	$C\beta H_2$ scissor
1475.6	0.08	0.15				-				
1465.8	0.28	0.26	1462.5	0.23	0.91	-				
1448.7	0.24	0.30	1446.5	0.16	1.31	-				
1440.0	1.32	0.42				+	1439.0	14.01	IV	$C\alpha H_2$ scissor
1436.5	0.01	0.05	1436.6	0.11	0.56	-	1433.7	12.42	VII	$C\alpha H_2$ scissor
1431.9	0.18	0.97				-	1427.7	20.49	II	$C\alpha H_2$ scissor
1425.0	0.55	0.30				-	1423.4	20.70	I	$C\alpha H_2$ scissor
1422.0	1.44	0.89	1422.2	0.42	0.86	+	1414.4	46.82	IV	$C\beta H_2$ wag
1411.5	0.54	0.50	1411.6	0.82	1.11	-	1405.5	12.58	I	$C\beta H_2$ wag
1408.0	1.11	0.57	1408.5	0.40	0.52	+	1364.9	44.13	IV	$C\alpha H_2$ wag
1398.2	0.62	0.40	1396.6	0.63	1.78	-	1390.4	55.27	VII	$C\alpha H_2$, $C\beta H_2$ wag
			1387.1	0.81	0.68	-	1389.1	28.28	II	$C\alpha H_2$ wag
1382.7	1.35	0.53	1381.1	0.83	0.48	-	1386.9	56.23	I	$C\alpha H_2$ wag
1364.9	0.30	0.56	1366.4	0.35	1.80	+				
1345.3	0.21	0.54				-	1359.0	34.74	II	$C\beta H_2$ wag
1336.9	0.34	0.65				-				
1298.7	0.39	0.53				-	1289.3	7.86	I	OH bend
1268.4	0.38	0.66				-				
1261.9	0.06	0.32	1261.3	0.17	0.70	-				
1247.5	0.40	0.51	1245.1	0.61	0.75	+	1246.4	7.88	IV	$C\alpha H_2$ twist
1230.3	0.22	0.50	1229.3	0.26	0.54	-	1234.8	14.84	II	$C\alpha H_2$ twist
1225.3	0.06	0.07	1224.5	0.47	0.67	-				
1219.4	0.20	0.13	1221.4	0.30	0.22	-	1217.0	2.33	I	$C\alpha H_2$ twist
1209.4	0.08	0.28				+				
			1188.8	0.16	0.27	+				
			1184.3	0.11	0.16	-				
			1180.5	0.42	0.43	-				
1178.5	2.79	0.47	1177.0	1.52	0.19	-	1182.7	83.86	I	OH bend; NH_2, $C\beta H_2$ twist
			1175.5	1.65	0.11	-				
1165.0	0.49	0.50				-	1173.8	70.21	II	OH bend; NH_2, $C\alpha H_2$ twist

Experimental							Calculation[a]			
Parahydrogen			Argon			UV[b]	B3LYP/aug-cc-pVTZ		Conf.	Assignment[c]
ν_{pH2}	h_{pH2}	w_{pH2}	ν_{Ar}	h_{Ar}	w_{Ar}		ν_{B3LYP}	I_{B3LYP}		
1153.0	0.63	0.50	1152.7	0.35	0.39	-	1128.4	241.69	VII	C-O str; OH bend
			1143.8	0.32	0.43	-				
			1123.6	0.22	0.28	-				
1119.3	2.91	0.38	1113.4	2.47	0.37	+	1114.6	209.07	IV	C-O str; OH bend
1113.8	10.93	0.31	1110.5	8.98	0.13	-	1108.9	225.45	I	C-O str; OH bend
							1107.9	204.42	II[e]	C-O str; OH bend
			1108.7	3.54	0.11	-	1107.9	204.42	II	C-O str; OH bend
1106.2	0.61	1.21				-	1092.9	11.75	I	CN, CαCβ str
1101.3	0.35	0.50				+	1099.7	101.35	III	C-O str; OH bend
1099.0	0.33	0.49	1099.3	0.37	0.46	-	1061.2	84.29	VII	CN str
			1090.1	0.22	0.56	-				
1084.1	0.40	1.04	1083.9	0.23	0.66	+	1082.1	15.56	IV	CαCβ str; NH_2 tor
1065.2	0.20	0.79				-				
1057.5	0.05	0.24				+	1066.3	31.78	III	CN str; CαCβ tor
1044.3	1.02	0.67	1047.3	0.54	0.73	-	1047.6	23.26	I	CN str; CαCβ tor
			1043.2	0.41	0.96					
998.5	0.91	0.69				-	1009.9	18.93	II	CαCβ str; NH_2 tor
977.8	0.24	0.64				+	993.7	37.63	III	CαCβN bend
954.5	0.16	0.01				+	971.7	16.87	IV	CαCβ str; NH_2 tor
953.1	0.23	0.23				-				
939.3	1.05	0.13				-	933.4	2.34	I	CαCβ, CCα str; NH_2 tor
921.8	0.22	0.37				+				
894.2	0.16	0.28				-				
889.2	0.43	0.67				-				
884.2	0.80	0.33	886.1	0.45	0.57	-	882.8	29.47	I	CαCβN bend
846.3	0.46	0.29	845.7	0.18	0.09	-				
841.6	0.13	0.76				-				
823.7	1.26	0.66	822.1	0.68	0.28	-				
822.7	1.46	0.37	818.8	0.71	0.17	-	836.0	86.00	I	NH_2 wag
819.9	2.96	0.13	817.3	4.54	0.13	-	820.1	174.52	II	NH_2 wag
			812.7	0.55	0.11	-				

Experimental							Calculation[a]			
Parahydrogen			Argon			UV[b]	B3LYP/aug-cc-pVTZ		Conf.	Assignment[c]
ν_{pH2}	h_{pH2}	w_{pH2}	ν_{Ar}	h_{Ar}	w_{Ar}		ν_{B3LYP}	I_{B3LYP}		
809.6[d]	0.89	0.33	809.4	0.58	0.10	+	821.6	73.87	IV	NH_2 wag
						+	811.6	30.09	III[e]	CCα str
803.4	0.10	0.06	804.7	0.11	0.14	-				
797.9	0.69	0.51	800.5	0.71	0.14	-	795.1	206.46	VII	NH_2 wag
781.8[d]	2.00	0.31	783.5	0.51	0.16	-	787.7	11.73	I	CCα str; $C\beta H_2$
						+	783.7	49.44	IV[e]	rock CαCβN
						+	776.8	95.84	III[e]	tor NH_2 wag
			778.6	1.14	0.23	+	783.7	49.44	IV	CαCβN tor NH_2 wag

[a] Scaling factors: 0.955 for vibrational modes with wavenumbers greater than 2000 cm^{-1}, 0.985 for all other vibrational modes. [b] "+" indicates that the corresponding peak intensity increased upon UV-irradiation, while "-" indicates those which decreased. [c] asy - asymmetric, bend - bending, rock - rocking, scissor - scissoring, str - stretching, s - symmetric, tor - torsion, twist - twisting, wag - wagging. [d] UV-irradiation indicated overlapping of multiple peaks. [e] Assignment applicable to solid parahydrogen matrix isolation spectra only. [f] Assignment applicable to solid argon matrix isolation spectra only. Note experimental bands in the region of approximately 1520 cm^{-1} to 1700 cm^{-1} are not listed in the table. These assignments were difficult due to the interference of water absorption.

the theoretical calculation, a peak due to conformer I is expected to be observed at a high wavenumber in this region with a strong intensity, as it has a theoretically predicted wavenumber of 836.0 cm^{-1} and it is the most stable conformer of β-alanine. Two intense peaks were observed in the high wavenumber region at 819.9 cm^{-1} and 822.7 cm^{-1}. If we assign the peak at 822.7 cm^{-1} to conformer I, the peak at 819.9 cm^{-1} can be assigned to conformer II since (1) the theoretically calculated wavenumber (820.1 cm^{-1}) is slightly lower than that of conformer I, (2) the predicted intensity is larger than that of the corresponding peak of conformer I, and (3) conformer II is the third lowest energy conformer among the eleven conformers (Table 5.1), therefore a large abundance is expected. The assignment of the peaks due to conformers I and II also suggests that the difference between the theoretical and the experimental wavenumbers in this region is expected to be within 15 cm^{-1}. Referring to the calculated wavenumbers, intensities and the stability of conformers, the band at 797.9 cm^{-1} was attributed to conformer VII. Bands corresponding to conformers I, II and VII were all observed to decrease in intensity upon UV-irradiation (Figure 5.2b). The difference spectrum shows that the peaks occurring at 809.6 cm^{-1} and 781.8 cm^{-1} increased in intensity upon UV-irradiation, and were resolved into multiple sharp peaks. These bands were attributed to conformers III and IV based on similar assignment criteria as described above. Besides peaks corresponding to conformers I, II, III, IV and VII, unassigned bands with minor intensities, such as the peak at 803.4 cm^{-1}, are still present in this region. These bands could not be allocated consistently to any theoretically predicted peaks.

Region of the ν(C-O)/δ(OH) Vibrational Modes (1090 - 1160 cm^{-1})

The presence of conformers I, II, III, IV and VII deduced by the spectral analysis in the $\omega(NH_2)$ region was also confirmed in the ν(C-O)/δ(OH) region (Figure 5.2). Two peaks at 1113.8 cm^{-1} and 1153.0 cm^{-1} in the ν(C-O)/δ(OH) region reduced in intensity upon UV-irradiation. The spectral analysis in the $\omega(NH_2)$ region revealed that conformers I, II and VII were observed to have the same behaviour upon UV-irradiation. From the theoretical wavenumbers, the peak at 1153.0 cm^{-1} can be assigned to conformer VII, whose theoretical wavenumber is 1128.4 cm^{-1}. The calculation showed comparable intensities between the ν(C-O)/δ(OH) and the $\omega(NH_2)$ modes, which also supports the assignment. The band located at 1113.8 cm^{-1} was ascribed to both conformers I and II, whose theoretical wavenumbers are 1108.9 cm^{-1} and 1107.9 cm^{-1}, respectively. Due to the proximity of the calculated wavenumbers, these peaks are expected to overlap completely. Peaks at 1101.3 cm^{-1} and 1119.3 cm^{-1} showed an increase in intensity upon UV-irradiation. Referring to the theoretical values, these peaks were assigned to conformers III and IV, respectively.

Region of the ν(C=O) Vibrational Mode (1725 - 1790 cm^{-1})

The most intense band (at 1771.1 cm^{-1}) and the second most intense band (at 1734.3 cm^{-1}) in this region showed a decrease in intensity upon UV-irradiation, and therefore these were attributed to conformers I and II, respectively. Their theoretical wavenumbers are 1770.9 cm^{-1} and 1752.7 cm^{-1}, respectively, which are in good agreement with the observed wavenumbers. The ν(C=O) modes of conformers IV and III, whose theoretical wavenumbers are 1776.9 cm^{-1} and 1782.0 cm^{-1}, respectively, were identified at 1762.3 cm^{-1} and 1781.2 cm^{-1}, respectively. These bands showed an increase in intensity upon UV-irradiation. The band originating from the ν(C=O) mode of conformer VII, predicted at 1777.4 cm^{-1}, was unobserved as it is most likely masked by the presence of other peaks.

Region of the ν(OH) Vibrational Mode (3560 - 3580 cm^{-1})

The spectral region of the ν(OH) vibrational mode showed only one feature, which results from the overlap of multiple peaks. Upon UV-irradiation, the peaks at 3567.8 cm^{-1} and 3569.3 cm^{-1} deceased in intensity, while the peak at 3571.5 cm^{-1} was resolved into two components which increased in intensity. Based on the calculated wavenumbers and these UV-irradiation behaviours, the peak at 3567.8 cm^{-1} was assigned to conformers II and VII, and the peak at 3569.3 cm^{-1} was attributed to conformer I, and the two resolved bands were assigned to conformers IV and III, respectively.

Other Spectral Regions

From the regions of $\omega(NH_2)$, ν(C-O)/δ(OH), ν(C=O) and ν(OH) vibrational modes, we were able to deduce the presence of five conformers, conformers I, II, III, IV, and VII, in solid parahydrogen, and obtain their corresponding UV-irradiation behaviour. The bands in the remaining regions were then assigned according to these results, and also the theoretical wavenumbers and intensities. The majority of the bands in the recorded spectra originated from conformer I due to its large abundance in the matrix. Out of its twenty-four theoretical bands in the region of 700 cm^{-1} - 4800 cm^{-1}, all but three were identified experimentally.

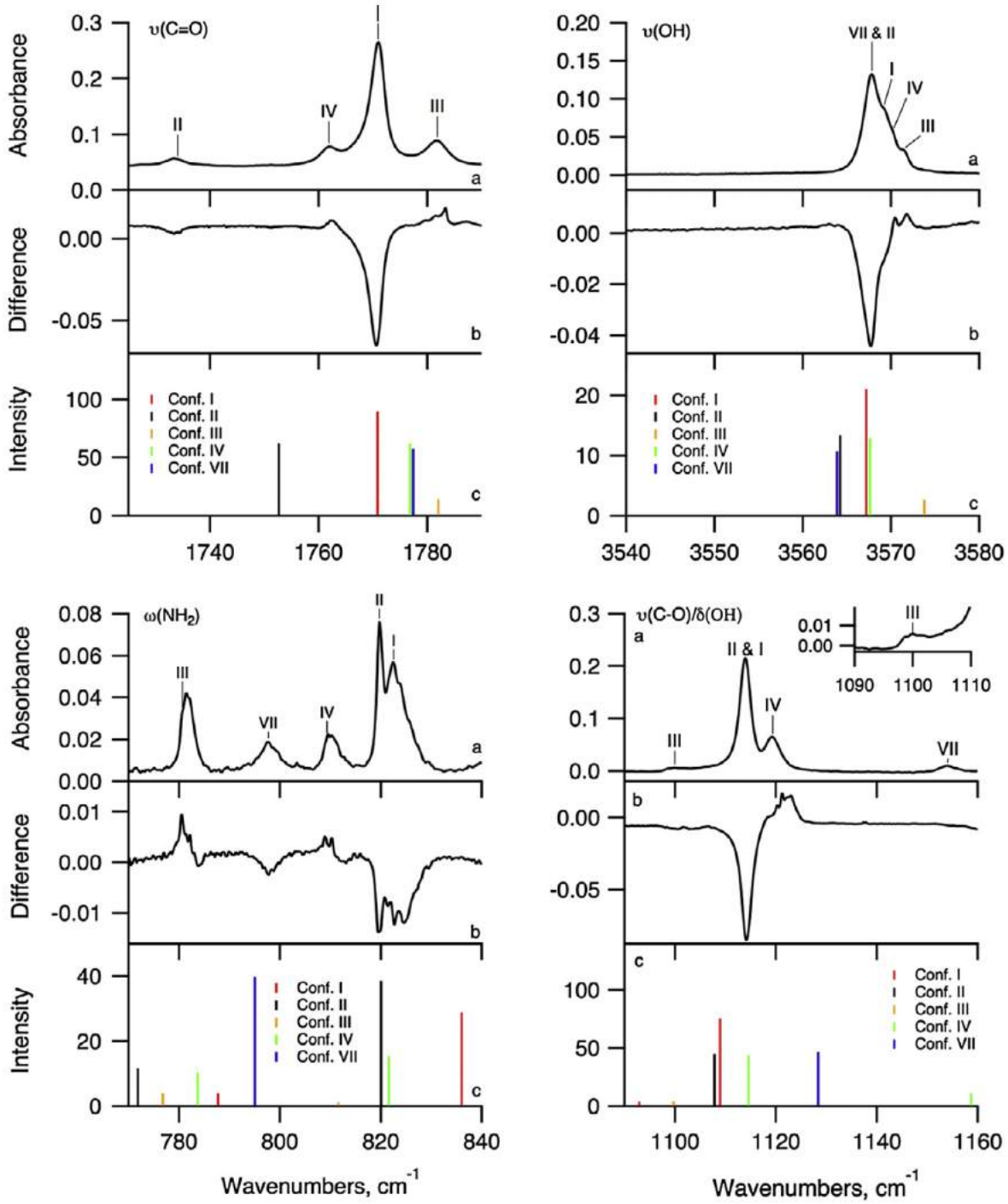

Figure 5.2: FTIR spectra of β-alanine sublimed at 390 K and isolated in a parahydrogen matrix (T = 4 K) taken from regions of ν(OH), ν(C=O), ν(C-O)/δ(OH), and $\omega(NH_2)$. Panel (a) shows the spectrum recorded immediately after deposition. Panel (b) is the difference spectrum obtained by subtracting the deposition spectrum from the spectrum observed after 4 hrs of UV-irradiation. Panel (c) shows the theoretically predicted vibrational wavenumbers assuming a Boltzmann distribution at 390 K. The theoretical wavenumbers are corrected by a factor of 0.955 for vibrational modes which are derived to be above 2000 cm^{-1}, and 0.985 for all other vibrational modes. The conformational assignment is given at each peak by Ramek's nomenclatures.

Conformer II is the second most stable conformer out of the five found in our matrix. This conformer is stabilized by an intramolecular N-H—O bond as is the case in conformer I. Due to the structural similarity between conformers I and II, many of the corresponding vibrational bands are expected to overlap. Consequently, only twelve vibrational bands were assigned to conformer II. The structure of conformer IV differs considerably from that of conformers I and II. As a result, the corresponding bands were more resolved, and twelve vibrational bands were attributed to conformer IV despite its instability as compared to conformer II. Since conformers VII and III are unstable compared to the other detected conformers, only six and eight bands, respectively, with intensities predicted to be large were identified.

Upon UV-irradiation, bands corresponding to conformers I, II, and VII were found to reduce in intensity, while bands from conformers III and IV increased in intensity. Since conformers I and II are the most stable among these five conformers, UV excitation by 200 nm - 250 nm radiation induces conformational changes in β-alanine to less stable structures via electronically excited states.

Conformer III is stabilized by an n - π^* interaction by the delocalization of electron density from the non-bonding orbital of the nitrogen to the anti-bonding orbital of the carbonyl group [59], but its free energy is 6.8 kJ·mol^{-1} higher than the lowest conformer I. Its population is about a few percent at the sublimation temperature of 390 K. Conformer III has been detected by Sanz *et al.* [59] by the laser ablation technique using microwave spectroscopy, but no vibrational spectroscopy has been reported. This is the first time the presence of conformer III in a matrix environment has been confirmed.

5.1.3 Comparison between Conformational Composition of β-alanine in a Parahydrogen Matrix and in an Argon Matrix

The conformational composition of β-alanine was also investigated in an argon matrix (Figures A.5, A.6, A.7 and A.8 of Appendix). Spectral assignment was performed similarly to our analysis of the spectra in solid parahydrogen. As a result, four β-alanine conformers, conformers I, II, IV and VII, were identified and assigned in an argon matrix (Table 5.2). Twelve, seven, nine and six vibrational modes were assigned experimentally for conformers I, II, IV and VII, respectively.

The vibrational wavenumbers of the peaks detected in a parahydrogen matrix and in an argon matrix were observed to differ by less than 9 cm^{-1}. It was found that the spectral linewidth of β-alanine in solid argon was slightly narrower than that in solid parahydrogen. Spectral linewidths of rotationally resolved vibrational transitions in solid parahydrogen were reported to be much narrower than those in rare gas matrices due to a long rotational decoherence time in solid parahydrogen [32, 37, 102–104]. In the case of β-alanine, rotational motion is completely quenched even in solid parahydrogen. The broader linewidth in solid parahydrogen indicates that the vibrational decoherence time is much shorter in solid parahydrogen than in solid argon. Because of the narrower linewidth, the argon spectra were used to resolve some of the overlapping bands detected in the parahydrogen spectra, in particular, the bands corresponding to the ν(C-O)/δ(OH) of conformers I and II. Contrary to expectations, the slightly broader linewidth in parahydrogen crystals is less desirable for matrix isolation spectroscopy of amino acids.

The effect of UV-irradiation in an argon matrix is similar to that in a parahydrogen matrix - conformers I, II and VII decreased in intensity, and conformer IV increased in intensity (Figure 5.3). However, the change

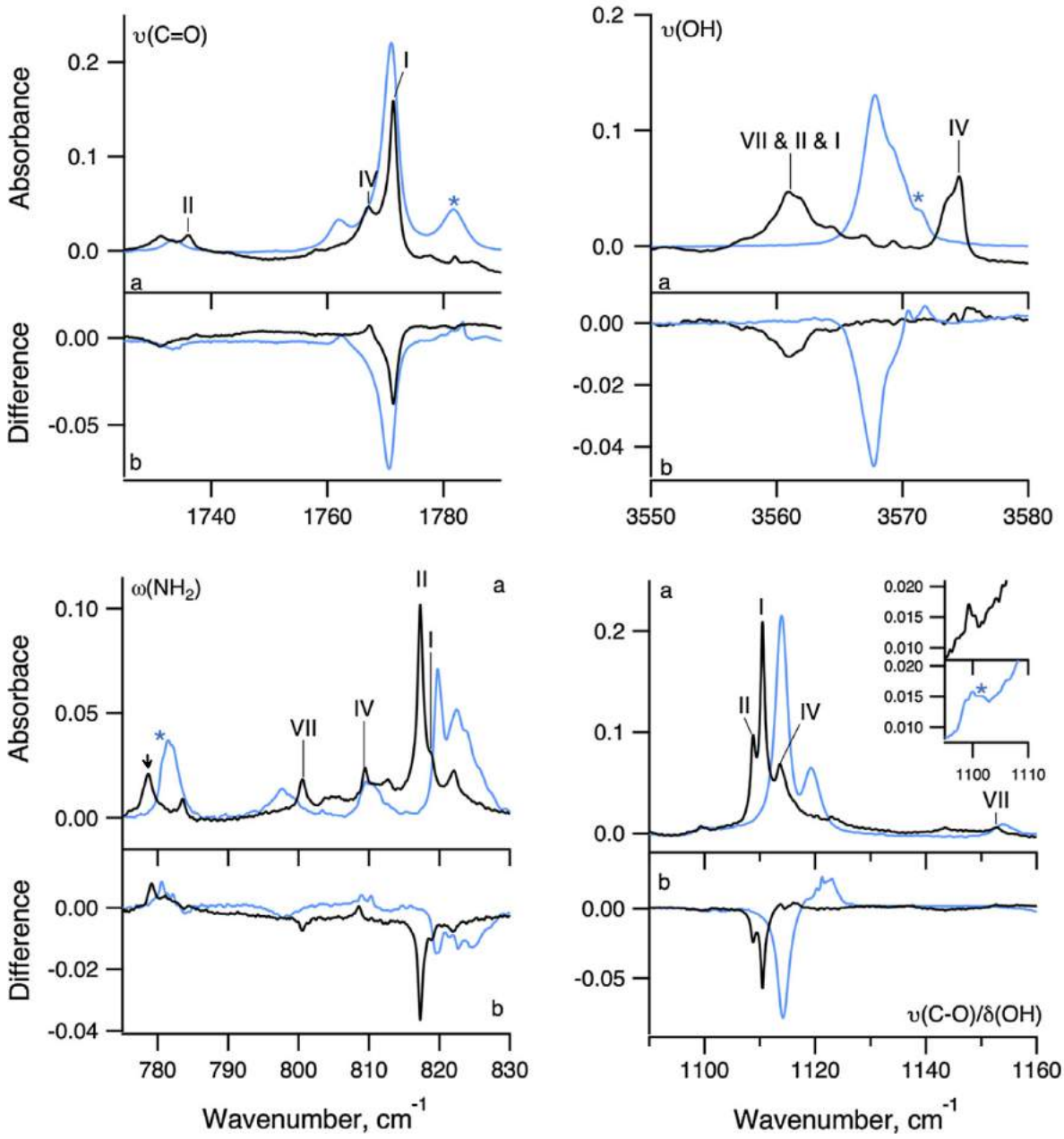

Figure 5.3: FTIR spectra of β-alanine sublimed at 390 K taken from regions of ν(OH), ν(C=O), ν(C-O)/δ(OH), and $\omega(NH_2)$ in solid parahydrogen (blue trace) and in solid argon(black trace). Each panel consists of (a) a spectrum taken immediately after deposition, and (b) a difference spectrum obtained by subtracting the deposition spectrum from the spectrum observed after 4 hrs of UV-irradiation. The assignments of conformers are given in each argon spectrum. "*" mark the bands of conformer III, which were observed in the solid parahydrogen spectrum but not in the argon spectrum. The band marked by "↓" in the $\omega(NH_2)$ region is assigned to another vibrational mode associated with conformer IV.

in intensity upon irradiation was less pronounced in solid argon. The intensity of conformer I decreased by 14 % in parahydrogen matrices after 4 hrs UV-irradiation, while it decreased by 10 % in argon matrices under the same irradiation condition. The larger conformational change found in parahydrogen matrices is due to the softer environment provided by these matrices as compared to the rare gas matrices. The softness of the parahydrogen matrix environment is a result of the quantum nature of solid hydrogen (see Section 2.1.2). As a consequence, *in-situ* photoirradiation results in more conformational changes in parahydrogen matrices than in argon matrices.

Conformer V was unobserved in both solid parahydrogen and argon matrices in our experiments, as opposed to what was previously reported. Stepanian *et al.* [19] reported that the ν(OH) stretching mode of conformer V was observed at 2982.8 cm^{-1} in an argon matrix. We did not observe any peaks in this spectral region in an argon matrix or in a parahydrogen matrix. Furthermore, none of the observed bands in the regions of $\omega(NH_2)$, ν(C-O)/δ(OH), and ν(C=O) agree with the theoretical wavenumbers and intensities of the corresponding modes of conformer V. Thus, the presence of conformer V is unsupported by our experimental results. Indeed, the free energy of conformer V is relatively high at 390 K, although its ZPE-corrected energy is low (see Table 5.1).

5.1.4 Sublimation Temperature Dependence of β-alanine Conformational Population in Solid Parahydrogen

We attempted to investigate the correlation between sublimation temperature and conformational population ratio of gas phase β-alanine in solid parahydrogen, by introducing our sample into the matrices at different sublimation temperatures of 390 K and 380 K. All β-alanine conformers which were observed at 390 K were also detected at 380 K. We then tried to obtain the relative abundance of each conformer at deposition by extracting the experimental peak areas and weighing them by the theoretical intensities. However, we found this task quite impossible to accomplish due to the presence of unresolved overlapping peaks involving multiple conformers. As we could not accurately calculate the population of each conformer from our data, we aborted this study for β-alanine, and reinvestigated it on another amino acid, namely α-alanine.

5.2 Conformational Analysis of Gaseous α-alanine in Solid Parahydrogen and Argon Matrices

Similar to β-alanine experiment, we investigated the conformational stability of α-alanine in solid parahydrogen using FTIR spectroscopy, and compared the results to those in argon matrices. We mainly analyzed the correlation between sublimation temperature and conformational population ratio of gaseous α-alanine in both matrices. We also explored the effect of UV-irradiation on α-alanine by performing *in-situ* photoirradiation.

We have prepared a manuscript on our result for publication in the near future [4]. The following subsections are mostly copies from our written draft, with minor editions and rearrangements to accommodate the format and coherency of this thesis.

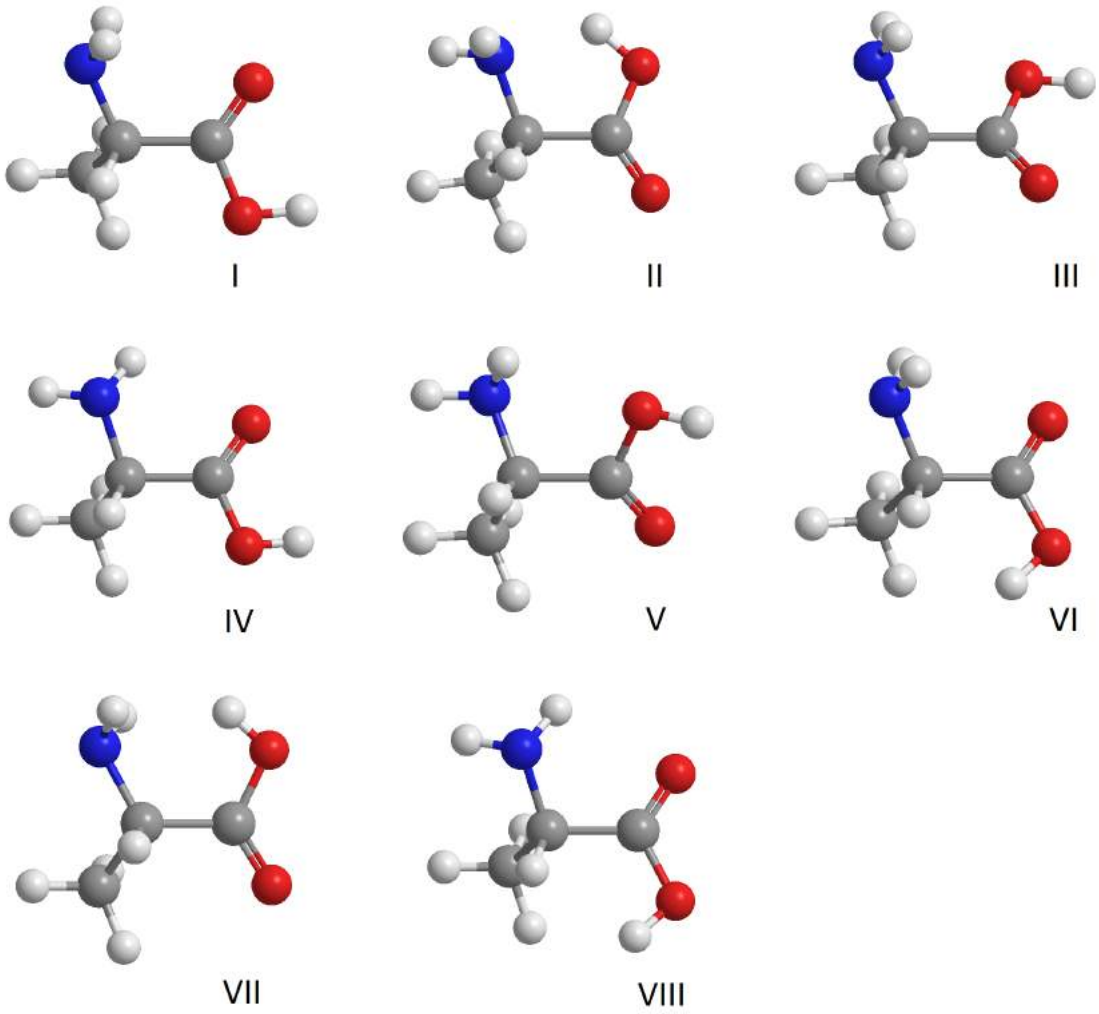

Figure 5.4: Structures of the eight lowest energy α-alanine conformers using Cs*ászár*'s nomenclatures and Baladin's geometric configurations. All conformers presented are in the L-form of α-alanine enantiomer. Therefore, we omitted the "A" and "B" labels which accompanied the L- and D-enantiomers, respectively, in Cs*ászár*'s notations.

5.2.1 Experimental and Computational Details for α-alanine Conformational Study

This section highlights the experimental and computational specificities applied in our α-alanine conformational study. The general set-ups and procedure have been described previously (see Chapter 3).

The α-alanine gas and the matrix gas were simultaneously deposited directly onto a BaF_2 cold window for 30 min at a gas flow rate of 5 ccm, for both solid parahydrogen and argon matrix experiments. α-alanine gas was obtained by subliming the α-alanine sample (L-α-alanine, Sigma Aldrich, $\geq$99.5 % purity, used as received) using a built-in house copper Knudsen cell. The sample was sublimed at a temperature of 420$\pm$1 K in order to identify the conformers present in the matrices and to investigate the effects of *in-situ* UV-irradiation, and also at temperatures of 410$\pm$1 K and 430$\pm$1 K in order to study the relationship between conformational population and sublimation temperature. Thermal decomposition of α-alanine was

monitored for all experiments, and no degradation products were observed. The molar ratio of matrix gas to α-alanine was unknown for all experiments. However, formation of clusters was monitored by examining the spectral line shapes.

For the *in-situ* UV-irradiation experiments, a modified deuterium lamp was employed, and the deposited samples were irradiated for 4 hrs in total, with a spectrum recorded at each hour of irradiation.

The optical measurements were obtained using a FTIR spectrometer, with all spectra recorded at 0.2 cm^{-1} resolution and 1000 number of measurements. The obtained spectral bands were fitted with a Gaussian and/or Lorentzian function in order to obtain the corresponding band heights, widths and areas.

The structures of the eight stable L-α-alanine configurations found by Balabin [70] was employed as a foundation for geometry optimization at the B3LYP/aug$-$cc$-$pVTZ level of theory (Figure 5.4). All α-alanine conformers in this study are denoted using C*sászár*'s nomenclatures [69]. The corresponding ZPE-corrected relative energies, the relative Gibbs free energies, and the theoretical vibrational wavenumbers and intensities were derived in order to interpret our experimental FTIR spectra. Tight optimization of each geometry was first performed, and the vibrational wavenumbers were then calculated analytically. The eight conformers were found to be local minimum conformers as all of the derived vibrational wavenumbers were calculated to be real.

5.2.2 Conformers of Gaseous α-alanine Isolated in Solid Parahydrogen and Argon Matrices

The conformational compositions of α-alanine in our parahydrogen matrix and in our argon matrix were identified by comparing the spectra obtained immediately after deposition (Figures B.1 and B.1 of Appendix, respectively) with the calculated wavenumbers and intensities (Table B.1 of Appendix) of the eight lowest energy conformers, while taking into consideration the corresponding ZPE-corrected relative energies and the relative Gibbs free energies (Table 5.3). In order to identify peaks which result from site splitting in an argon matrix environment, we also performed annealing experiments and compared the corresponding spectrum (Figure B.3 of Appendix) with the spectrum recorded immediately after deposition in an argon matrix.

Table 5.3: ZPE-corrected relative energies, ΔE, and relative Gibbs free energies at 420 K, ΔG_{420K}, of the eight lowest energy α-alanine conformers calculated by B3LYP/aug$-$cc$-$pVTZ.

Conformer	**I**	**II**	**III**	**IV**	**V**	**VI**	**VII**	**VIII**
ΔE, kJ mol^{-1}	0.00	1.76	4.96	4.77	7.92	20.34	21.21	24.56
ΔG_{420K}, kJ mol^{-1}	0.00	4.34	3.80	5.72	8.43	20.33	22.56	25.38

We expect conformer I to be the most abundant in our matrices as it is the lowest energy conformer. We also anticipate the presence of conformer II, the third lowest energy configuration, as its occurrence in a matrix environment has been reported previously [45, 47, 80]. A comparison between the theoretical spectra and the experimental spectra reveals that the most predominant bands in our spectra indeed correspond to conformer I and II. Other unassigned bands still remain in our spectra after the allocation of the conformer I and conformer II bands. In the solid parahydrogen spectra, these bands were concluded to arise from

conformer IV and V; while in the argon spectra, no additional conformers were identified. In order to illustrate the presence of these conformers in our matrices, a more detailed analysis of the spectra is described below. The discussion will focus on four regions of the spectra: the region of the OH stretching modes (ν(OH)), the C=O stretching modes (ν(C=O)), the C-O stretching modes (ν(C-O)), and the NH_2 wagging modes ($\omega(NH_2)$), respectively, as these regions consist of the strongest theoretical vibrational motions. The spectral assignments of the remaining bands observed in our recorded spectra can be found in Table 5.4.

Region of the ν(OH) Vibrational Mode (3560 - 3580 cm^{-1})

In this region of the spectra, a peak associated with conformer I is derived to be observed at 3565.4 cm^{-1} (Figure 5.5a). This band is also predicted to be strong as conformer I is derived as the most stable configuration by the ZPE-corrected relative energies and the relative Gibbs free energies, hence it can be expected to occur with the greatest abundance in our matrices. In the solid parahydrogen spectrum (Figure 5.5b) a strong peak is detected at 3565.3 cm^{-1}, and thus was attributed to conformer I. In the argon spectrum (Figure 5.5c), a predominant band was observed at 3564.4 cm^{-1}. However, it was concluded to result from site splitting rather than conformational effects as it decreased drastically upon annealing (Figure 5.5d). As a result, the conformer I peak was attributed to the band at 3574.5 cm^{-1} instead. As compared to conformer I, conformer II consists of an intramolecular OH—N hydrogen bond which is absent in conformer I (Figure 5.4). Consequently, the ν(OH) band of conformer II was predicted to be downshifted with respect to the conformer I band. Such a band was observed at 3210.0 cm^{-1} in the solid parahydrogen spectrum and at 3196.0 cm^{-1} in the argon spectrum. Peaks corresponding to conformers IV and V were also identified in this region of the solid parahydrogen spectrum. According to the derived spectra, the bands of conformers IV and V should occur at a higher wavenumber than conformer I; moreover, conformers IV and V are calculated to be relatively unstable, thus they should be low in abundances and the corresponding bands should be weak in intensities. Two bands at 3577.5 cm^{-1} and at 3579.3 cm^{-1} were observed to fit these criteria in our solid parahydrogen spectrum and they were attributed to conformer IV and V, respectively. These bands were unobserved in the spectrum obtained in crystalline argon. Other unassigned bands were still present in this region of the solid parahydrogen spectrum after the allocation of bands corresponding to conformers I, II, IV and V, and the argon spectra after the identification of the bands corresponding to conformers I and II. We were unable to identify these bands as the corresponding wavenumbers and intensities disagree with what is predicted theoretically by our derived spectra and the calculated stability of the conformers.

Region of the ν(C=O) Vibrational Mode (1770 - 1805 cm^{-1})

From the ν(OH) region of the spectrum, there is evidence supporting the occurrence of four α-alanine conformers (conformer I, II, III and IV) in a parahydrogen matrix, and two conformers (conformer I and II) in an argon matrix. These conclusions are reached once again in this region of the spectra, thus further confirming our initial analysis. Based on the calculated spectra (Figure 5.5a), a peak corresponding to conformer I should be found at 1775.9 cm^{-1} with an intensity that is greater than the conformer I peak observed in the ν(OH) region. Furthermore, a weaker band due to conformer II can be anticipated to occur at a higher wavenumber than the conformer I band since conformer II is less stable than conformer I and

Table 5.4: Experimental wavenumbers (ν, cm^{-1}), peak heights (h, arbitrary unit) and spectral linewidths (w, cm^{-1}) of α-alanine sublimed at 420 K and trapped in solid parahydrogen and argon matrices. The corresponding theoretical wavenumbers (ν, cm^{-1}) and intensities (I, $km \cdot mol^{-1}$) were calculated by B3LYP/aug − cc − pVTZ. The brackets indicate bands due to site splitting.

Experimental						Calculation			
Argon			Parahydrogen			B3LYP/aug-cc-pVTZ		Conf.	Assignment[a]
ν_{Ar}	h_{Ar}	w_{Ar}	ν_{pH2}	h_{pH2}	w_{pH2}	ν_{B3LYP}[b]	I_{B3LYP}		
			3579.3	0.017	0.568	3574.7	66.80	V	OH str
			3577.5	0.007	2.963	3570.0	67.20	IV	OH str
			3567.2	0.258	0.737				
3574.5	0.186	1.758	3565.3	0.224	0.943	3565.4	56.11	I	OH str
3573.6	0.046	0.744							
3564.4	0.356	0.980							
3559.3	0.233	1.860							
3557.5	0.022	0.509	3559.4	0.004	0.304				
3555.9	0.049	1.280	3554.5	0.001	1.672				
3552.2	0.038	1.342							
3532.8	0.003	5.629	3541.8	0.003	4.379				
3526.2	0.007	9.160	3530.4	0.002	4.590				
3515.1	0.009	8.812	3518.4	0.001	6.492				
3505.2	0.008	7.523	3505.6	0.002	7.196				
3485.4	0.004	3.345	3490.4	0.004	4.289				
3480.5	0.005	1.689							
3463.0	0.005	1.066							
3425.9	0.001	1.431	3430.6	0.004	0.860	3434.1	10.97	II	NH_2 str asym
3423.6	0.004	6.533	3430.1	0.006	3.042				
			3397.9	0.004	4.749	3426.8	9.93	IV	NH_2 str asym
3398.7	0.011	4.396	3396.7	0.008	1.570	3407.2	4.57	I	NH_2 str asym
3390.5	0.006	5.783							
3377.6	0.005	92.053	3385.7	0.004	14.808	3361.1	1.38	II	NH_2 str sym
			3344.2	0.001	9.558				
			3263.7	0.003	7.886	3345.7	6.09	IV	NH_2 str sym
3234.4	0.009	23.437	3234.2	0.008	36.674	3338.5	1.67	I	NH_2 str sym
3196.0	0.012	14.491	3210.0	0.015	18.633	3322.6	247.63	II	OH str
			3187.3	0.001	1.004				
3163.3	0.005	1.203							
3003.8	0.019	4.620				2989.4	9.12	II	CH_3 str asym
3001.1	0.012	3.101	3003.2	0.049	2.104	2986.0	11.89	I	CH_3 str asym
2987.3	0.022	6.445							
2983.2	0.020	3.415	2982.9	0.078	1.980	2966.7	20.99	I	CH_3 str asym
			2964.4	0.001	11.596	2959.3	20.26	IV	CH_3 str asym

Experimental						Calculation			
Argon			Parahydrogen			B3LYP/aug-cc-pVTZ		Conf.	Assignment[a]
ν_{Ar}	h_{Ar}	w_{Ar}	ν_{pH2}	h_{pH2}	w_{pH2}	ν_{B3LYP}[b]	I_{B3LYP}		
2958.9	0.004	18.357							
2953.0	0.002	5.509							
2945.7	0.010	5.375	2943.8	0.018	8.383	2916.3	12.85	I	$C_\alpha H$ str
2938.5	0.005	17.111	2933.7	0.011	8.303	2901.8	11.25	I	CH_3 str sym
			2925.0	0.001	4.908				
2912.9	0.002	12.953	2915.2	0.004	19.081				
2887.7	0.006	5.931	2889.3	0.005	3.302	2902.1	20.27	II	$C_\alpha H$ str
2881.4	0.002	6.311	2886.5	0.006	13.710	2897.2	11.37	II	CH_3 str sym
			2843.0	0.001	10.222				
			2828.0	0.001	2.669				
			2775.1	0.000	5.927	2785.0	47.00	V	$C_\alpha H$ str
			2757.3	0.001	2.105				
			2740.2	0.001	3.470				
			2449.9	0.001	9.196				
			2430.7	0.001	2.572				
			2306.5	0.000	3.892				
			2263.7	0.000	9.332				
			2241.6	0.001	10.918				
2212.7	0.001	13.772	2216.7	0.003	6.831				
			2005.0	0.001	8.135				
1884.4	0.002	2.246	1894.3	0.002	8.136				
			1849.8	0.002	4.779				
1846.4	0.001	1.591	1846.7	0.002	2.292				
			1838.6	0.001	3.234				
1808.8	0.042	1.245	1809.6	0.018	4.033				
1793.3	0.032	4.463	1790.5	0.068	4.721	1804.0	335.67	II	C=O str
1788.4	0.104	1.493							
			1783.1	0.010	3.236	1781.4	279.07	IV	C=O str
1779.2	0.019	0.526							
			1776.8	0.307	2.425				
1775.8	0.523	1.255	1773.1	0.332	2.727	1775.9	295.48	I	C=O str
1774.3	0.398	1.584							
1771.9	0.153	2.760							
1770.0	0.135	2.535							
			1765.9	0.005	1.154				
1762.0	0.007	17.525	1761.8	0.012	4.603				
1752.4	0.063	161.51	1752.0	0.014	8.943				

Experimental						Calculation			
Argon			Parahydrogen			B3LYP/aug-cc-pVTZ		Conf.	Assignment[a]
ν_{Ar}	h_{Ar}	w_{Ar}	ν_{pH2}	h_{pH2}	w_{pH2}	ν_{B3LYP}[b]	I_{B3LYP}		
1741.1	0.016	4.462	1743.7	0.015	6.056				
1717.8	0.010	2.602	1720.6	0.006	1.747				
			1703.2	0.003	1.839				
1572.0	0.015	6.246	1576.1	0.010	9.131	1644.9	23.27	I	NH_2 scissor
1552.8	0.010	3.279	1557.0	0.007	4.684	1632.5	33.23	II	NH_2 scissor
			1552.0	0.001	3.622	1625.1	36.54	V	NH_2 scissor
			1541.7	0.002	6.752	1613.2	61.42	IV	NH_2 scissor
			1525.6	0.002	10.659				
			1513	0.001	7.639				
			1500.6	0.003	8.994	1480.6	10.18	IV	CH_3 bend asym
1461.6	0.047	3.813	1462.7	0.045	1.640	1477.6	6.96	I	CH_3 bend asym
1455.4	0.030	3.145	1457.5	0.020	2.114	1472.6	7.30		CH_3 bend asym
1387.8	0.032	5.389	1388.7	0.047	2.335	1390.3	76.17	II	CH_3 bend sym
1377.6	0.209	0.965	1379.0	0.163	0.863	1380.0	278.79	II	OH bend
1369.2	0.136	1.245	1370.7	0.189	1.819				
			1368.9	0.022	2.055				
1353.8	0.005	1.421	1359.9	0.004	5.574	1379.8	0.51	I	CH_3 bend sym, $C_\alpha H$ bend
1351.4	0.006	1.330	1351.0	0.004	8.133				
1337.6	0.013	2.889	1342.1	0.021	3.928	1333.2	16.93	I	$C_\alpha H$ bend, NH_2 twist, OH bend
1326.4	0.006	3.094	1332.6	0.011	4.210	1339.7	37.83	II	$C_\alpha H$ bend, OH bend
1317.0	0.003	0.940	1316.7	0.009	4.030	1312.9	10.03	II	$C_\alpha H$ bend, NH_2
			1311.7	0.008	5.432	1294.8	11.98	IV	$C_\alpha H$ bend, OH bend
1306.9	0.006	2.508	1304.2	0.005	10.253				
1267.2	0.004	1.372	1267.4	0.008	2.677	1274.5	2.77	I	$C_\alpha H$ bend,OH bend
1255.8	0.005	5.354	1259.4	0.006	11.646	1254.7	1.18	I	CH_3 rock, NH_2 twist, OH bend
1240.2	0.003	1.662	1242.5	0.004	12.050	1250.4	4.02	II	NH_2 twist, CH_3 rock, $C_\alpha H$ bend
1208.7	0.003	4.305	1210.6	0.005	10.534				
			1196.8	0.011	5.698	1214.1	24.36	IV	NH_2 twist, OH bend
1192.0	0.022	1.965	1190.9	0.001	3.206				
1189.8	0.019	3.145	1183.7	0.009	3.156	1183.0	19.62	II	C-O str, OH bend, NH_2 twist
1182.3	0.015	0.899							
1179.6	0.004	1.351							
			1158.0	0.009	4.535	1152.8	2.34	IV	CN str
1154.4	0.018	7.097	1154.4	0.026	2.937	1147.4	17.27	I	CN str

Experimental						Calculation			
Argon			Parahydrogen			B3LYP/aug-cc-pVTZ		Conf.	Assignment[a]
ν_{Ar}	h_{Ar}	w_{Ar}	ν_{pH2}	h_{pH2}	w_{pH2}	ν_{B3LYP}[b]	I_{B3LYP}		
1143.4	0.015	7.416	1144.5	0.007	2.406				
			1142.6	0.003	3.445	1143.3	75.75	V	CN str
			1127.6	0.018	10.003	1119.1	281.01	IV	C-O str
			1123.5	0.006	1.969	1117.7	228.38	V	C-O str
1122.7	0.020	0.060							
1118.8	0.038	8.962				1110.4	13.24	II	CN str
1112.1	0.698	1.831	1112.2	0.266	2.122	1106.1	286.03	I	C-O str
1110.0	0.122	1.289							
1106.6	0.157	1.477							
			1102.8	0.010	2.187				
1100.6	0.046	3.865	1095.4	0.006	6.423				
			1085.8	0.004	6.000				
			1077.6	0.003	9.107	1073.8	20.44	V	$C_\alpha C_\beta$ str
1065.3	0.106	1.594	1064.9	0.201	1.066	1068.2	24.02	I	CH_3 rock
1062.9	0.117	1.235							
1039.0	0.009	2.425	1040.7	0.007	8.071	1040.6	32.00	II	$C_\alpha H$ bend, CH_3 rock
1036.5	0.006	1.480							
			1028.2	0.004	1.939	1016.5	6.00	IV	$C_\alpha C_\beta$ str
1003.4	0.006	0.576	1003.4	0.003	2.357	997.6	0.98	II	NH_2 twist, CH_3 rock
1002.1	0.005	0.596							
			957.8	0.002	5.955				
926.3	0.027	0.519	927.7	0.031	1.210	923.4	37.55	II	$C_\alpha C_\beta$ str
923.1	0.016	8.745	920.7	0.009	2.211	908.0	1.09	I	$C_\alpha C_\beta$ str
			857.6	0.046	1.659				
853.3	0.566	0.939	855.7	0.407	2.057	870.5	133.74	I	NH_2 wag
852.2	0.135	4.791							
849.2	0.019	0.692							
827.2	0.030	7.128	828.4	0.023	3.115	850.9	73.73	II	OH bend, NH_2 wag
			815.6	0.003	2.524	838.7	54.24	V	NH_2 wag
805.5	0.048	2.522	806.4	0.024	3.584	827.3	73.06	II	OH bend, NH_2 wag
			803.9	0.005	0.776	823.2	134.60	IV	NH_2 wag
787.2	0.010	0.316	787.3	0.029	2.278	786.1	9.73	II	CC_α str
783.0	0.287	0.860	783.3	0.220	1.137	774.9	35.24	I	CC_α str
781.3	0.247	0.538							
780.5	0.054	0.687							
779.7	0.090	0.673							

Experimental						Calculation			
Argon			Parahydrogen			B3LYP/aug-cc-pVTZ		Conf.	Assignment[a]
ν_{Ar}	h_{Ar}	w_{Ar}	ν_{pH2}	h_{pH2}	w_{pH2}	ν_{B3LYP}[b]	I_{B3LYP}		
			778.2	0.003	0.652	779.3	48.98	IV	CC_α str
759.5	0.019	1.209	768.2	0.005	1.247				
			742.1	0.050	1.411				
741.9	0.043	0.885	740.7	0.093	1.188	744.9	29.79	I	COO wag
736.5	0.038	2.041	734.9	0.017	1.741	730.4	15.51	II	COO wag
729.2	0.020	0.396							

[a] asy - asymmetric, bend - bending, rock - rocking, scissor - scissoring, str - stretching, s - symmetric, twist - twisting, wag - wagging, C_α - α carbon, C_β - β carbon. [b] Vibrational modes with wavenumbers above 2000 cm^{-1} are scaled by a factor of 0.955, and all other vibrational modes are scaled by a factor of 0.985.

thus should be less abundant in our matrices, and the corresponding band has a calculated wavenumber of 1804.0 cm^{-1}. In the solid parahydrogen spectrum (Figure 5.5b), a strong band is observed at 1773.1 cm^{-1} and a weaker band is observed at 1790.5 cm^{-1}. These bands were assigned to conformer I and conformer II, respectively. A band associated with conformer IV was also detected in this region of the spectrum as a small shouldering band located at 1783.1 cm^{-1}. This assignment agrees well with the theoretical spectra as the band was derived to occur at 1781.4 cm^{-1}. The band corresponding to conformer V was unobserved in this region and was concluded to be masked by the conformer IV band since the conformer V band was calculated to occur at 1785.7 cm^{-1}, which is in close proximity of the conformer IV band. A relatively intense band at 1776.8 cm^{-1} remains unassigned after the allocation of the bands corresponding to conformers I, II, IV and V in this region of the spectrum. The identity of this band cannot be deduced based on the theoretical calculations employed as the position and relative intensity of this band does not agree with any of the bands in the predicted spectra. In the argon spectrum (Figure 5.5c), multiple bands were found in this region, and the amount of bands observed in this region of the spectrum greatly exceeds the amount of conformers which are expected to be present in the matrix. Upon annealing (Figure 5.5d), the number of bands detected reduced significantly, indicating that most of these bands are a result of site splitting. Using similar methods employed for the assignment of the solid parahydrogen spectrum, the band associated with conformer I was located at 1775.8 cm^{-1}, while the band corresponding to conformer II was found at 1793.3 cm^{-1}. In the region where the conformer IV band in the solid parahydrogen spectrum was located, a small band at 1779.2 cm^{-1} is found in the argon spectrum. Nevertheless, this band cannot be attributed to conformer IV or V. According to the theoretical spectra, the ν(C=O) and the ν(C-O) modes of these two conformers are derived to occur with similar intensities. Hence, if the ν(C=O) mode is detected, then the ν(C-O) mode should also be detected. In the ν(C-O) region of the argon spectrum, only one band at 1122.7 cm^{-1} that is not associated with other conformers was detected in the range of the calculated wavenumber of the ν(C-O) vibrational motion of conformer IV and V (Figure 5.6c). However, the origin of this band was concluded to differ from the band observed at 1779.2 cm^{-1} as the band at 1779.2 cm^{-1}

vanished upon annealing (Figure 5.5d), while the band at 1122.7 cm^{-1} remained (Figure 5.6d). Thus, the band at 1779.2 cm^{-1} cannot be assigned to either conformer IV and/or V as the corresponding ν(C-O) band is undetected, and there is a lack of evidence for the presence of conformer IV and V in this region of the argon spectrum.

Region of the ν(C-O) Vibrational Mode (1000 - 1400 cm^{-1})

The most apparent band in this region of the solid parahydrogen spectrum at 1112.2 cm^{-1} (Figure 5.6b) was assigned to the ν(C-O) vibrational mode of conformer I. In the argon spectrum (Figure 5.6c), this conformer I band is located at 1112.1 cm^{-1}, with a shouldering band at 1110.0 cm^{-1} as a result of site splitting. As per our theoretical calculations, there is an absence of peaks which correspond to the ν(C-O) vibrational motion of conformer II in our experimental spectra. Moreover, bands associated with conformer IV and V are predicted to be slightly redshifted with respect to that of conformer I at 1119.1 and 1117.7 cm^{-1}, respectively (Figure 5.6a). Two small bands shouldering that of conformer I is observed at 1123.5 cm^{-1} and 1127.6 cm^{-1} in our solid parahydrogen spectrum, and these bands were concluded to originate from conformer V and IV, respectively. In the solid argon spectrum, small shouldering bands at 1118.8 cm^{-1} and 1122.7 cm^{-1} are also observed at the higher wavenumber side of the conformer I band. The peak at 1118.8 cm^{-1} was attributed to another vibrational mode of conformer II (ν(CN)) which is derived to occur in this region. The band at 1122.7 cm^{-1} cannot be assigned to conformer IV or V. As discussed in the section concerning the ν(C=O) region of the spectra, the ν(C-O) bands and the ν(C=O) bands of conformers IV or V were calculated to occur with comparable intensities. Consequently, if the ν(C-O) band is observed, the ν(C=O) band is also expected to be detected and vice-versa. However, this was unobserved in our solid argon spectrum. Furthermore, if the band at 1122.7 cm^{-1} was allocated to conformer IV or V, the intensity of the peak would indicate that other vibrational modes of conformer IV or V should also be detected in the ν(OH) and the $\omega(NH_2)$ regions of the spectra. Yet, these bands were unobserved in an argon matrix environment. As a result, the band at 1122.7 cm^{-1} was not attributed to either conformer IV or conformer V, and the origin of this peak cannot be deduced based on the theoretical spectra.

Region of the $\omega(NH_2)$ Vibrational Mode (800 - 880 cm^{-1})

In this region of the spectra, a strong peak associated with conformer I is calculated to occur in a higher wavenumber range at 870.5 cm^{-1} (Figure 5.6a). This band was allocated at 855.7 cm^{-1} in a solid parahydrogen environment (Figure 5.6b), and at 853.3 cm^{-1} in a solid argon environment (Figure 5.6c). At a lower wavenumber region of the conformer I peak, two smaller peaks with similar intensities are observed in both the solid parahydrogen and the solid argon spectrum, which are at 806.4 cm^{-1} and 828.4 cm^{-1} in the parahydrogen spectrum, and at 805.5 cm^{-1} and 827.2 cm^{-1} in the argon spectrum. These were assigned to conformer II as two bands associated with this conformer were derived to occur with comparable intensities and blue-shifted from the conformer I band. Additional bands at 803.9 cm^{-1} and at 815.6 cm^{-1} were observed in this region of our solid parahydrogen spectrum but not in our solid argon spectrum. A comparison between the theoretical spectra and the solid parahydrogen spectra reveals that the band at 803.9 cm^{-1} belongs to conformer IV and the band at 815.6 cm^{-1} belongs to conformer V. Consequently, the absent of

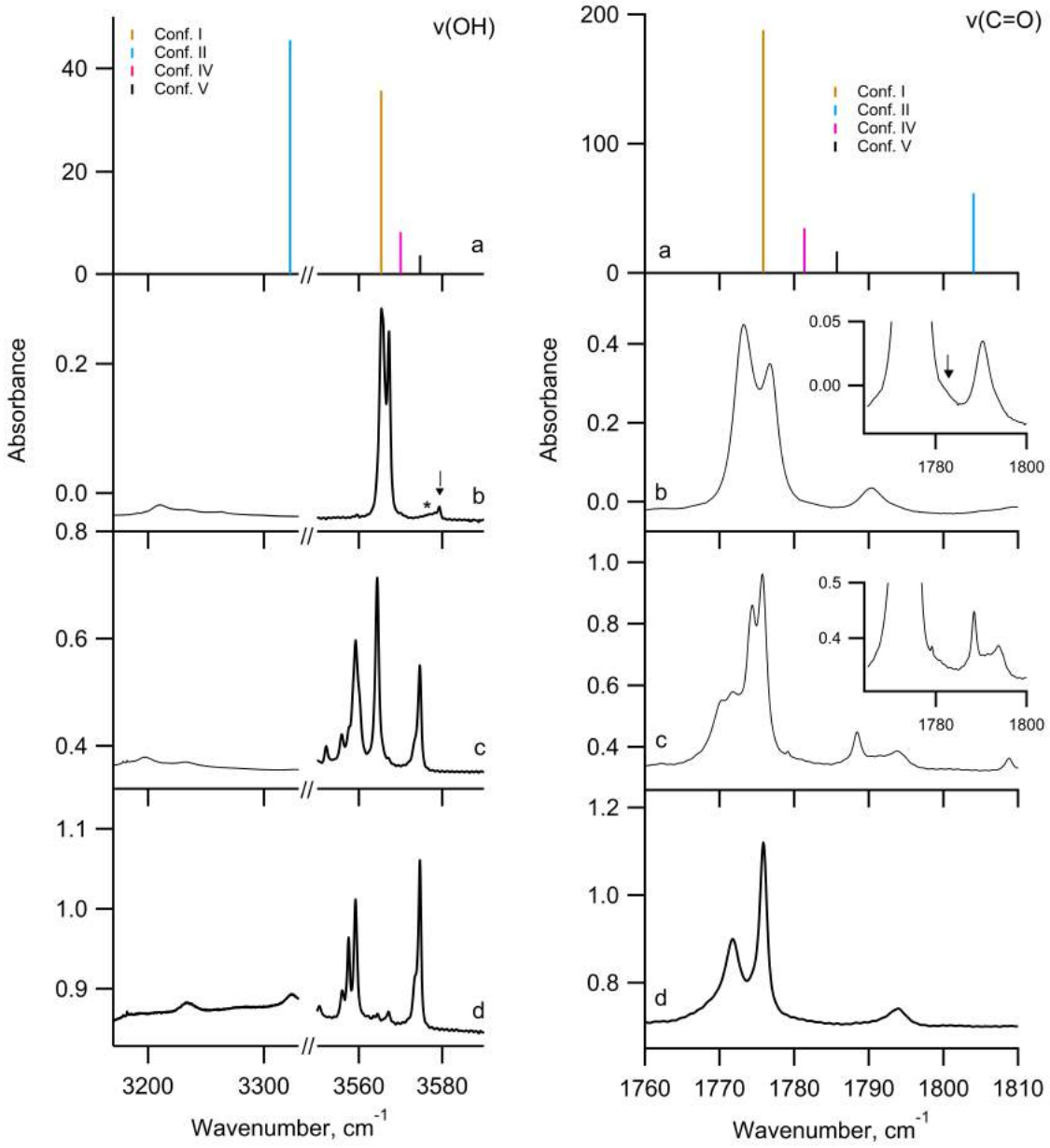

Figure 5.5: The ν(OH) and ν(C=O) regions of the vibrational spectra of α-alanine sublimed at 420 K. Panel (a) is the theoretical spectra of the observed conformers derived by B3LYP/aug − cc − pVTZ. The theoretical wavenumbers are corrected by a factor of 0.955 for the ν(OH) region and 0.985 for the ν(C=O) region, and the relative intensities are scaled with respect to the Boltzmann distribution at 420 K assuming that only conformers I, II, IV and V are present. Panel (b) shows the FTIR spectra of α-alanine isolated in a parahydrogen matrix (T_{dep} = 4 K) obtained immediately after deposition. Panel (c) is the argon matrix isolation FTIR spectra (T_{dep} = 18 K) recorded immediately after deposition, while panel (d) is the corresponding spectra registered after annealing (10 mins, 40 K). The "*" and "↓" donates the conformer IV and V bands, respectively, which are present in the parahydrogen spectra, but absent in the argon spectra.

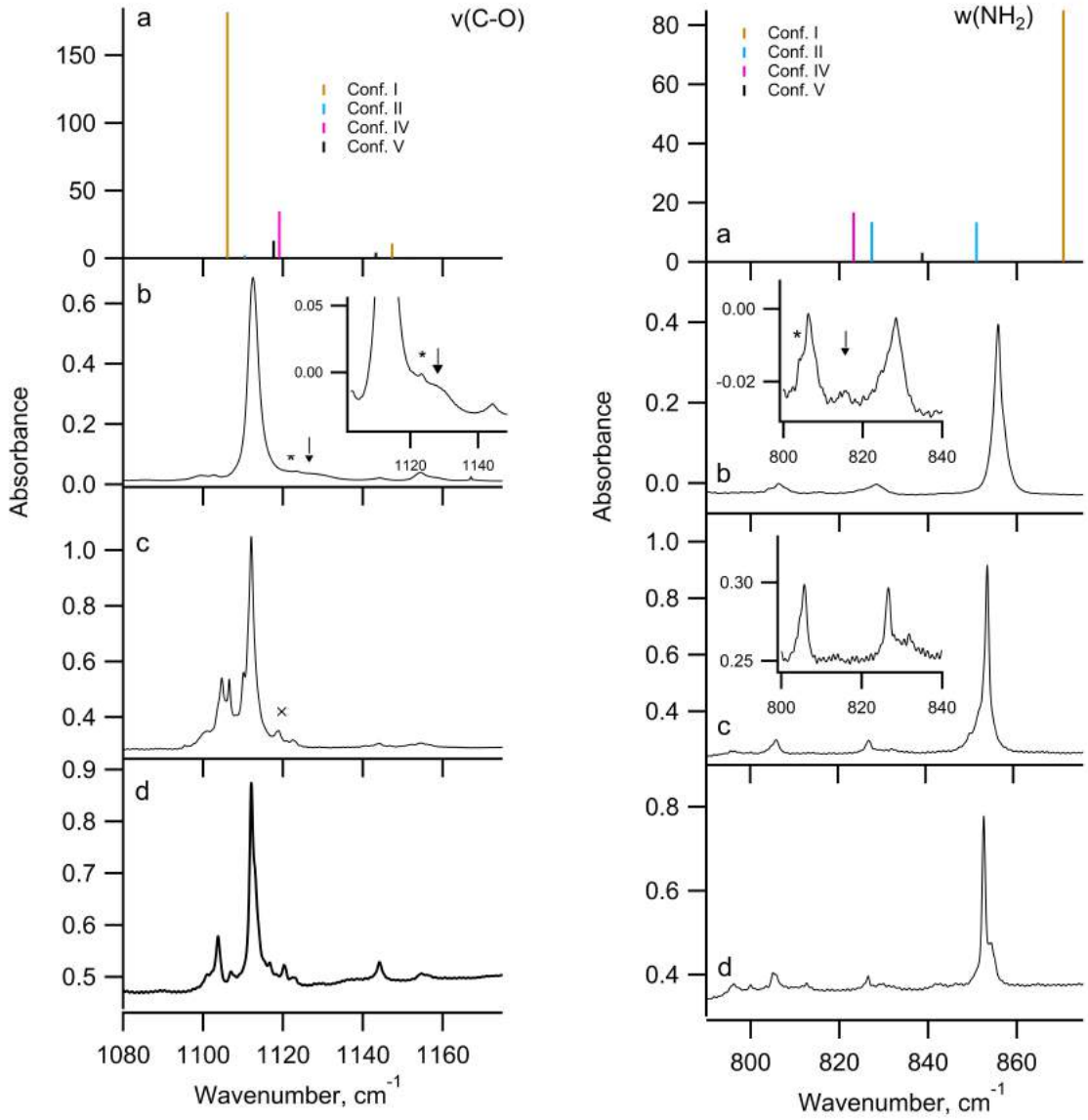

Figure 5.6: The ν(C-O) and $\omega(NH_2)$ regions of the vibrational spectra of α-alanine sublimed at 420 K. Panel (a) is the theoretical spectra of the observed conformers derived by $B3LYP/aug-cc-pVTZ$. The theoretical wavenumbers are corrected by a factor of 0.985 for both ν(C-O) and $\omega(NH_2)$ regions, and the relative intensities are scaled with respect to the Boltzmann distribution at 420 K assuming that only conformers I, II, IV and V are present. Panel (b) shows the FTIR spectra of α-alanine isolated in a parahydrogen matrix (T_{dep} = 4 K) obtained immediately after deposition. Panel (c) is the argon matrix isolation FTIR spectra (T_{dep} = 18 K) recorded immediately after deposition, while panel (d) is the corresponding spectra registered after annealing (10 mins, 40 K). The "*" and "↓" donates the conformer IV and V bands, respectively, which are present in the parahydrogen spectra, but absent in the argon spectra. The band marked by "×" corresponds to the ν(CN) mode of conformer II present in the ν(C-O) region of the argon spectrum.

these bands in the argon spectrum suggests a lack of conformer IV and V in our argon matrix.

From our solid parahydrogen matrix isolation spectra, we were able to observe and identify the presence of four gas phase α-alanine conformers, conformer I, II, IV and V. Conformer I is stabilized by a cis COOH structure [69] and two N-H—O=C hydrogen bonds. It is the lowest energy conformer, and as a result, has the greatest abundance in our matrix and is responsible for some of the most intense bands. Out of the twenty-four bands calculated to occur in the region of our recorded spectra, all but two were observed experimentally. Conformer II is the third lowest energy conformation and the only trans COOH structure which is detected in our solid parahydrogen matrix. A total of twenty-one bands (out of twenty-five) associated with this conformation were identified in our spectrum. Similar to conformer I, conformer IV is also stabilized by a NH—O=C interaction; however, conformer IV consists of only one hydrogen bond. As a result, it is the fourth most stable conformation, and only fourteen bands were assigned. The highest energy conformation that is detected in our solid parahydrogen matrix is conformer V. Due to its low abundance in the matrix, the corresponding bands were weak in intensity and only seven bands were identified experimentally.

As compared to solid parahydrogen, the argon spectra were more complex due to site splitting, consequently, spectral analysis was more difficult. Furthermore, the argon matrix also consists of less gaseous α-alanine conformers - only conformer I and II were detected, with twenty-two bands attributed to each conformer, respectively. The absence of conformer IV and V in crystalline argon can be attributed to the large mass of argon and a low energy barrier between conformational states. Subsequently, the collision between argon atoms and α-alanine molecules results in a conversion from higher energy states (IV and V) to lower energy states (I and II). On the other hand, parahydrogen atoms are lighter in mass and thus provides a softer collision between the matrix atoms and α-alanine molecules. As a result, the solid parahydrogen matrix was able to preserve a more complete set of gas phase α-alanine conformers.

Contrary to literature [80], we were unable to find evidence to support the presence of conformer III in a solid parahydrogen or a solid argon environment. The most predominant band that was observed for this conformer was reported to occur at 838 cm^{-1}. However, we did not detect this band in the $\omega(NH_2)$ region of solid parahydrogen and solid argon spectra, or any of the bands which corresponds to the ν(OH), ν(C-O) or ν(C=O) vibrational modes of conformer III. The absence of this conformer is most like due to low energy barrier heights, which results in fast relaxation to lower energy states. This explanation is supported by a previous conformational study of α-alanine performed by Balabin using jet-cooled Raman spectroscopy, where conformer III was observed to result in lower energy conformers (I or II) via collision as indicated by the decrease in intensity of the conformer III bands as nozzle-laser distance was increased [78].

5.2.3 Populations of Gaseous α-alanine Conformers in Solid Parahydrogen and in Solid Argon at Various Sublimation Temperatures

The effects of sublimation temperature on the population of α-alanine conformers in a crystalline parahydrogen environment was compared with that of a solid argon environment. Three different sublimation temperatures, 410 K, 420 K, and 430 K, were employed and the corresponding spectra can be found in figures B.4, B.5,B.1, B.2, B.6 and B.7 of Appendix, respectively. The conformational population at each temperature (Table 5.5) were extracted from the experimental areas of peaks that are derived to be predom-

inant.

Table 5.5: Experimental (Exp., %) and theoretical relative populations (Boltzmann, %) of the gaseous α-alanine conformers detected in parahydrogen matrices (Para-H_2) and argon matrices (Ar) at sublimation temperatures of 410 K, 420 K, and 430 K.

	430 K			**420 K**			**410 K**		
	Exp.		Boltz-	Exp.		Boltz-	Exp		Boltz-
	Para-H_2[a]	Ar[a]	mann	Para-H_2[a]	Ar[a]	mann	Para-H_2[a]	Ar[a]	mann
Conformer I	67.2 %	79.5 %	63.1 %	73.4 %	79.8 %	63.6 %	75.0 %	79.0 %	64.1 %
Conformer II	24.6 %	20.5 %	18.3 %	21.5 %	20.7%	18.4 %	21.2 %	21.0 %	18.4 %
Conformer IV[b]	3.0 %	0.0 %	12.7 %	2.7 %	0.0 %	12.4 %	2.4 %	0.0 %	12.0 %
Conformer V[b]	5.2 %	0.0 %	5.9 %	2.4 %	0.0 %	5.7 %	1.4 %	0.0 %	5.4 %

[a] Experimental relative populations of conformer I, II, IV, and V were derived from the band corresponding to the ν(C=O), ν(C=O), $\delta(NH_2)$ and $\omega(NH_2)$, respectively. [b] Conformer IV and V were undetected in argon matrices.

In both matrices, the same set of conformers were observed in the spectra obtained at sublimation temperatures of 410 K and 430 K as compared to the spectra recorded using a sublimation temperature of 420 K. In contrast with the results obtained in crystalline argon, the population of each conformer taken from the solid parahydrogen spectra is in better agreement with the corresponding Boltzmann distribution (Table 5.5). This is attributed to the superior ability of solid parahydrogen to preserve a more complete set of conformers. Furthermore, in the solid parahydrogen spectra, a sublimation temperature induced excitation between conformational states as predicted by the Boltzmann distribution was detected - the lowest energy configuration, conformer I, decreased in abundance while the higher energy configurations, conformer II and V, increased in abundance as the sublimation temperature was raised (Figure 5.7). The population of conformer IV was approximately constant as a function of sublimation temperature, which suggests that the energy barrier of this conformer is comparatively larger. On the other hand, a lack of any excitation was observed in the argon spectrum (Figure 5.7). The population of conformers in an argon matrix remained relatively fixed as the sublimation temperature was varied. A change of less than 1 % was observed for each conformer, which is too small to be concluded as a result of the variation in sublimation temperature. This lack of excitation is once again due to the large mass of argon atoms, which facilitates collisional relaxation. Subsequently, any higher energy states which were obtained due to an increase of sublimation temperatures were lost in an argon matrix.

5.2.4 UV-irradiation of α-alanine in Solid Parahydrogen and in Solid Argon

The effects of *in-situ* UV-irradiation on α-alanine were investigated in crystalline parahydrogen and crystalline argon. The sample was irradiated for 4 hours in total, and a spectrum was taken at each hour of irradiation. For the spectra obtained in solid parahydrogen, please see Figures B.8 - B.12 of Appendix, and for the spectra recorded in solid argon, please see Figures B.13 - B.17 of Appendix. For both matrices, *in-situ* UV-irradiation resulted in photodissociation of α-alanine, as indicated by a decrease in all conformers and an increase in CO_2, instead of excitation to higher energy configurations. Thus, the same sets of conformers were observed after irradiation as compared to immediately after deposition. Furthermore, ir-

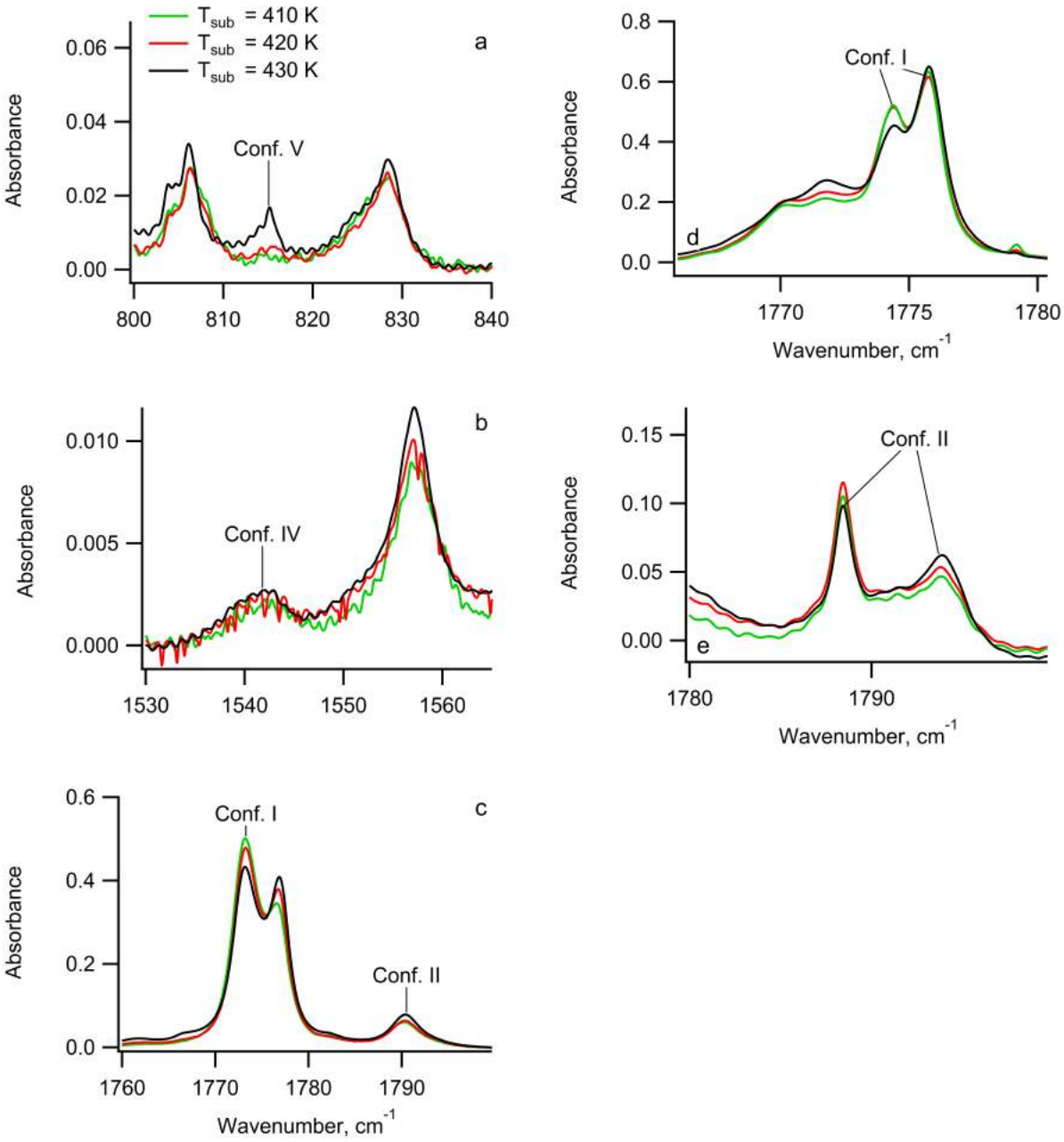

Figure 5.7: Regions of the FTIR spectra of α-alanine prepared using different sublimation temperatures (410 K, 420 K, and 430 K) that were employed for conformational population calculations (Table 5.5). Panels (a) - (c) give the spectra obtained in parahydrogen matrices, while panels (d) and (e) consist of the spectra recorded in argon matrices. The intensities of the bands in the spectra acquired at sublimation temperatures of 410 K and 430 K are weighted by the sample concentration at 420 K.

radiation was more influential in solid parahydrogen. In the parahydrogen matrix, conformer I bands were found to decrease at a faster rate as compared to the corresponding bands in the argon matrix (Table 5.6 and Figure 5.8). Upon 4 hour of irradiation, a 35.3 % decrease was observed for conformer I in a solid parahydrogen environment, while an 8.3 % decrease was found in a solid argon environment. The more prominent effects observed in the parahydrogen matrix is due to the quantum nature of hydrogen crystals, which allows the corresponding matrices to provide a softer environment for the analytes as compared to noble gas matrices (see Section 2.1.2). Consequently, the effects of *in-situ* photoirradiation are more pronounced in solid parahydrogen than in solid argon.

Table 5.6: The percent decrease (%) in the intensity of conformer I observed in parahydrogen and argon matrices upon 1 hr, 2 hrs, 3 hrs, and 4 hrs of UV-irradiation as compared to deposition intensity.

UV irradiation	1 hr	2 hrs	3 hrs	4 hrs
Parahydrogen	9.6 %	18.9 %	31.0 %	35.3 %
Argon	1.9 %	4.2 %	6.5 %	8.3 %

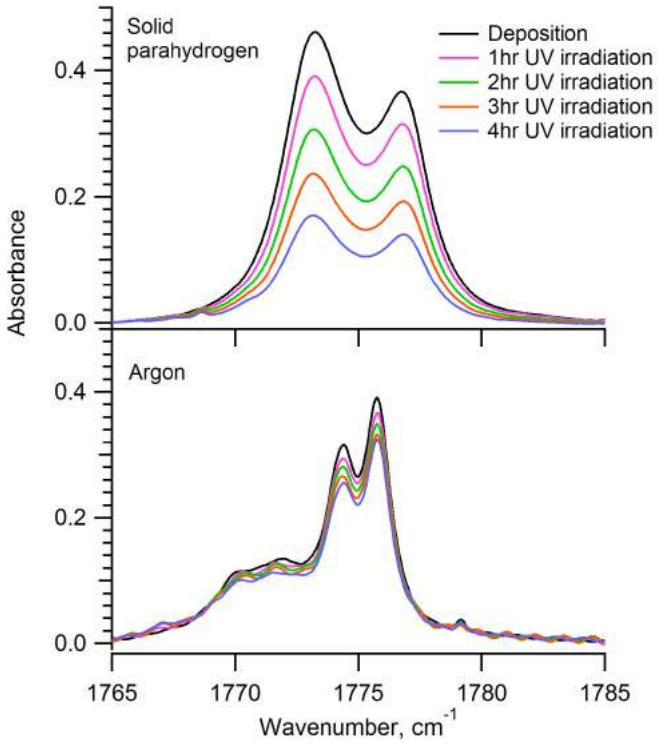

Figure 5.8: FTIR spectra of the ν(C=O) band of α-alanine conformer I recorded in solid parahydrogen matrices and argon matrices immediately after deposition, and after 1 hr, 2 hrs, 3 hrs, and 4 hrs of *in-situ* UV-irradiation.

Upon prolonged UV-irradiation, we also noticed the formations of weak photoproducts band in our spectra. Therefore, we decided to expand our investigation on the UV photolysis of α-alanine with the

deuterated analogue of the amino acid (see Section 5.3).

5.3 UV Photolysis of Deuterated α-alanine in Solid Parahydrogen

As mentioned in the Introduction (see Chapter 1), the effect of UV radiation on amino acids is one of the keys for their search in interstellar space, where strong UV radiation exist. In our experiment, we have investigated the UV photochemistry of both β- and α-alanine encaged in parahydrogen and argon matrices. In solid parahydrogen, β-alanine mainly exhibited conformational change upon UV-irradiation with minimal photodissociation outcomes; α-alanine, on the other hand, experienced photodecomposition almost completely. Aside from the decay of α-alanine sample and the production of CO_2, we observed the formation of several new, but weak, photoproducts bands in our parahydrogen spectra upon prolonged UV-irradiation. In order to better assess these photoproducts peaks, we have reinvestigated the photolysis of α-alanine in parahydrogen matrices by using the deuterated form of α-alanine (Figure 5.9). We also hope to clarify the role played by the parahydrogen environment on the UV photochemistry of α-alanine by employing the deuterated α-alanine sample in our experiment.

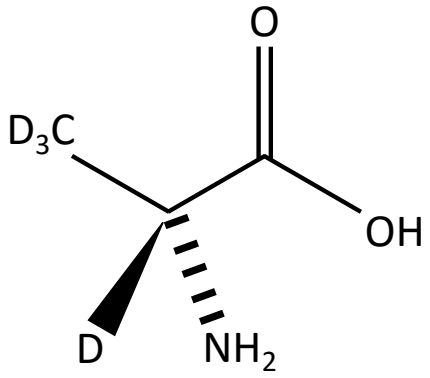

Figure 5.9: Structure of deuterated α-alanine: DL-Alanine2,3,3,3-d.

5.3.1 Experimental and Computational Details for Deuterated α-alanine UV Photochemistry Study

The experimental procedures for this study were similar to that of α-alanine conformational study as described previously (see Section 5.2.1), with some slight variations. Parahydrogen gas was predominantly used as the matrix material for this experiment. We acquired longer deposition durations of 2.5 hrs for the deuterated α-alanine sample (DL-Alanine-2,3,3,3-d4, Sigma Aldrich, 98 atom % D isotopic purity, used as received), with a gas flow rate of 5 ccm. The sublimation temperature of deuterated α-alanine was 380 K, and the mixed amino acid and matrix gas sample was grown directly onto the 4 K BaF_2 cold window. The sample matrix was subjected to *in-situ* UV-irradiation with a modified deuterium lamp, and a total of 3 hrs of irradiation was applied to the deposited sample. In terms of spectra measurements, all FTIR spectra collected in this experiment were recorded at 0.05 cm^{-1} resolution and 1000 number of measurements, with the aim of obtaining stronger photoproducts signals induced by the increase in signal-to-noise ratio.

On the computation aspect, we performed calculations at B3LYP/aug − cc − pVTZ level of theory on the twelve stable α-alanine conformers, as denoted by Cs*ászá*r's nomenclatures [69] and Balabin's geometric configurations [78], in their deuterated forms (Figure 5.10, and Table C.1 of Appendix). We have also applied the same theoretical calculation parameters on seventeen photoproduct candidates we predicted to result from the UV photolysis of deuterated α-alanine (Table C.3 of Appendix).

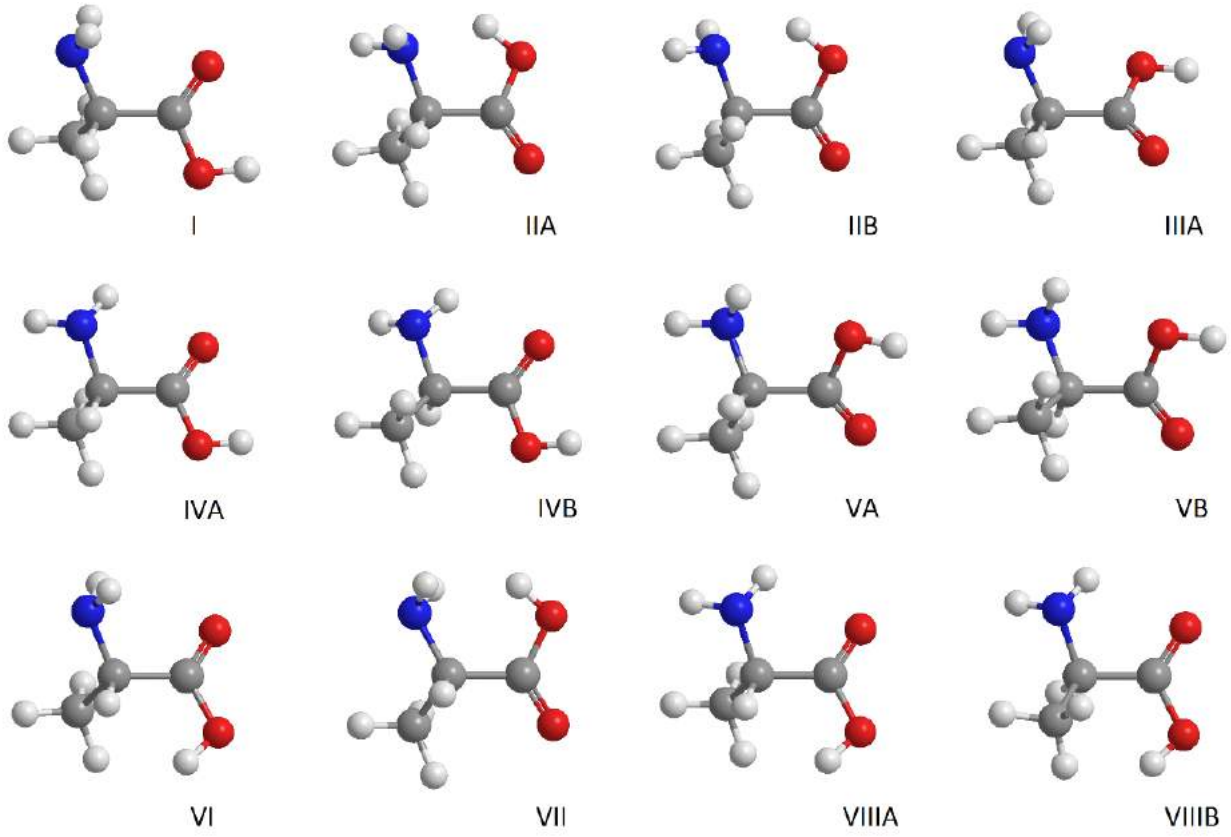

Figure 5.10: Structures of the twelve lowest energy deuterated α-alanine conformers using by Cs*ászá*r's nomenclatures and Balabin's geometric configurations. The labels "A" and "B" denoted the L- and D- enantiomers, respectively.

5.3.2 Spectra Comparison between α-alanine and Deuterated α-alanine

Before we proceed with analyzing the UV photoproducts, we did a quick spectra comparison between α-alanine and deuterated α-alanine. As the corresponding ZPE-corrected relative energies and the relative Gibbs free energies of the calculated deuterated α-alanine conformers (Table 5.7) are close in values to those of α-alanine (Table 5.3), we could assume that the same four conformers observed in the α-alanine experiment should also be obtained in the deuterated α-alanine experiment. Due to the present of deuteration on the carbon backbone (C_α) and the extension carbon (C_β), the deuterated α-alanine spectra experienced an overall downshift in wavenumbers as compared to the α-alanine spectra (Figure 5.11), by 15 - 30 cm^{-1} for most regions and up to 700 - 800 cm^{-1} for the CH_3 symmetric and asymmetric stretch regions. The only two

regions that seemed to be unaffected by the deuteration effect were the ν(OH) and ν(C=O) regions, which remained relatively at the same wavenumber positions as that in α-alanine spectra. The deuterated α-alanine spectra also featured two strong bands which were previously unobserved or weak in the α-alanine spectra. These two bands were the peaks at 1144.9 cm^{-1} and 920.7 cm^{-1}, which were attributed to conformer I with the $C_\alpha H$ bending and NH^2 twisting vibrational modes. The peak at 1144.9 cm^{-1} also had vibrational contribution from the OH bending mode. Table 5.8 summarized the spectral assignments of deuterated α-alanine as deposited in parahydrogen matrices, in the approximate regions of ν(OH), $\nu(C^3H)$, ν(C=O), ν(C-O), and $\omega(NH_2)$. The identities of deuterated α-alanine spectral signals were determined by comparing the resulting spectra to the assignment conclusions from the α-alanine conformational experiment (see Table 5.4 for the complete assignments of α-alanine) and to the computed vibrational frequencies values of deuterated α-alanine at B3LYP/aug − cc − pVTZ level of theory.

Table 5.7: ZPE-corrected relative energies, ΔE, and relative Gibbs free energies at 380 K, ΔG_{380K}, of the twelve lowest energy deuterated α-alanine conformers calculated by B3LYP/aug − cc − pVTZ.

Conformer	**I**	**IIA**	**IIB**	**IIIA**	**IVA**	**IVB**	**VA**	**VB**	**VI**	**VII**	**VIIIA**	**VIIIB**
ΔE, kJ mol^{-1}	0.00	1.80	1.80	4.89	4.83	5.40	8.17	9.34	20.34	21.18	24.72	25.38
ΔG_{380K}, kJ mol^{-1}	0.00	4.06	4.06	3.85	5.70	6.50	8.59	9.76	20.43	22.40	25.47	26.05

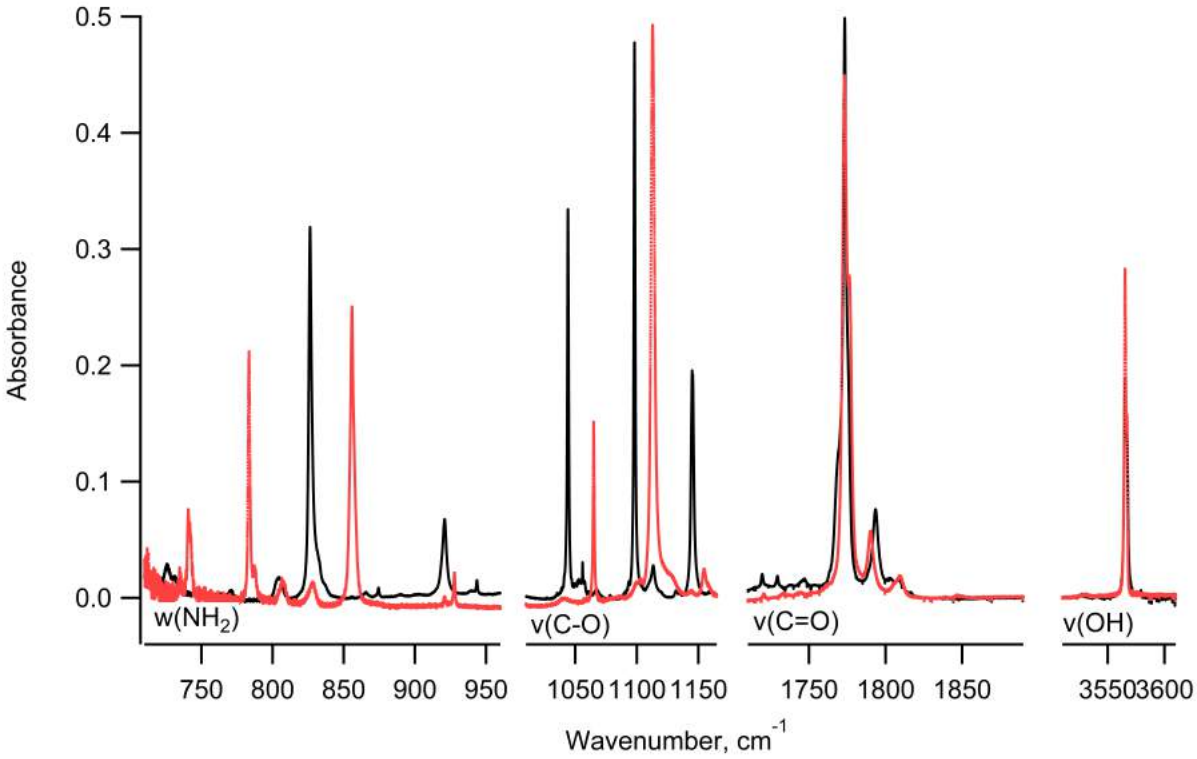

Figure 5.11: FTIR spectra of deuterated α-alanine (black trace) and non-deuterated α-alanine (red trace, scaled to match deuterated α-alanine signal intensities) in the regions of $\omega(NH_2)$, ν(C-O), ν(C=O), and ν(OH) in solid parahydrogen taken immediately after deposition.

Table 5.8: Experiment wavenumbers (ν, cm^{-1}) and peak height (h, arbitrary unit) of Deuterated α-alanine sublimed at 380 K trapped in solid parahydrogen in comparison with the experiment values of non-deuterated α-alanine as presented in Section 5.2. The corresponding theoretical wavenumbers (ν, cm^{-1}) and intensities (I, $km \cdot mol^{-1}$) were calculated by B3LYP/aug − cc − pVTZ.

Deuterated α-alanine				Non-Deuterated α-alanine				$\Delta\nu_{expt}$[b]	Conf.	Assignment[c]
Experimental		Calculation[a]		Experimental		Calculation[a]				
$\nu_{d\text{-}\alpha\text{-}ala}$	$h_{d\text{-}\alpha\text{-}ala}$	ν_{B3LYP}	I_{B3LYP}	$\nu_{\alpha\text{-}ala}$	$h_{\alpha\text{-}ala}$	ν_{B3LYP}	I_{B3LYP}			
3579.2	0.006	3547.6	66.89	3579.3	0.017	3574.7	66.80	+ 0.1	V	OH str
3577.9	0.003	3552.3	67.25	3577.5	0.007	3570.0	67.20	- 0.4	IV	OH str
3565.4	0.187	3543.0	56.16	3565.3	0.224	3565.1	56.11	- 0.1	I	OH str
3212.5	0.015	3301.7	246.89	3210.0	0.015	3322.6	247.63	- 2.5	II	OH str
2252.9	0.007	2269.2	5.18	3003.2	0.049	2986.0	11.89	+ 750.3	I	CH_3 str asym
2234.4	0.023	2251.4	10.38	2982.9	0.078	2966.7	20.99	+ 748.5	I	CH_3 str asym
2230.8	0.006	2252.6	11.11	2964.4	0.001	2959.3	20.26	+ 733.6	IV	CH_3 str asym
2071.6	0.007	2137.7	7.05	2933.7	0.011	2901.8	11.25	+ 862.1	I	CH_3 str sym
2069.7	0.001	2134.6	8.27	2886.5	0.006	2897.2	11.37	+ 816.8	II	CH_3 str sym
1793.5	0.061	1793.6	337.01	1790.5	0.068	1804.0	335.67	- 3.0	II	C=O str
1775.4	0.012	1770.6	282.22	1783.1	0.010	1781.4	279.07	+ 7.7	IV	C=O str
1773.2	0.483	1765.3	299.38	1773.1	0.332	1775.9	295.48	- 0.1	I	C=O str
1375.5	0.053	1373.0	375.43	1379.0	0.163	1380.0	278.79	+ 4.0	II	OH bend
1158.5	0.003	1140.2	20.25	1183.7	0.009	1183.0	19.62	+ 25.2	II	C-O str, OH bend, NH_2 twist
1144.9	0.191	1131.9	87.60	---	---	---	---	---	I[d]	OH bend, $C_\alpha H$ bend, NH_2 twist
1113.1	0.020	1115.1	223.20	1127.6	0.018	1119.1	281.01	+ 14.5	IV	C-O str
1111.1	0.008	1112.1	277.51	1123.5	0.006	1117.1	228.38	+ 12.4	V	C-O str
1098.2	0.477	1089.8	98.97	1112.2	0.266	1106.1	286.03	+ 14.0	I	C-O str
1044.0	0.337	1041.4	110.26	1064.9	0.201	1068.2	24.02	+ 20.9	I	CH_3 rock
920.7	0.064	915.8	38.46	---	---	---	---	---	I[d]	NH_2 twist, $C_\alpha H$ bend
826.3	0.316	833.4	108.29	855.7	0.407	870.5	133.74	+ 29.4	I	NH_2 wag
805.4	0.017	824.4	77.23	828.4	0.023	850.9	73.06	+ 23.0	II	OH bend, NH_2 wag
771.2	0.006	804.1	139.85	803.9	0.005	823.2	134.60	+ 32.7	IV	NH_2 wag

[a] Scaling factor: 0.955 for vibrational modes with wavenumbers greater than 2000 cm^{-1}, 0.985 for all other vibrational modes. [b] The difference between the wavenumber of deuterated α-alanine and non-deuterated α-alanine at the same vibrational mode. "+" denotes a blue-shift on the peak position of α-alanine to the deuterated α-alanine, and "-" denotes a red-shift. [c] asy - asymmetric, bend - bending, rock - rocking, str - stretching, s - symmetric, twist - twisting, wag - wagging. [d] Assignment applicable to deuterated α-alanine spectra only.

5.3.3 Assignment Attempt on the UV Photoproducts of Deuterated α-alanine

Figure 5.12 highlighted the spectra results of deuterated α-alanine after 3 hrs of *in-situ* UV-irradiation in parahydrogen matrix. For the full spectra obtained for this investigation, please see Figures C.1 - C.3 of Appendix. From the spectra results, we observed the dominant production of CO_2 (at 2345 cm^{-1}) with the expense of the amino acid molecules upon prolonged UV-irradiation. We also noticed the formation of several new, but often small, bands across our spectra after the UV-irradiation (see Table C.2). We deduced that these bands must be resulting from the photodecarboxylation of the acid group from the deuterated α-alanine, which gave CO_2 and another major photoproduct with the amine group latched on it. We came out with seventeen possible photoproducts for this photolysis reaction (Table C.3 of Appendix).

One plausible outcome of amino acids UV photolysis is the production of hydrogen cyanide (HCN). In 2001, Ehrenfreund *et al.* reported the formation of HCN along with CO_2 from their photolysis studies of several amino acids, including α-alanine, in argon matrix [20]. The group stated that HCN was formed through rapid decay of R-CH_2-NH_2 (in which "R" is the specific amino acids side chain) into the intermediate methylimine (H_2C=NH), which then decompose to yield HCN. Their argument was supported by the detection of HCN predominant peak at 3300 cm^{-1} and two smaller peaks at 2100 cm^{-1} and 711 cm^{-1} in their spectra. The group also observed several weak peaks consistent with the wavenumbers of the intermediate H_2C=NH throughout their spectra [20]. Contrary to the findings of Ehrenfreund *et al.*, we were unable to find evidence to support the production of HCN, or its deuterated analogue DCN, after UV photolysis of deuterated α-alanine in solid parahydrogen environment. The predominant peak at 3300 cm^{-1} for HCN and 2600 cm^{-1} for DCN were undetected in our spectra. We also did not observe several theoretically intense signals of H_3C-CH_2-NH_2, H_2C=NH, and their deuterated analogoues in our spectra, impliying these intermediary molecules must have underwent a secondary or tertiary photochemical reaction to produce photoproducts that is other than HCN. However, as to what the final photoproducts might be is still unknown to us, and we are still in the process of concisely assessing the identities of the obtained photoproducts bands with the photoproduct candidates we calculated.

Another puzzle we encountered in our attempt to identify the photoproducts of deuterated α-alanine in solid parahydrogen was the observation of several photoproduct bands not associated with the amine group within our spectra. One of these bands was the medium intensity signal located at 1845 cm^{-1}. The position in which the photoproduct band of 1845 cm^{-1} was situated might be more relevance to the acid group than the amine group of amino acid. However, the dominant production of CO_2 upon UV photolysis of the amino acid sample ruled out any other form of photochemistry by-product that might arise from the acid group. We are now trying to find and assess other possible precursors, in which might be in the form of unwanted impurities, that led to the formation of non-amine photoproduct molecules in our parahydrogen matrix.

5.4 Study of Amino Acid Zwitterions in Solid Parahydrogen

We attempted to grow β-alanine zwitterions in parahydrogen matrices by doping the gas mixture with water prior to deposition. This method was previously applied by Ramaekers *et al.* on glycine in solid argon, and the group reported the requirement of at least three water molecules per glycine to transform the amino acid into its zwitterionic form [94]. The presume β-alanine zwitterion spectra were compared to the spectrum of

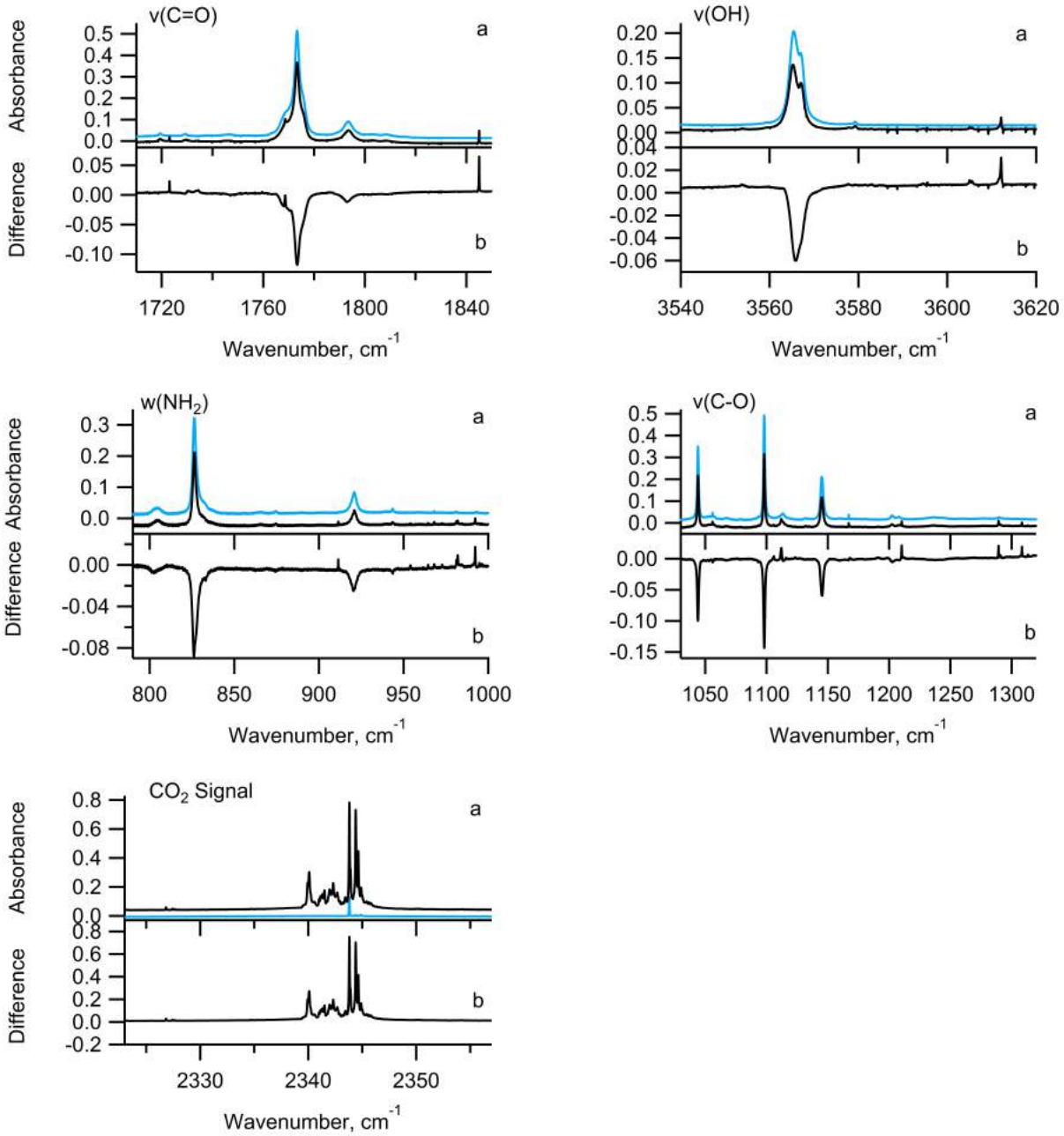

Figure 5.12: FTIR spectra of deuterated α-alanine in solid parahydrogen in the regions of ν(OH), ν(C=O), ν(C-O), and $\omega(NH_2)$ taken immediately after deposition (blue trace) and after 3 hrs of UV-irradiation (black trace). The FTIR spectra of CO_2 signal before and after UV irradiation is also shown. Each panel consists of (a) absorbance spectra of sample as deposited and after photolysis, and (b) a difference spectrum (the spectrum measured immediately after deposition subtracted from the spectrum recorded after 3 hrs of UV irradiation).

neutral β-alanine.

5.4.1 Experimental Details for β-alanine Zwitterion Study

The experimental procedures for this study were similar to that of neutral β-alanine (see Section 5.1.1), with the addition of one preparatory step. Water-doped parahydrogen was prepare prior to deposition by mixing the appropriate amount of water vapour into the parahydrogen gas storage vessels. Twice distilled water was used and the concentrations of water employed for our study were 100 ppm and 500 ppm. We then deposited the gaseous β-alanine sample (sublimated at 390 K) and H_2O/pH_2 mixture gas simultaneously onto the 4 K BaF_2 cold window at a flow rate of 5 ccm for 1.5 hrs. No UV-irradiation experiment was performed for this study. All the FTIR spectra for this experiment were registered at 0.2 cm^{-1} resolution with 1000 number of measurements.

5.4.2 Spectra Result of β-alanine Zwitterion in Solid Parahydrogen

Figure 5.13 showed the presume spectra of β-alanine zwitterion (*i.e.*, water-doped samples) in comparison with the spectra of neutral β-alanine. For the full spectra obtained for this investigation, please see Figures D.1 - D.3 of Appendix. All five conformers observed in the neutral β-alanine spectra were attained in the β-alanine zwitterion spectra as well, with the same wavenumber position and comparable intensity. Moreover, the presume β-alanine zwitterions spectra displayed the present of additional bands, specifically at the ν(OH) and ν(C=O) regions. These bands were observed to increase with the increase concentration of water-dopant, indicating them to be spectral signal of the produced β-alanine zwitterions formed via H_2O-assisted proton transfer in the amino acid. The newly formed bands at the 2800 cm^{-1} and 3500 cm^{-1} regions were consistent with the assignment of $^+NH_3$ stretch in literature [94]; whereas multiple new bands observed in the 1400 cm^{-1} and 1700 cm^{-1} regions can be attributed to the assignment of $^+NH_3$ bend. Some of the bands, specifically in the regions of 1100 cm^{-1}, 1700 cm^{-1}, and 2800 cm^{-1}, might also aroused from the H-bonding of water to the neutral or zwitterionic forms of β-alanine. The most intense band at 3579 cm^{-1} in the ν(OH) region of 500 ppm water-doped sample spectra, however, are not consistent with the assignment of β-alanine zwitterion or H-bonding of water with β-alanine. We suspected the band to be the absorption of β-alanine dimers in solid parahydrogen. As to how β-alanine dimers is formed with the increase in the amino acid zwitterions in isolated solid parahydrogen environment is still under investigation. Lastly, we noticed the present of several congregated new bands in various regions of our spectra, implying the present of multiple conformer configurations of β-alanine zwitterion within our parahydrogen matrix. Currently, we are attempting to perform high accuracy theoretical calculations of all predicted β-alanine zwitterion conformers, in association with the hydration effect of water molecule towards the amino acid sample, to aid us in completing the spectral assignments of this experiment in the near future.

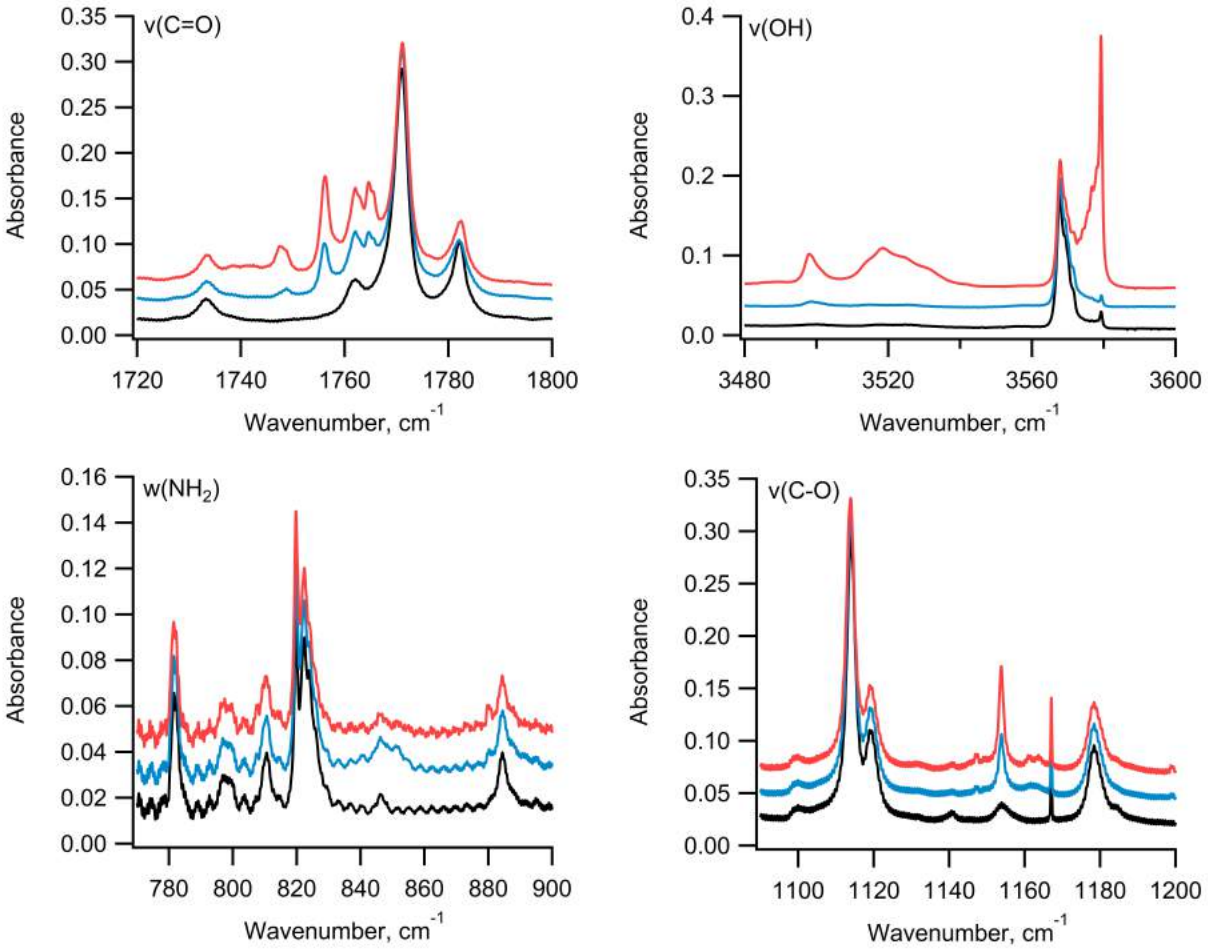

Figure 5.13: FTIR spectra of β-alanine in solid parahydrogen in the regions of ν(OH), ν(C=O), ν(C-O), and $\omega(NH_2)$ taken immediately after deposition. For each panel, the bottom black trace denotes the sample without water dosage, the middle blue trace denotes the sample with 100 ppm of water dopant, and the top red trace denotes the sample with 500 ppm of water dopant.

Chapter 6

Conclusion

For the presented work, we have reported the conformational and UV photochemistry studies of two of the simplest amino acid, β- and α-alanine, using MI-FTIR spectroscopy. Parahydrogen matrices were mainly employed for our study, and we compared the results obtained in solid parahydrogen to those obtained in argon matrices. Due to the soft quantum nature of solid parahydrogen, the matrix imposed several advantages over argon matrix in conformational studies of amino acids. Noble gas matrices like solid argon often suffer from site splitting effect; solid parahydrogen, however, is free from such effect, allowing us to obtain cleaner spectra which correspond to simpler conformational analysis process. We have also managed to trapped highly unstable amino acids conformers within parahydrogen matrix, which are previously unobserved in noble gas matrices. On another note, solid parahydrogen is better than noble gas at sustaining the conformational population of amino acids as present in their sublimating temperature, giving us a more accurate interpretation on the conformers distribution in the gas phase. As on UV photolysis investigation, we observed more efficient *in-situ* UV irradiation outcomes for samples encaged in the parahydrogen matrices as compared to argon matrices. These aspects have thus highlighted the strength of using parahydrogen matrices for spectroscopic investigation of molecules with large conformational flexibility.

FTIR spectra of β-alanine isolated in solid parahydrogen were registered for the first time. Together with theoretical spectra of eleven stable β-alanine conformers obtained at the B3LYP/aug$-$cc$-$pVTZ level of theory and *in-situ* UV-irradiation, the spectral characterization of five conformers, conformer I, II, III, IV, and VII, was accomplished. On the other hand, only four conformers, conformer I, II, VI, and VII, were observer in solid argon, with highly unstable conformer III being undetected in the rare gas matrices. *In-situ* UV-irradiation resulted in conformational change of β-alanine, with a decrease in band intensities for conformer I, II, and VII and an increase for conformer III and VI.

FTIR spectra of α-alanine isolated in solid parahydrogen were registered for the first time. A comparison between the theoretical spectra of eight stable α-alanine conformers calculated at the B3LYP/aug$-$cc$-$pVTZ level of theory and the recorded FTIR spectra shows that four conformers, conformer I, II, IV, and V are present in the parahydrogen matrices. On another note, only two conformers, conformer I and II were detected in the argon matrices, and the higher energy conformers, conformer IV and V, were unobserved. Upon prolonged UV-irradiation, α-alanine underwent total phototdestruction to yield CO_2 and several photoproducts. We expanded our investigation on UV photolysis of α-alanine to the deuterated analogue of the amino

acid, in the hope to simplify our analysis on the photoproducts' bands. However, the full identification of these photoproducts are still incomplete and we are in the process of matching the photoproducts' signals to the seventeen possible product candidates we predicted.

Lastly, we have successfully produced and detected β-alanine zwitterions in solid parahydrogen. We accomplished the formation of zwitterions by doping the appropriate amount of water into our matrix system, leading to the H_2O-assisted proton transfer in the amino acid. We deduced the possibility of multiple β-alanine zwitterion conformers in the parahydrogen matrices from the present of several congregated new bands in various regions of our spectra. We are currently attempting to identify these new bands by utilizing high accuracy computational method, with consideration of hydration effect from the doped water, on several β-alanine zwitterion conformer candidates and then comparing the resulting theoretical wavenumbers to our experimental spectral signals. We also suspected the production of β-alanine dimers in the parahydrogen matrices upon the increase in zwitterion concentration, allocated by the observation an intense band at 3579 cm^{-1} in the highly water-doped solid parahydrogen spectra.

Chapter 7

Future Work

7.1 Conformational, UV Photochemistry, and Zwitterion Studies of Other Amino Acids

Solid parahydrogen has proven to be a superior matrix for the spectroscopic studies of neutral or ionic sample with high conformational flexibility. *In-situ* UV-irradiation in parahydrogen matrix has also shown to be more effective than in argon matrix. Proceeding our success in conformational analysis of β- and α-alanine in solid parahydrogen, we hope to extend our investigation to other simple amino acids, and the candidates for our next studies are serine, aspartic acid and glutamic acid (Figure 7.1). These amino acids contain an α-amino group (-NH_2), an α-carboxylic acid group (-COOH), and a side chain with another carboxylic acid latched to its end. With the present of two acidic end points on the molecules, we predicted that the formation of zwitterions would be more accessible through these amino acids. We would also like to perturb the zwitterions formed in solid parahydrogen with UV-irradiation and study the photochemistry reaction of amino acids zwitterions in cold isolated environment.

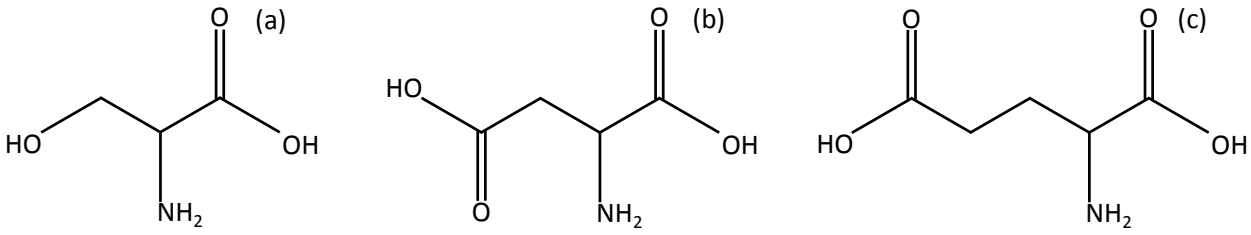

Figure 7.1: Structure of (a) serine, (b) aspartic acid, and (c) glutamic acid.

7.2 Investigation on The Vibrational Dephasing of Molecules in Solid Parahydrogen, and The Annealing Effect in Parahydrogen and Argon Matrices

Sharper spectral signal is expected to be produced with solid parahydrogen FTIR spectroscopy as compared to rare gases (see Section 2.1.2). However, for our amino acids experiments, the spectral linewidth in

parahydrogen matrices appeared to be slightly broader than in argon matrices. This observation indicated the occurrence of fast vibrational dephasing of molecules with large flexibility in parahydrogen crystal (see Section 5.1.3). Due to the broader linewidth, conformers bands of close proximity tended to overlap in parahydrogen matrices, making this features unfavourable for the spectral identification.

A way to check on vibrational dephasing effect is to perform MI-FTIR spectroscopy at a lower temperature than 4 K. We have recently partaken in this investigation using a liquid helium cryostat chamber, where the temperature of the cold window could be brought down to as low as 2.2 K. The lower temperature limit at 2.2 K also allowed us to investigate the annealing effect of parahydrogen matrix on the trapped amino acids. We used α-alanine (sublimated at 425 K) as the principle sample for this investigation and compared the spectra taken in solid parahydrogen to those in argon matrices.

Figure 7.2 shows the spectral result of α-alanine deposited at 2.2 K in solid parahydrogen and underwent multiple annealing process to 4.2 K. After the first annealing process, we observed the upward shift of wavenumber in the solid parahydrogen spectra. If this observation was caused by the vibrational dephasing of trapped α-alanine, we expect the peak shifting process to be reproducible and reversible with varying temperature. However, the wavenumber position remained relatively constant upon the second and third annealing process, indicating the shift in wavenumber observed during the first annealing process was just a result of matrix annealing effect. On another note, the spectral linewidth in 2.2 K parahydrogen matrices did not improve much from the linewidth as deposited at 4 K, being still generally broader than the linewidth in argon matrices.

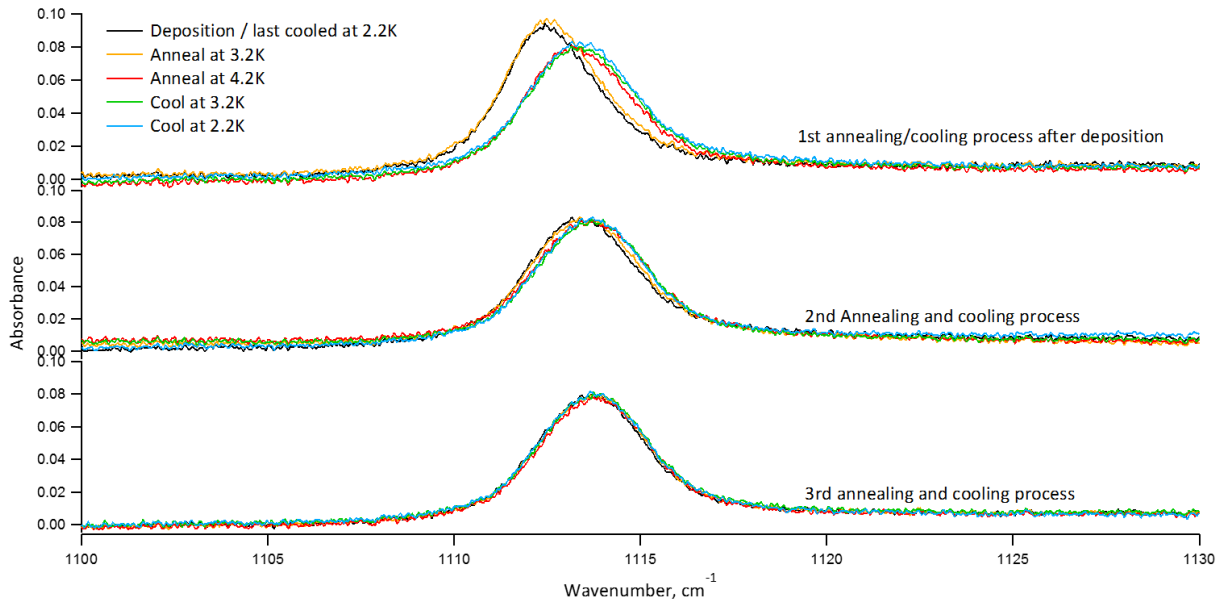

Figure 7.2: FTIR spectra of α-alanine in solid parahydrogen deposited at 2.2 K and subjected to multiple annealing processes to 4.2 K. Minimal to no spectral change was observed upon the 2^{nd} and 3^{rd} annealing processes. The signal shown is the ν(C-O) band of conformer I.

As for the spectral of α-alanine deposited in solid argon at 2.2 K (Figure 7.3), we did not detect any spectral change, even during the first annealing process to 4.2 K. We deduced that the annealing temperature

range might be too low and narrow for the crystalline argon environment. Thus, we repeated the annealing experiment of α-alanine in argon matrices in our closed-cycle refrigerator cryostat chamber, depositing our sample at 18 K and annealing the argon crystal up to a temperature of 35 K (Figure 7.4). Interestingly, we observed a reversible spectral shift after the first annealing process, where the wavenumber experienced a blue-shift upon heating the matrix up to 35 K, and a red-shift upon cooling it down to 4 K.

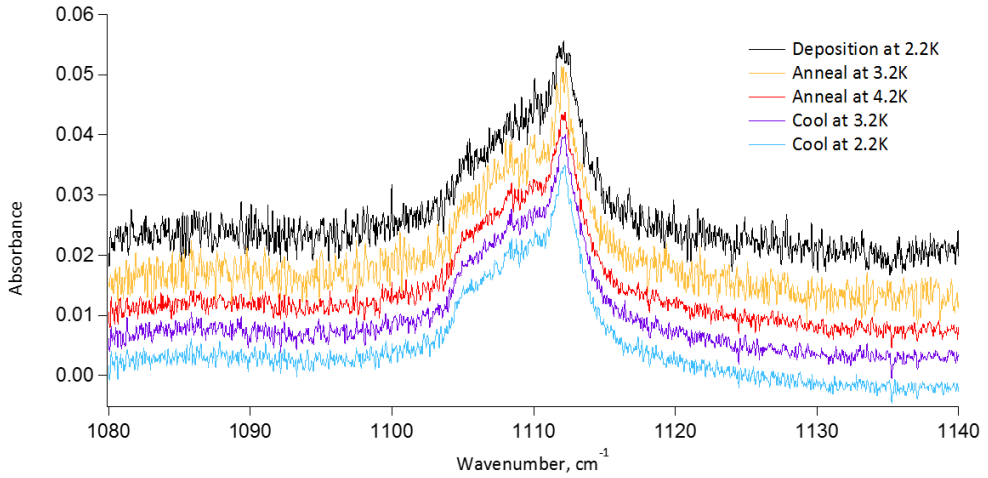

Figure 7.3: FTIR spectra of α-alanine in solid argon deposited at 2.2 K and annealed to 4.2 K. Minimal to no spectral change was observed even on the 1^{st} annealing process. The signal shown is the ν(C-O) band of conformer I.

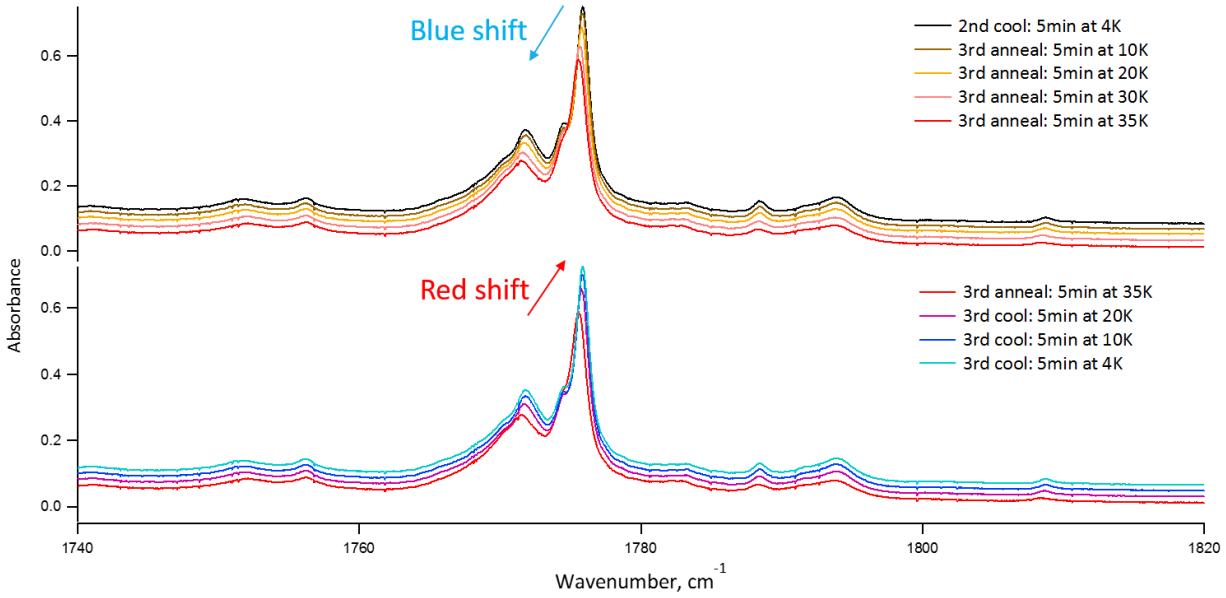

Figure 7.4: FTIR spectra of α-alanine in solid argon deposited at 18 K and subjected to multiple annealing processes to 35 K. The sample was cooled to 4 K before taking the deposition spectrum. The spectral bands exhibited a blue-shift with the increase in matrix temperature, and a red-shift with the decrease. The signal shown is the ν(C=O) band of conformer I.

7.3 Chirality Studies of Amino Acid in Matrix-Isolation System

Another interesting project to be consider for the spectroscopy of amino acid in matrix environment is the investigation of the molecules' chiral nature. As mention previously (see Section 2.2.2), homochirality is believed to be a pre-requisite for the origin of life. Therefore, the investigation of homochirality in biological molecules, including amino acids, is of a topic of high interest.

Monomeric enantiomers are known to exhibit the same vibrational behaviours, deeming them indistinguishable under IR spectroscopy. A way to get around this problem is to make dimer clusters of enantiopure or racemic composition, then measure and compare the molecule-to-molecule interactions between homo- and heterochiral dimers. This proposal has proven to be successful through the conduction of several IR spectroscopies of various gaseous chiral molecules with supersonic expansions techniques [105]. Therefore, we would like to apply similar principle and procedure in a matrix-isolation system, and hope to expand the study of chiral molecules in the matrix-isolation field.

Bibliography

[1] Brian A. Tom, Siddhartha Bhasker, Yuki Miyamoto, Takamasa Momose, and Benjamin J. McCall. Producing and quantifying enriched para-H[sub 2]. *Review of Scientific Instruments*, 80(1):016108, 2009. ISSN 00346748. doi:10.1063/1.3072881. → pages iii, 15, 16, 17

[2] Angel Ying-Tung Wong, Shin Yi Toh, Pavle Djuricanin, and Takamasa Momose. Conformational composition and population analysis of -alanine isolated in solid parahydrogen. *Journal of Molecular Spectroscopy*, 310:23–31, April 2015. ISSN 00222852. doi:10.1016/j.jms.2015.01.002. → pages iii, 9, 29

[3] Angel Ying-Tung Wong. Matrix-Isolation FT-IR Spectroscopy of Amino Acids. Bachelor's thesis, University of British Columbia, April 2014. → pages iii

[4] Angel Ying-Tung Wong, Shin Yi Toh, Pavle Djuricanin, and Takamasa Momose. Conformational Analysis of Gaseous -alanine: A Solid Parahydrogen and Argon Matrix Isolation FT-IR Study. Manuscript in preparation. 2016. → pages iii, 9, 40

[5] Yi-Jehng Kuan, Steven B. Charnley, Hui-Chun Huang, Wei-Ling Tseng, and Zbigniew Kisiel. Interstellar glycine. *The Astrophysical Journal*, 593(2):848, 2003. → pages 1

[6] Lewis E. Snyder, Francis J. Lovas, J. M. Hollis, D. N. Friedel, P. R. Jewell, A. Remijan, V. V. Ilyushin, E. A. Alekseev, and S. F. Dyubko. A rigorous attempt to verify interstellar glycine. *The Astrophysical Journal*, 619(2):914, 2005. → pages 1

[7] M. R. Cunningham, P. A. Jones, P. D. Godfrey, D. M. Cragg, I. Bains, M. G. Burton, P. Calisse, N. H. M. Crighton, S. J. Curran, T. M. Davis, J. T. Dempsey, B. Fulton, M. G. Hidas, T. Hill, L. Kedziora-Chudczer, V. Minier, M. B. Pracy, C. Purcell, J. Shobbrook, and T. Travouillon. A search for propylene oxide and glycine in Sagittarius B2 (LMH) and Orion. *Monthly Notices of the Royal Astronomical Society*, 376(3):1201–1210, April 2007. ISSN 0035-8711, 1365-2966. doi:10.1111/j.1365-2966.2007.11504.x. → pages 1

[8] Oliver Botta, Zita Martins, and Pascale Ehrenfreund. Amino acids in Antarctic CM1 meteorites and their relationship to other carbonaceous chondrites. *Meteoritics & Planetary Science*, 42(1):81–92, 2007. → pages 1, 10

[9] James G. Lawless. Amino acids in the Murchison meteorite. *Geochimica et Cosmochimica Acta*, 37 (9):2207–2212, 1973. → pages 10

[10] Daniel P. Glavin, Jason P. Dworkin, Andrew Aubrey, Oliver Botta, James H. Doty, Zita Martins, and Jeffrey L. Bada. Amino acid analyses of Antarctic CM2 meteorites using liquid chromatography-time of flight-mass spectrometry. *Meteoritics & Planetary Science*, 41(6):889–902, 2006. → pages

[11] Mark A. Sephton. Organic compounds in carbonaceous meteorites. *Natural Product Reports*, 19(3): 292–311, May 2002. ISSN 02650568, 14604752. doi:10.1039/b103775g. → pages

[12] Oliver Botta and Jeffrey L. Bada. Extraterrestrial Organic Compounds in Meteorites. *Surveys in Geophysics*, 23(5):411–467, September 2002. ISSN 0169-3298, 1573-0956. doi:10.1023/A:1020139302770. → pages 1

[13] S. Pizzarello, R. V. Krishnamurthy, S. Epstein, and J. R. Cronin. Isotopic analyses of amino acids from the Murchison meteorite. *Geochimica et Cosmochimica Acta*, 55(3):905–910, March 1991. ISSN 0016-7037. doi:10.1016/0016-7037(91)90350-E. → pages 1

[14] Pascale Ehrenfreund, Daniel P. Glavin, Oliver Botta, George Cooper, and Jeffrey L. Bada. Extraterrestrial amino acids in Orgueil and Ivuna: Tracing the parent body of CI type carbonaceous chondrites. *Proceedings of the National Academy of Sciences*, 98(5):2138–2141, 2001. → pages 1, 10

[15] E. T. Peltzer, J. L. Bada, G. Schlesinger, and S. L. Miller. The chemical conditions on the parent body of the Murchison meteorite: some conclusions based on amino, hydroxy and dicarboxylic acids. *Advances in space research: the official journal of the Committee on Space Research (COSPAR)*, 4(12):69–74, 1984. ISSN 0273-1177. → pages 1

[16] Voislav Blagojevic, Simon Petrie, and Diethard K. Bohme. Gas-phase syntheses for interstellar carboxylic and amino acids. *Monthly Notices of the Royal Astronomical Society*, 339(1):L7–L11, 2003. → pages 1, 10

[17] Antonio Largo, Pilar Redondo, and Carmen Barrientos. Theoretical study of possible ion-molecule reactions leading to precursors of glycine in the interstellar medium. *International Journal of Quantum Chemistry*, 98(4):355–360, 2004. ISSN 0020-7608, 1097-461X. doi:10.1002/qua.20070. → pages 1

[18] Bernard Barbier, Annie Chabin, Didier Chaput, and André Brack. Photochemical processing of amino acids in Earth orbit. *Planetary and Space Science*, 46(4):391–398, April 1998. ISSN 0032-0633. doi:10.1016/S0032-0633(97)00150-5. → pages 1

[19] Stepan G. Stepanian, Alexander Yu. Ivanov, Daryna A. Smyrnova, and Ludwik Adamowicz. UV-induced isomerization of -alanine isolated in argon matrices. *Journal of Molecular Structure*, 1025:6–19, October 2012. ISSN 00222860. doi:10.1016/j.molstruc.2012.04.093. → pages 1, 9, 11, 30, 40

[20] P. Ehrenfreund, M. P. Bernstein, J. P. Dworkin, S. A. Sandford, and L. J. Allamandola. The photostability of amino acids in space. *The Astrophysical Journal Letters*, 550(1):L95, 2001. → pages 1, 2, 60

[21] Paul V. Johnson, Robert Hodyss, Victoria F. Chernow, Dawn M. Lipscomb, and Jay D. Goguen. Ultraviolet photolysis of amino acids on the surface of icy Solar System bodies. *Icarus*, 221(2): 800–805, November 2012. ISSN 00191035. doi:10.1016/j.icarus.2012.09.005. → pages 1

[22] A. J. Barnes, W. J. Orville-Thomas, A. Müller, and R. Gaufrès, editors. *Matrix Isolation Spectroscopy*, volume 76. Springer Netherlands, Dordrecht, 1981. ISBN 978-94-009-8542-1 978-94-009-8540-7. → pages 2, 3, 4, 6, 7, 9

[23] Eric Whittle, David A. Dows, and George C. Pimentel. Matrix Isolation Method for the Experimental Study of Unstable Species. *The Journal of Chemical Physics*, 22(11):1943–1943, November 1954. ISSN 0021-9606, 1089-7690. doi:10.1063/1.1739957. → pages 3

[24] Marilyn E. Jacox. On Walking in the Footprints of Giants *. *Annual Review of Physical Chemistry*, 61(1):1–18, March 2010. ISSN 0066-426X, 1545-1593. doi:10.1146/annurev.physchem.012809.103439. → pages 3, 4

[25] Dolphus E. Milligan and Marilyn E. Jacox. Infrared Spectroscopic Evidence for the Species HO2. *The Journal of Chemical Physics*, 38(11):2627, 1963. ISSN 00219606. doi:10.1063/1.1733562. → pages 3

[26] Marilyn E. Jacox. The spectroscopy of molecular reaction intermediates trapped in the solid rare gases. *Chemical Society Reviews*, 31(2):108–115, March 2002. ISSN 03060012, 14604744. doi:10.1039/b102907j. → pages 4

[27] Marilyn E. Jacox. Vibrational and electronic energy levels of polyatomic transient molecules: Supplement 1. *Journal of Physical and Chemical Reference Data*, 19(6):1387–1546, November 1990. ISSN 0047-2689, 1529-7845. doi:10.1063/1.555848. → pages 4

[28] Marilyn E. Jacox. Vibrational and Electronic Energy Levels of Polyatomic Transient Molecules. Supplement A. *Journal of Physical and Chemical Reference Data*, 27(2):115–393, March 1998. ISSN 0047-2689, 1529-7845. doi:10.1063/1.556017. → pages

[29] Marilyn E. Jacox. Vibrational and Electronic Energy Levels of Polyatomic Transient Molecules. Supplement B. *Journal of Physical and Chemical Reference Data*, 32(1):1–441, March 2003. ISSN 0047-2689, 1529-7845. doi:10.1063/1.1497629. → pages 4

[30] V. E. Bondybey and V. A. Apkarian. Preface. *Chemical Physics*, 189(2):137–138, December 1994. ISSN 0301-0104. doi:10.1016/0301-0104(94)89003-X. → pages 4

[31] Ingeborg Iping Petterson. Marilyn Jacox, a Pioneer in Infrared Spectroscopy. *Spectroscopy*, 29(6): 40–44, June 2014. ISSN 08876703. → pages 4

[32] Takamasa Momose and Tadamasa Shida. Matrix-Isolation Spectroscopy Using Solid Parahydrogen as the Matrix: Application to High-Resolution Spectroscopy, Photochemistry, and Cryochemistry. *Bulletin of the Chemical Society of Japan*, 71(1):1–15, 1998. ISSN 0009-2673. doi:10.1246/bcsj.71.1. → pages 4, 6, 7, 8, 38

[33] Takamasa Momose, Hiroyuki Katsuki, Hiromichi Hoshina, Norihito Sogoshi, Tomonari Wakabayashi, and Tadamasa Shida. High-resolution laser spectroscopy of methane clusters trapped in solid parahydrogen. *The Journal of Chemical Physics*, 107(19):7717–7720, November 1997. ISSN 0021-9606, 1089-7690. doi:10.1063/1.475086. → pages 4, 6

[34] Donald L. Pavia, Gary M. Lampman, George S. Kriz, and James A. Vyvyan. *Introduction to Spectroscopy*. Cengage Learning, 4th edition edition, March 2009. → pages 5

[35] Douglas A. Skoog, F. James Holler, and Stanley R. Crouch. *Principles of Instrumental Analysis*. Thomson Brooks/Cole, 6th edition edition, 2007. ISBN 978-0-495-01201-6. → pages 5, 6

[36] *User's Manual for IFS 125HR*. Bruker Optik GmbH, 1st edition edition, April 2006. ISBN I26013. → pages 5

[37] Takamasa Momose, Hiromichi Hoshina, Mizuho Fushitani, and Hiroyuki Katsuki. High-resolution spectroscopy and the analysis of ro-vibrational transitions of molecules in solid parahydrogen. *Vibrational Spectroscopy*, 34(1):95–108, January 2004. ISSN 09242031. doi:10.1016/j.vibspec.2003.06.001. → pages 6, 7, 8, 38

[38] Takeshi Oka. High-resolution spectroscopy of solid hydrogen. *Annual Review of Physical Chemistry*, 44(1):299–333, 1993. → pages 6, 7, 8

[39] Justinas Ceponkus, Wutharath Chin, Michèle Chevalier, Michel Broquier, André Limongi, and Claudine Crépin. Infrared study of glycolaldehyde isolated in parahydrogen matrix. *The Journal of Chemical Physics*, 133(9):094502, 2010. ISSN 00219606. doi:10.1063/1.3474994. → pages 6, 7

[40] Isaac F. Silvera. The solid molecular hydrogens in the condensed phase: Fundamentals and static properties. *Reviews of Modern Physics*, 52(2):393–452, April 1980. doi:10.1103/RevModPhys.52.393. → pages 7, 8

[41] Mitchio Okumura, Man-Chor Chan, and Takeshi Oka. High-Resolution Infrared Spectroscopy of Solid Hydrogen: The Tetrahexacontapole-Induced J= 6 Transitions. *Physical review letters*, 62(1): 32, 1989. → pages 7

[42] D. P. Weliky, T. J. Byers, K. E. Kerr, T. Momose, R. M. Dickson, and T. Oka. High-resolution laser spectroscopy of theQ v (0) transitions in solid parahydrogen. *Applied Physics B*, 59(3):265–281, 1994. → pages 8

[43] Peter Klaeboe and Claus J. Nielsen. Recent advances in infrared matrix isolation spectroscopy. Invited lecture. *Analyst*, 117(3):335–341, 1992. → pages 9

[44] Peter Klaeboe. Conformational studies by vibrational spectroscopy: a review of various methods. *Vibrational Spectroscopy*, 1(9):3–17, 1995. ISSN 0924-2031. → pages 9

[45] S.G Stepanian, I. D. Reva, E. D. Radchenko, and L Adamowicz. Conformational Behavior of -Alanine. Matrix-Isolation Infrared and Theoretical DFT and ab Initio Study. *Journal of Physical Chemistry A*, 102(24), 1998. ISSN 1089-5639. doi:10.1021/jp973479z. → pages 9, 12, 42

[46] Igor D. Reva, Alexander M. Plokhotnichenko, Stepan G. Stepanian, Alexander Yu. Ivanov, Eugeni D. Radchenko, Galina G. Sheina, and Yuri P. Blagoi. The rotamerization of conformers of glycine isolated in inert gas matrices. An infrared spectroscopic study. *Chemical Physics Letters*, 232:141–148, January 1995. ISSN 0009-2614. doi:10.1016/0009-2614(95)90630-B. → pages 9

[47] Gábor Bazsó, Eszter E. Najbauer, Gábor Magyarfalvi, and György Tarczay. Near-Infrared Laser Induced Conformational Change of Alanine in Low-Temperature Matrixes and the Tunneling Lifetime of Its Conformer VI. *The Journal of Physical Chemistry A*, 117(9):1952–1962, March 2013. ISSN 1089-5639, 1520-5215. doi:10.1021/jp400196b. → pages 9, 12, 13, 42

[48] A. Yu. Ivanov, A. M. Plokhotnichenko, V. Izvekov, G. G. Sheina, and Yu. P. Blagoi. FTIR investigation of the effect of matrices (Kr, Ar, Ne) on the UV-induced isomerization of the monomeric links of biopolymers. *Journal of Molecular Structure*, 408409:459–462, June 1997. ISSN 0022-2860. doi:10.1016/S0022-2860(96)09554-3. → pages

[49] A. Yu Ivanov, G. Sheina, and Yu P. Blagoi. FTIR spectroscopic study of the UV-induced rotamerization of glycine in the low temperature matrices (Kr, Ar, Ne). *Spectrochimica Acta Part A: Molecular and Biomolecular Spectroscopy*, 55(1):219–228, 1999. → pages

[50] Eszter E. Najbauer, G*á*bor Bazs, S*á*ndor G*ó*bi, G*á*bor Magyarfalvi, and GyÖrgy Tarczay. Exploring the Conformational Space of Cysteine by Matrix Isolation Spectroscopy Combined with Near-Infrared Laser Induced Conformational Change. *The Journal of Physical Chemistry B*, 118(8): 2093–2103, February 2014. ISSN 1520-6106, 1520-5207. doi:10.1021/jp412550q. → pages

[51] Eszter E. Najbauer, G*á*bor Bazs*ó*, Rui Ap*ó*stolo, Rui Fausto, Malgorzata Biczysko, Vincenzo Barone, and Gy*ö*rgy Tarczay. Identification of Serine Conformers by Matrix-Isolation IR Spectroscopy Aided by Near-Infrared Laser-Induced Conformational Change, 2d Correlation Analysis, and Quantum Mechanical Anharmonic Computations. *The Journal of Physical Chemistry B*, 119(33):10496–10510, August 2015. ISSN 1520-6106, 1520-5207. doi:10.1021/acs.jpcb.5b05768. → pages 9

[52] C. E. Blom, R. P. Mller, and Hs H. G*ü*nthard. S-trans and S-cis acrolein: trapping from thermal molecular beams and uv-induced isomerization in argon matrices. *Chemical Physics Letters*, 73(3): 483–486, 1980. → pages 9

[53] Ana Borba, Andrea G*ó*mez-Zavaglia, Leszek Lapinski, and R. Fausto. Rotational isomers of lactic acid: first experimental observation of higher energy forms. *Phys. Chem. Chem. Phys.*, 6(9): 2101–2108, 2004. ISSN 1463-9076, 1463-9084. doi:10.1039/B316642B. → pages 9

[54] P. Huber-W*ä*lchli and Hs H. G*ü*nthard. Trapping of unstable conformations from thermal molecular beams in argon matrices: 1, 2-difluoroethane and 1, 3-butadiene, ir spectra and conformer equilibria. *Spectrochimica Acta Part A: Molecular Spectroscopy*, 37(5):285–304, 1981. → pages 9

[55] Rolando R. Lozada-Garcia, Justinas Ceponkus, Wutharath Chin, Michè*l*e Chevalier, and Claudine Cr*é*pin. Acetylacetone in hydrogen solids: IR signatures of the enol and keto tautomers and UV induced tautomerization. *Chemical Physics Letters*, 504(4-6):142–147, March 2011. ISSN 00092614. doi:10.1016/j.cplett.2011.01.055. → pages 9

[56] I.D Reva, S.G Stepanian, L Adamowicz, and R Fausto. Missing conformers. Comparative study of conformational cooling in cyanoacetic acid and methyl cyanoacetate isolated in low temperature inert gas matrixes. *Chemical Physics Letters*, 374(5-6):631–638, June 2003. ISSN 00092614. doi:10.1016/S0009-2614(03)00782-6. → pages 9

[57] Michael Ramek. Ab initio SCF investigation of -alanine. *Journal of Molecular Structure: THEOCHEM*, 208(34):301–355, September 1990. ISSN 0166-1280. doi:10.1016/0166-1280(90)80014-F. → pages 10, 31

[58] Shane J. McGlone and Peter D. Godfrey. Rotational Spectrum of a Neurohormone:. beta.-Alanine. *Journal of the American Chemical Society*, 117(3):1043–1048, 1995. → pages 10

[59] M. Eugenia Sanz, Alberto Lesarri, M. Isabel Pe*ñ*a, Vanesa Vaquero, Vanessa Cortijo, Juan C. L*ó*pez, and Jos*é* L. Alonso. The Shape of -Alanine. *Journal of the American Chemical Society*, 128(11): 3812–3817, March 2006. ISSN 0002-7863, 1520-5126. doi:10.1021/ja058194b. → pages 10, 38

[60] M*á*rio T*ú*lio S. Rosado, Maria Leonor RS Duarte, and Rui Fausto. Vibrational spectra (FT-IR, Raman and MI-IR) of -and -alanine. *Journal of Molecular Structure*, 410:343–348, June 1997. → pages 10, 11, 12

[61] Jan Cz. Dobrowolski, Michal H. Jamr*óz*, Robert Kolos, Joanna E. Rode, and Joanna Sadlej. IR Low-Temperature Matrix and ab Initio Study on -Alanine Conformers. *ChemPhysChem*, 9(14): 2042–2051, October 2008. ISSN 14394235, 14397641. doi:10.1002/cphc.200800383. → pages 11

[62] Stepan G. Stepanian, Alexander Yu Ivanov, and Ludwik Adamowicz. FTIR spectra and conformational structure of deutero--alanine isolated in argon matrices. *Journal of Molecular Spectroscopy*, 320:13–24, February 2016. ISSN 00222852. doi:10.1016/j.jms.2015.12.010. → pages 11

[63] J. Bailey, A. Chrysostomou, J. H. Hough, T. M. Gledhill, A. McCall, S. Clark, F. Ménard, and M. Tamura. Circular polarization in star-formation regions: implications for biomolecular homochirality. *Science (New York, N.Y.)*, 281(5377):672–674, July 1998. ISSN 0036-8075. → pages 11

[64] William A. Bonner. Terrestrial and extraterrestrial sources of molecular homochirality. *Origins of Life and Evolution of the Biosphere*, 21(5-6):407–420, 1991. → pages 11

[65] John R. Cronin and Sandra Pizzarello. Enantiomeric Excesses in Meteoritic Amino Acids. *Science*, 275(5302):951–955, February 1997. ISSN 0036-8075, 1095-9203. doi:10.1126/science.275.5302.951. → pages 11

[66] M. H. Engel and S. A. Macko. Isotopic evidence for extraterrestrial non- racemic amino acids in the Murchison meteorite. *Nature*, 389(6648):265–268, September 1997. ISSN 0028-0836. doi:10.1038/38460. → pages 11

[67] Scott Gronert and Richard AJ O'Hair. Ab initio studies of amino acid conformations. 1. The conformers of alanine, serine, and cysteine. *Journal of the American Chemical Society*, 117(7): 2071–2081, 1995. → pages 11

[68] M. Cao, S. Q. Newton, J. Pranata, and L. Schäfer. AB INITIO CONFORMATIONAL ANALYSIS OF ALANINE. *Journal of molecular structure. Theochem*, 332(3):251–267, 1995. ISSN 0166-1280. → pages 11

[69] Attila G. Császár. Conformers of gaseous -alanine. *The Journal of Physical Chemistry*, 100(9): 3541–3551, 1996. → pages 11, 12, 42, 52, 57

[70] Roman M. Balabin. Conformational equilibrium in alanine: Focal-point analysis and ab initio limit. *Computational and Theoretical Chemistry*, 965(1):15–21, April 2011. ISSN 2210271X. doi:10.1016/j.comptc.2011.01.008. → pages 12, 42

[71] Kinya Iijima and Brian Beagley. An electron diffraction study of gaseous -alanine, NH 2chch 3co 2h. *Journal of Molecular Structure*, 248:133–142, August 1991. ISSN 0022-2860. doi:10.1016/0022-2860(91)85008-Q. → pages 12

[72] K Iijima and M Nakano. Reinvestigation of molecular structure and conformation of gaseous l-alanine by joint analysis using electron diffraction data and rotational constants. *Journal of Molecular Structure*, 485486:255–260, August 1999. ISSN 0022-2860. doi:10.1016/S0022-2860(99)00047-2. → pages 12

[73] P. D. Godfrey, S. Firth, L. D. Hatherley, R. D. Brown, and A. P. Pierlot. Millimeter-wave spectroscopy of biomolecules: alanine. *Journal of the American Chemical Society*, 115(21): 9687–9691, October 1993. ISSN 0002-7863. doi:10.1021/ja00074a039. → pages 12

[74] Peter D. Godfrey, Ronald D. Brown, and Fiona M. Rodgers. Spectroscopy and Quantum Chemical Theory Applied to Problems in Molecular StructureThe missing conformers of glycine and alanine: relaxation in seeded supersonic jets. *Journal of Molecular Structure*, 376(1):65–81, February 1996. ISSN 0022-2860. doi:10.1016/0022-2860(95)09065-7. → pages

[75] Susana Blanco, Alberto Lesarri, Juan C. L*ó*pez, and Jos*é* L. Alonso. The Gas-Phase Structure of Alanine. *Journal of the American Chemical Society*, 126(37):11675–11683, September 2004. ISSN 0002-7863, 1520-5126. doi:10.1021/ja048317c. → pages 12

[76] Y. Hirata, S. Kubota, S. Watanabe, T. Momose, and K. Kawaguchi. Millimeter-wave spectroscopy of -alanine. *Journal of Molecular Spectroscopy*, 251(1-2):314–318, September 2008. ISSN 00222852. doi:10.1016/j.jms.2008.03.022. → pages 12

[77] Rolf Linder, Kai Seefeld, Andreas Vavra, and Karl Kleinermanns. Gas phase infrared spectra of nonaromatic amino acids. *Chemical Physics Letters*, 453(1-3):1–6, February 2008. ISSN 00092614. doi:10.1016/j.cplett.2007.12.069. → pages

[78] Roman M. Balabin. The identification of the two missing conformers of gas-phase alanine: a jet-cooled Raman spectroscopy study. *Physical Chemistry Chemical Physics*, 12(23):5980, 2010. ISSN 1463-9076, 1463-9084. doi:10.1039/b924029b. → pages 12, 52, 57

[79] H. Farrokhpour, F. Fathi, and A. Naves De Brito. Theoretical and Experimental Study of Valence Photoelectron Spectrum of d , l -Alanine Amino Acid. *The Journal of Physical Chemistry A*, 116(26):7004–7015, July 2012. ISSN 1089-5639, 1520-5215. doi:10.1021/jp3023716. → pages

[80] Bert Lambie, Riet Ramaekers, and Guido Maes. On the contribution of intramolecular H-bonding entropy to the conformational stability of alanine conformations. *Spectrochimica Acta Part A: Molecular and Biomolecular Spectroscopy*, 59(6):1387–1397, 2003. → pages 12, 13, 42, 52

[81] Shoujun Xu, J. Michael Nilles, and Kit H. Bowen. Zwitterion formation in hydrated amino acid, dipole bound anions: How many water molecules are required? *The Journal of Chemical Physics*, 119(20):10696, 2003. ISSN 00219606. doi:10.1063/1.1620501. → pages 13

[82] Yamilet Rodr*í*guez-Lazcano, Bel*é*n Mat*é*, Oscar G*á*lvez, V*í*ctor J. Herrero, Isabel Tanarro, and Rafael Escribano. Solid L--alanine: Spectroscopic properties and theoretical calculations. *Journal of Quantitative Spectroscopy and Radiative Transfer*, 113(11):1266–1275, 2012. → pages 13, 14

[83] Christine M. Aikens and Mark S. Gordon. Incremental Solvation of Nonionized and Zwitterionic Glycine. *Journal of the American Chemical Society*, 128(39):12835–12850, October 2006. ISSN 0002-7863, 1520-5126. doi:10.1021/ja062842p. → pages 13

[84] Yanbo Ding and Karsten Krogh-Jespersen. The glycine zwitterion does not exist in the gas phase: results from a detailed ab initio electronic structure study. *Chemical Physics Letters*, 199(34): 261–266, November 1992. ISSN 0009-2614. doi:10.1016/0009-2614(92)80116-S. → pages

[85] Antonio Fern*á*ndez-Ramos, Zorka Smedarchina, Willem Siebrand, and Marek Z. Zgierski. A direct-dynamics study of the zwitterion-to-neutral interconversion of glycine in aqueous solution. *The Journal of Chemical Physics*, 113(21):9714, 2000. ISSN 00219606. doi:10.1063/1.1322084. → pages

[86] Animesh K. Ojha and Snehasis Bhunia. Different proton transfer channels for the transformation of zwitterionic alanine(H2o) n=2-4 to nonzwitterionic alanine(H2o) n=2-4: a density functional theory study. *Journal of Molecular Modeling*, 20(3), March 2014. ISSN 1610-2940, 0948-5023. doi:10.1007/s00894-014-2124-9. → pages

[87] P. Selvarengan and P. Kolandaivel. Potential energy surface study on glycine, alanine and their zwitterionic forms. *Journal of Molecular Structure: THEOCHEM*, 671(1-3):77–86, February 2004. ISSN 01661280. doi:10.1016/j.theochem.2003.10.021. → pages

[88] Emadeddin Tajkhorshid, K. J. Jalkanen, and S*á*ndor Suhai. Structure and vibrational spectra of the zwitterion L-alanine in the presence of explicit water molecules: a density functional analysis. *The Journal of Physical Chemistry B*, 102(30):5899–5913, 1998. → pages

[89] Francisco R. Tortonda, Juan-Luis Pascual-Ahuir, Estanislao Silla, Iñaki Tuñó*n*, and Francisco J. Ramı́rez. Aminoacid zwitterions in solution: Geometric, energetic, and vibrational analysis using density functional theory-continuum model calculations. *The Journal of Chemical Physics*, 109(2): 592, 1998. ISSN 00219606. doi:10.1063/1.476596. → pages

[90] Basak Turan and Cenk Selcuki. Conformational analysis of glutamic acid: a density functional approach using implicit continuum solvent model. *Journal of Molecular Modeling*, 20(9), September 2014. ISSN 1610-2940, 0948-5023. doi:10.1007/s00894-014-2396-0. → pages 13

[91] Martine N. Blom, Isabelle Compagnon, Nick C. Polfer, Gert von Helden, Gerard Meijer, S*á*ndor Suhai, B*é*la Paizs, and Jos Oomens. Stepwise Solvation of an Amino Acid: The Appearance of Zwitterionic Structures . *The Journal of Physical Chemistry A*, 111(31):7309–7316, August 2007. ISSN 1089-5639, 1520-5215. doi:10.1021/jp070211r. → pages 13

[92] Clifton Espinoza, Jan Szczepanski, Martin Vala, and Nick C. Polfer. Glycine and Its Hydrated Complexes: A Matrix Isolation Infrared Study. *The Journal of Physical Chemistry A*, 114(18): 5919–5927, May 2010. ISSN 1089-5639, 1520-5215. doi:10.1021/jp1014115. → pages 13, 14

[93] A Pawlukoj*ć*, J Leciejewicz, J Tomkinson, and S.F Parker. Neutron spectroscopic study of hydrogen bonding dynamics in l-serine. *Spectrochimica Acta Part A: Molecular and Biomolecular Spectroscopy*, 58(13):2897–2904, November 2002. ISSN 13861425. doi:10.1016/S1386-1425(02)00086-0. → pages

[94] Riet Ramaekers, Joanna Pajak, Bert Lambie, and Guido Maes. Neutral and zwitterionic glycine.H[sub 2]O complexes: A theoretical and matrix-isolation Fourier transform infrared study. *The Journal of Chemical Physics*, 120(9):4182, 2004. ISSN 00219606. doi:10.1063/1.1643735. → pages 13, 14, 60, 62

[95] Thomas Wyttenbach, Matthias Witt, and Michael T. Bowers. On the Stability of Amino Acid Zwitterions in the Gas Phase: The Influence of Derivatization, Proton Affinity, and Alkali Ion Addition. *Journal of the American Chemical Society*, 122(14):3458–3464, April 2000. ISSN 0002-7863, 1520-5126. doi:10.1021/ja992546v. → pages 13

[96] Simon Tam and Mario E. Fajardo. Ortho/para hydrogen converter for rapid deposition matrix isolation spectroscopy. *Review of Scientific Instruments*, 70(4):1926, 1999. ISSN 00346748. doi:10.1063/1.1149734. → pages 15

[97] Jordan R. Schmidt and William F. Polik. WebMO, 2014. URL http://abacus.chem.ubc.ca/webmo/cgi-bin/jobmgr.cgi. → pages 23, 25, 26, 27

[98] Ira Levine. *Physical Chemistry*. McGraw-Hill Education, Boston, 6 edition edition, May 2008. ISBN 978-0-07-253862-5. → pages 24, 25, 28

[99] Joseph W. Ochterski. Thermochemistry in gaussian. *Gaussian Inc, Pittsburgh, PA*, pages 1–17, 2000. → pages 24, 25, 26, 27

[100] Hendrik Zipse. Thermochemistry. URL http://www.cup.uni-muenchen.de/ch/compchem/vib/thermo1.html. → pages 24, 27

[101] Donald A. McQuarrie and John D. Simon. *Molecular Thermodynamics*. University Science Books, Sausalito, California, 1 edition edition, 1999. ISBN 978-1-891389-05-4. → pages 25, 26, 27

[102] Hiroyuki Katsuki and Takamasa Momose. Observation of rovibrational dephasing of molecules in parahydrogen crystals by frequency domain spectroscopy. *Physical review letters*, 84(15):3286, 2000. → pages 38

[103] Takamasa Momose, Masaaki Miki, Tomonari Wakabayashi, Tadamasa Shida, Man-Chor Chan, Steven S. Lee, and Takeshi Oka. Infrared spectroscopic study of rovibrational states of methane trapped in parahydrogen crystal. *The Journal of Chemical Physics*, 107(19):7707–7716, November 1997. ISSN 0021-9606, 1089-7690. doi:10.1063/1.475085. → pages

[104] Takamasa Momose. Rovibrational states of a tetrahedral molecule in a hexagonal close-packed crystal. *The Journal of Chemical Physics*, 107(19):7695–7706, November 1997. ISSN 0021-9606, 1089-7690. doi:10.1063/1.475084. → pages 38

[105] Anne Zehnacker and MartinA. Suhm. Chirality Recognition between Neutral Molecules in the Gas Phase. *Angewandte Chemie International Edition*, 47(37):6970–6992, September 2008. ISSN 14337851, 15213773. doi:10.1002/anie.200800957. → pages 69

Appendix A

Supplementary Material: Conformational Analysis of Gaseous β-alanine in Solid Parahydrogen and Argon Matrices

The following presents raw data from the β-alanine conformational studies discussed in Section 5.1. These include full FTIR spectra taken for each procedure, and tables of theoretically calculated wavenumbers and associated intensities tabulated for each β-alanine conformer candidate.

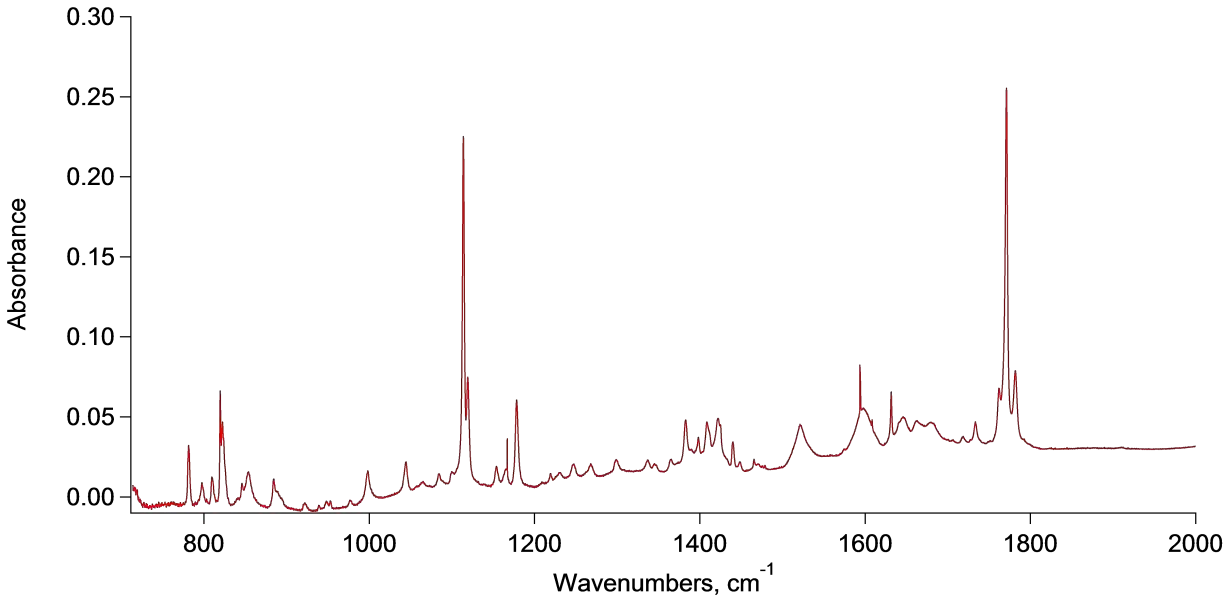

Figure A.1: The 750 - 2000 cm^{-1} region of the FTIR spectrum of β-alanine sublimed at a temperature of 390 K and trapped into a parahydrogen matrix observed immediately after deposition.

Table A.1: Theoretical wavenumbers (cm^{-1}) and intensities ($km \cdot mol^{-1}$) of the eleven β-alanine conformers (Conformer I to XI) calculated at the B3LYP/aug − cc − pVTZ level of theory in the region of 700 - 4800 cm^{-1}.

Conformer I		Conformer II		Conformer III		Conformer IV	
Wavenumber[a], cm^{-1}	Intensity, km mol^{-1}	Wavenumber[a], cm^{-1}	Intensity, km mol^{-1}	Wavenumber[a], cm^{-1}	Intensity, km mol^{-1}	Wavenumber[a], cm^{-1}	Intensity, km mol^{-1}
651.06	91.62	650.91	73.31	685.75	46.73	644.08	79.80
787.74	11.73	771.87	53.03	776.81	95.84	783.70	49.44
836.04	85.96	820.06	174.52	811.62	30.09	821.61	73.87
882.80	29.47	863.20	4.98	888.73	6.97	877.01	8.51
933.38	2.34	918.51	4.37	958.86	4.88	971.69	16.87
1047.64	23.26	1009.91	18.93	993.66	37.63	1039.95	48.71
1092.92	11.75	1107.86	204.42	1066.27	31.78	1082.12	15.56
1108.94	225.45	1173.75	70.21	1099.72	101.35	1114.59	209.07
1182.65	83.86	1234.84	14.84	1195.92	120.37	1158.73	53.14
1217.03	2.33	1286.47	5.90	1244.58	8.85	1246.43	7.88
1289.32	7.87	1358.98	34.74	1293.08	7.25	1283.70	2.04
1328.35	4.79	1374.36	4.22	1322.98	29.13	1313.54	1.33
1386.88	56.23	1389.09	28.28	1358.74	13.93	1364.88	44.13
1405.53	12.58	1427.68	20.49	1403.16	13.09	1414.42	46.82
1423.38	20.70	1465.49	5.14	1448.26	10.82	1439.03	14.01
1481.32	4.38	1631.66	22.82	1490.58	2.99	1493.46	2.15
1629.77	56.58	1752.68	282.32	1633.02	27.50	1634.73	24.54
1770.88	267.48	2886.76	10.93	1782.04	339.53	1776.85	297.74
2840.19	60.14	2903.18	29.52	2827.45	81.49	2846.93	49.94
2901.25	10.24	2917.64	12.65	2905.55	10.39	2898.58	8.06
2924.47	27.50	2942.24	21.51	2935.83	5.36	2923.39	2.74
2936.65	7.03	3342.17	1.94	2960.96	19.47	2944.28	20.77
3345.20	3.25	3420.45	6.85	3342.02	0.68	3337.59	0.63
3418.01	8.12	3564.24	60.16	3419.08	3.37	3411.99	2.31
3567.19	62.66			3573.78	65.04	3567.64	61.25

Table A.1 Continued

Conformer V		Conformer VI		Conformer VII		Conformer VIII	
Wavenumber[a], cm^{-1}	Intensity, km mol^{-1}	Wavenumber[a], cm^{-1}	Intensity, km mol^{-1}	Wavenumber[a], cm^{-1}	Intensity, km mol^{-1}	Wavenumber[a], cm^{-1}	Intensity, km mol^{-1}
685.36	9.50	742.22	43.25	764.71	10.85	671.08	94.45
796.90	18.26	781.80	19.19	795.07	206.46	777.30	8.76
842.92	55.64	841.28	154.49	876.32	4.94	820.81	106.41
894.72	17.82	858.80	48.97	958.81	3.05	876.42	25.04
932.18	29.15	928.48	1.81	1029.20	2.45	916.66	5.57
999.48	7.39	1058.82	46.57	1061.19	84.29	1041.49	32.96
1051.19	9.64	1128.20	113.69	1128.40	241.69	1092.43	8.76
1132.21	8.96	1172.05	88.44	1136.55	0.74	1115.15	151.45
1213.12	93.32	1228.93	42.35	1266.98	1.08	1185.92	94.01
1273.17	15.28	1299.03	7.52	1287.18	0.53	1226.37	2.27
1293.04	2.98	1328.16	62.59	1340.30	26.75	1309.23	17.11
1347.92	4.39	1369.50	1.90	1362.27	0.02	1331.14	18.14
1394.20	12.44	1384.47	8.51	1390.41	55.27	1356.70	5.26
1443.33	8.08	1459.51	12.40	1433.72	12.42	1405.01	17.88
1449.18	226.13	1474.20	1.65	1475.13	4.53	1424.71	6.57
1492.89	5.19	1648.62	19.98	1635.51	27.46	1483.35	3.19
1628.29	28.32	1763.31	297.12	1777.41	298.65	1634.56	35.00
1791.27	439.23	2896.88	28.70	2890.38	5.54	1780.84	351.83
2871.79	54.26	2915.96	3.72	2914.34	2.13	2848.82	56.66
2883.39	6.49	2936.11	27.28	2916.67	20.96	2898.18	9.52
2931.13	19.25	2968.10	14.95	2952.95	21.38	2922.96	26.65
2968.83	6.82	3338.47	2.10	3336.69	1.79	2953.66	6.26
3118.28	709.92	3408.10	6.88	3411.20	1.49	3348.85	0.96
3340.11	1.37	3559.82	60.98	3563.90	55.74	3420.72	5.72
3415.56	9.11					3564.36	64.92

Table A.1 Continued

Conformer IX		Conformer X		Conformer XI	
Wavenumber[a], cm^{-1}	Intensity, km mol^{-1}	Wavenumber[a], cm^{-1}	Intensity, km mol^{-1}	Wavenumber[a], cm^{-1}	Intensity, km mol^{-1}
712.69	35.86	730.95	42.45	687.90	68.30
784.06	47.22	768.36	1.16	773.68	105.12
820.56	78.44	818.40	205.12	814.60	23.45
874.41	16.19	879.71	6.74	891.10	4.91
957.95	3.38	962.17	23.88	964.80	6.92
1039.21	51.09	988.14	74.10	1068.14	32.47
1062.02	24.34	1078.38	102.51	1105.67	152.12
1104.53	106.35	1086.75	23.65	1175.43	138.80
1199.70	111.98	1196.50	134.03	1246.80	9.86
1239.40	1.45	1277.22	0.37	1286.43	1.36
1307.48	2.69	1286.01	0.16	1315.59	14.67
1314.35	8.91	1344.01	64.16	1385.73	47.92
1343.06	55.52	1366.88	21.93	1396.38	11.89
1399.50	17.85	1373.17	0.24	1446.70	10.93
1458.18	7.86	1458.67	6.12	1483.57	7.79
1497.65	2.19	1482.49	3.52	1634.28	24.46
1633.41	25.83	1638.27	22.95	2836.03	76.69
1778.30	351.34	1788.25	317.20	2944.27	11.28
2827.61	57.73	2994.17	12.11	2938.99	1.19
2918.29	7.28	3009.84	23.71	2956.37	21.37
2936.50	8.63	3028.95	8.06	3345.16	0.68
2970.55	15.09	3065.77	20.36	3423.24	3.64
3338.90	0.53	3227.13	0.90	3562.15	56.76
3413.21	2.94	3396.98	0.66		
3568.53	64.57	3575.77	57.67		

[a] A scaling factor of 0.955 was employed for vibrational modes with wavenumbers greater than 2000 cm^{-1}, and a scaling factor of 0.985 was employed for all other vibrational modes.

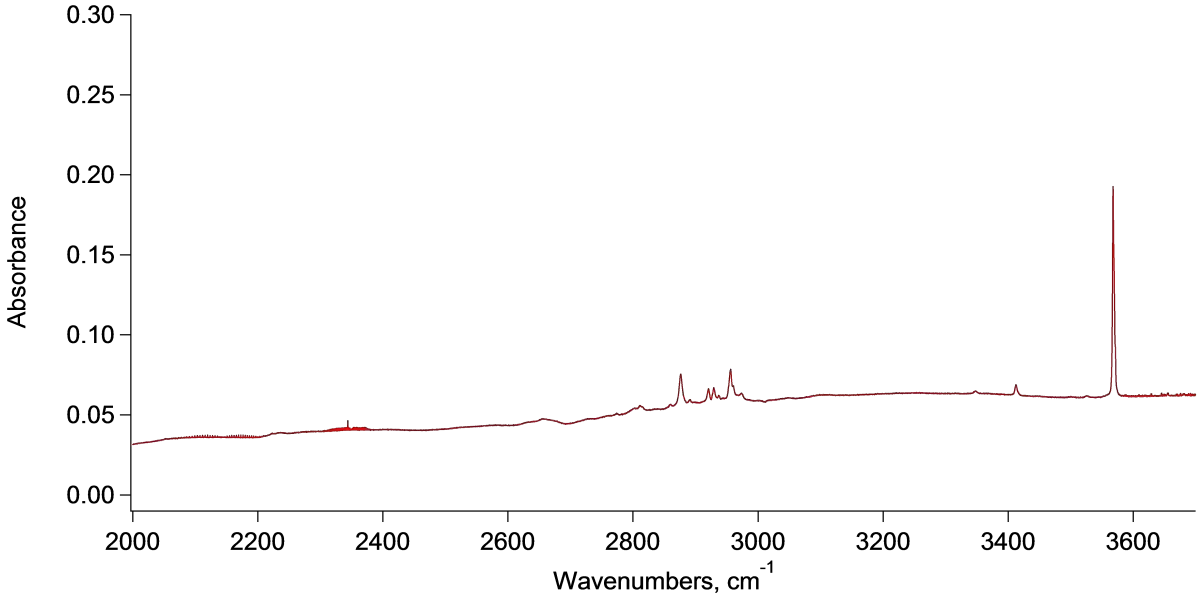

Figure A.2: The 2000 - 3700 cm^{-1} region of the FTIR spectrum of β-alanine sublimed at a temperature of 390 K and trapped into a parahydrogen matrix observed immediately after deposition.

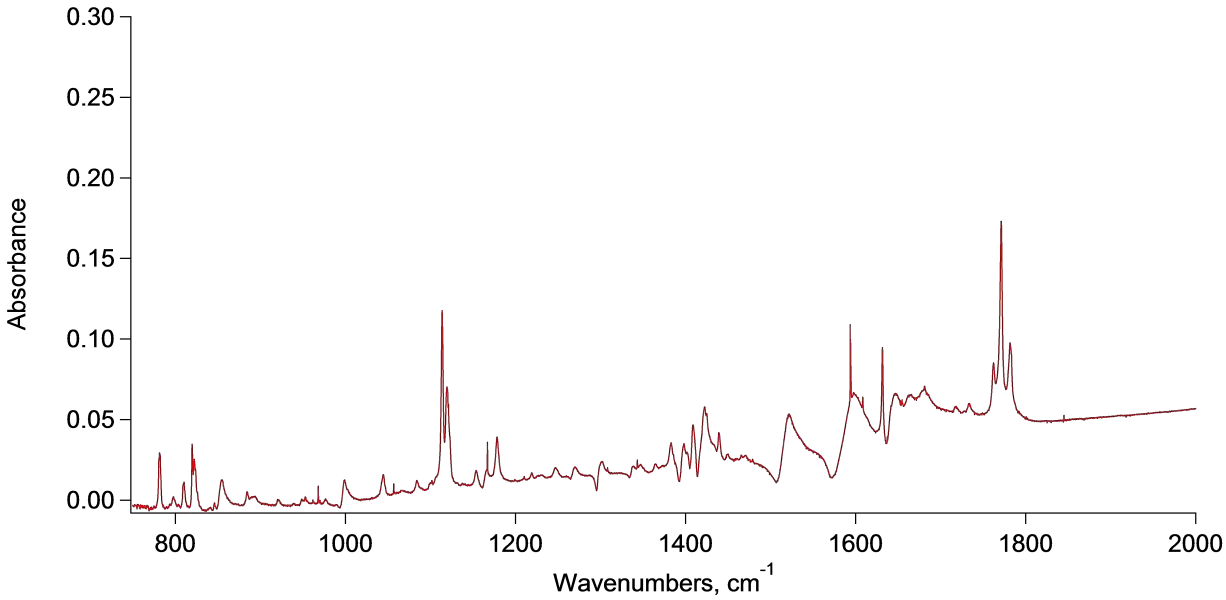

Figure A.3: The 750 - 2000 cm^{-1} region of the FTIR spectrum of β-alanine in solid parahydrogen recorded after 4 hrs of UV-irradiation of the sample shown in Figures A.1 and A.2

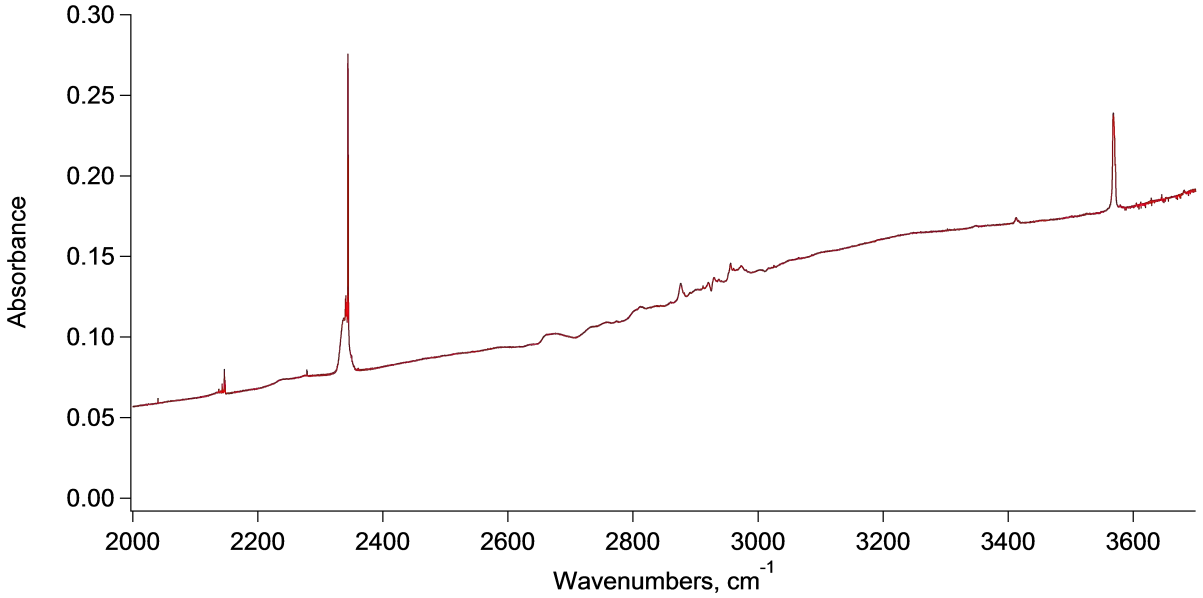

Figure A.4: The 2000 - 3700 cm^{-1} region of the FTIR spectrum of β-alanine in solid parahydrogen recorded after 4 hrs of UV-irradiation of the sample shown in Figures A.1 and A.2

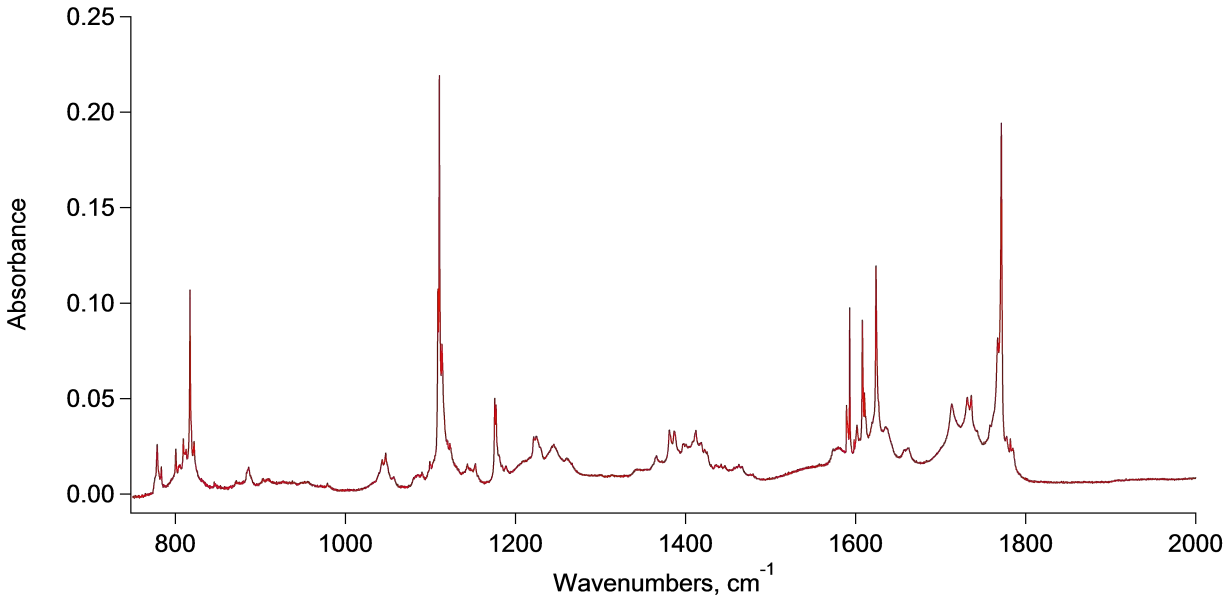

Figure A.5: The 750 - 2000 cm^{-1} region of the FTIR spectrum of β-alanine sublimed at a temperature of 390 K and trapped into an argon matrix observed immediately after deposition.

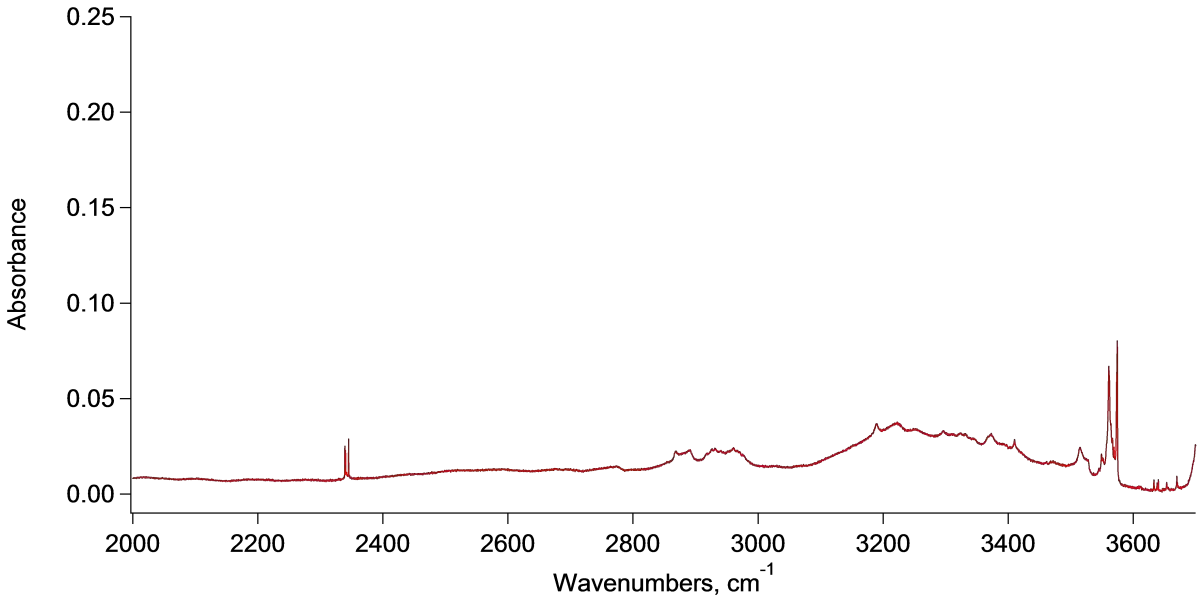

Figure A.6: The 2000 - 3700 cm^{-1} region of the FTIR spectrum of β-alanine sublimed at a temperature of 390 K and trapped into an argon matrix observed immediately after deposition.

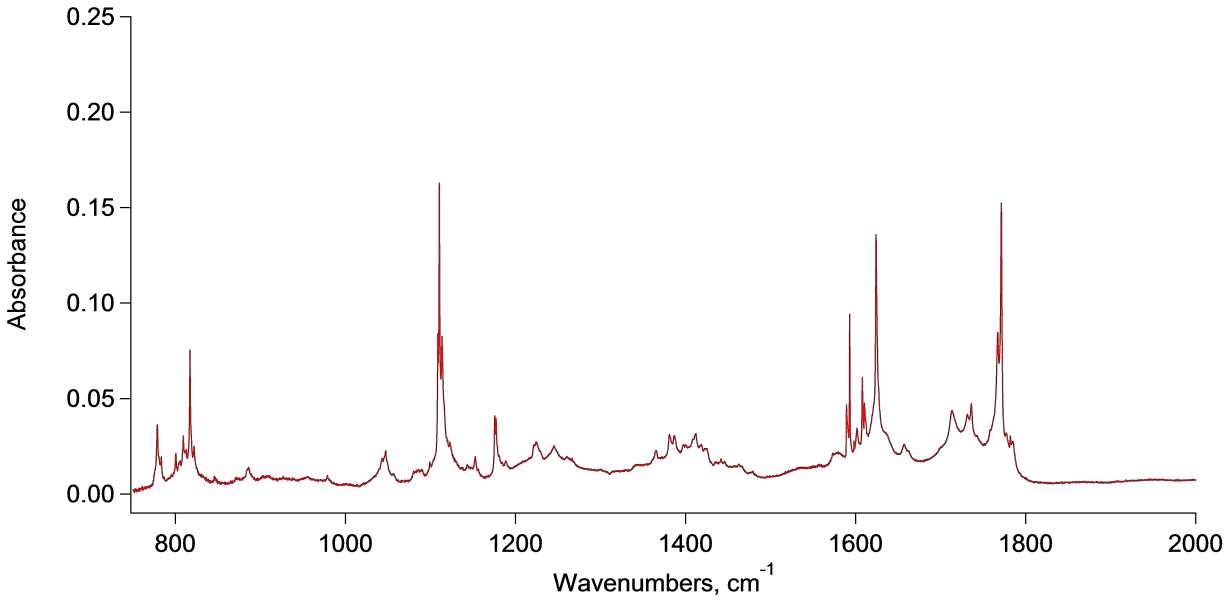

Figure A.7: The 750 - 2000 cm^{-1} region of the FTIR spectrum of β-alanine in solid argon recorded after 4 hrs of UV-irradiation of the sample shown in Figures A.5 and A.6

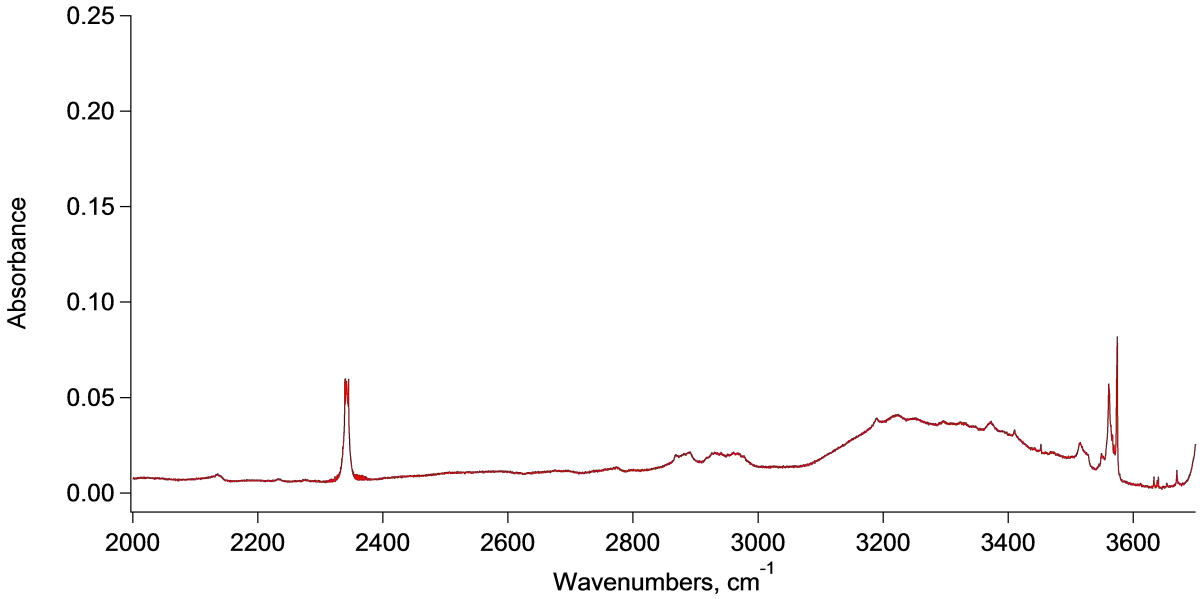

Figure A.8: The 2000 - 3700 cm^{-1} region of the FTIR spectrum of β-alanine in solid argon recorded after 4 hrs of UV-irradiation of the sample shown in Figures A.5 and A.6

Appendix B

Supplementary Material: Conformational Analysis of Gaseous α-alanine in Solid Parahydrogen and Argon Matrices

The following presents raw data from the α-alanine conformational studies discussed in Section 5.2. These include full FTIR spectra taken for each procedure, and tables of theoretically calculated wavenumbers and associated intensities tabulated for each α-alanine conformer candidate.

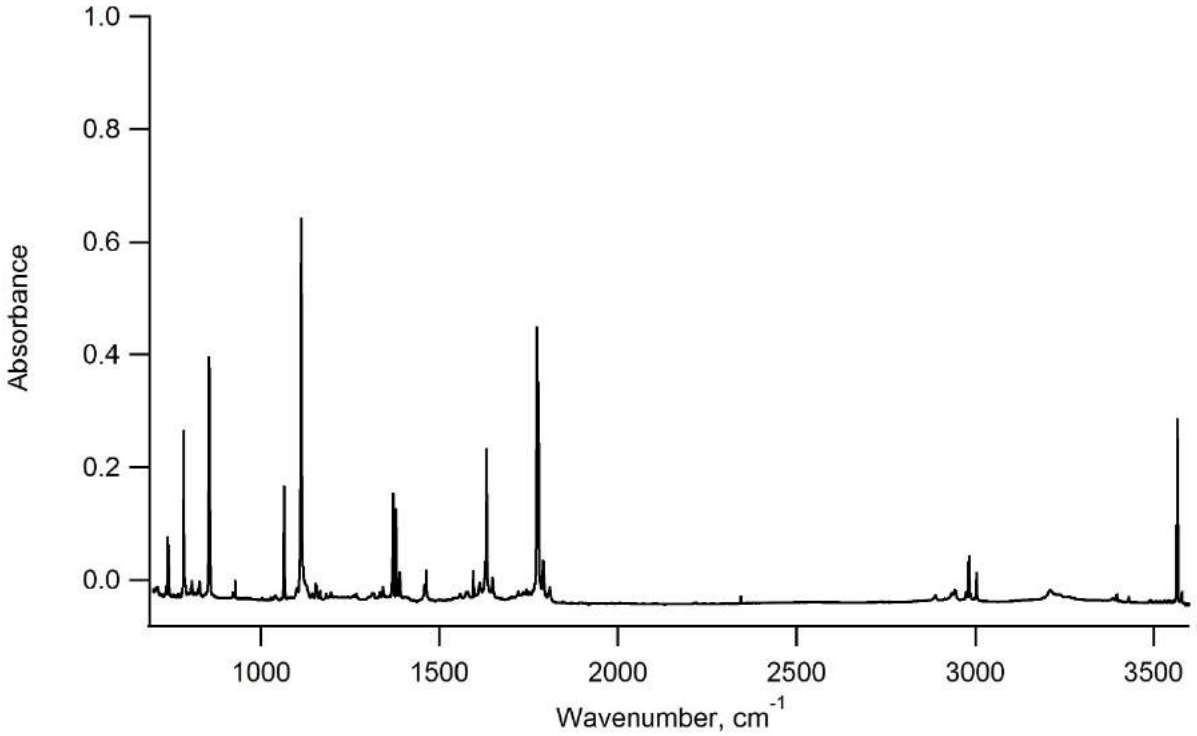

Figure B.1: The solid parahydrogen matrix isolation FTIR spectrum of α-alanine (T_{sub} = 420 K, deposition time = 30 min, flow rate = 5 ccm, T_{dep} = 4 K) measured immediately after deposition.

Table B.1: Theoretical wavenumbers (cm^{-1}) and intensities ($km \cdot mol^{-1}$) of the eight α-alanine conformers (Conformer I to VIII) calculated at the B3LYP/aug − cc − pVTZ level of theory in the region of 700 - 4800 cm^{-1}.

Conformer I		Conformer II		Conformer III		Conformer IV	
Wavenumber[a], cm^{-1}	Intensity, km mol^{-1}	Wavenumber[a], cm^{-1}	Intensity, km mol^{-1}	Wavenumber[a], cm^{-1}	Intensity, km mol^{-1}	Wavenumber[a], cm^{-1}	Intensity, km mol^{-1}
744.02	29.79	730.40	15.51	761.03	21.24	747.03	29.35
774.90	35.24	786.06	9.73	764.34	40.36	779.30	48.98
870.49	133.74	827.32	73.06	844.49	133.05	823.21	134.60
908.03	1.09	850.93	72.73	903.55	4.58	902.56	7.98
1055.90	1.63	923.42	37.55	1002.80	4.91	1016.52	5.99
1068.16	24.02	997.62	0.98	1028.33	117.20	1063.64	14.26
1106.11	286.03	1040.57	32.00	1120.46	16.30	1119.12	281.01
1147.36	17.27	1110.45	13.24	1161.85	137.00	1152.83	2.34
1254.69	1.18	1182.96	19.62	1247.51	5.70	1214.07	24.36
1274.48	2.77	1250.44	4.02	1309.18	5.38	1294.77	11.67
1333.19	16.93	1312.88	10.03	1324.27	29.19	1331.87	11.98
1379.82	0.51	1339.65	37.83	1378.41	6.56	1378.48	2.41
1394.79	8.19	1379.99	278.79	1387.22	8.22	1409.38	17.03
1472.56	7.30	1390.27	76.17	1471.04	8.15	1471.55	6.76
1477.56	6.95	1475.91	4.99	1476.65	3.26	1480.60	10.18
1644.88	23.27	1479.38	7.51	1638.17	30.37	1613.19	61.42
1775.86	295.48	1632.53	33.23	1772.61	315.89	1781.37	279.07
2901.81	11.25	1804.04	335.67	2903.02	12.94	2894.46	16.77
2916.31	12.85	2897.22	11.37	2936.12	5.03	2904.85	13.89
2966.71	20.99	2902.08	20.27	2967.39	23.17	2959.35	20.26
2985.96	11.89	2955.02	22.38	2979.34	12.26	2965.17	23.45
3338.48	1.67	2989.42	9.12	3344.37	1.72	3345.71	6.09
3407.16	4.57	3322.60	247.63	3418.75	4.92	3426.81	9.93
3565.36	56.11	3361.10	1.38	3573.80	67.99	3570.01	67.20
		3434.14	10.97				

Table B.1 Continued

Conformer V		Conformer VI		Conformer VII		Conformer VIII	
Wavenumber[a], cm^{-1}	Intensity, km mol^{-1}	Wavenumber[a], cm^{-1}	Intensity, km mol^{-1}	Wavenumber[a], cm^{-1}	Intensity, km mol^{-1}	Wavenumber[a], cm^{-1}	Intensity, km mol^{-1}
722.87	64.47	731.29	0.69	725.59	5.88	715.84	6.87
782.68	67.43	780.30	11.18	782.26	14.51	787.77	33.72
838.66	54.24	877.07	144.16	905.93	3.98	817.17	113.23
921.67	6.59	903.83	1.24	978.27	0.53	914.45	2.40
1007.38	0.89	1003.13	1.60	1039.13	35.53	1006.91	1.16
1073.79	20.44	1064.78	35.76	1123.78	15.27	1088.07	5.34
1117.69	228.38	1102.54	58.67	1162.02	12.99	1120.67	50.79
1143.30	75.75	1147.06	6.80	1224.39	12.54	1155.45	1.88
1236.43	1.34	1247.16	194.08	1297.63	186.34	1206.88	3.63
1293.44	16.33	1263.90	101.28	1302.34	169.04	1270.35	355.99
1324.34	20.69	1311.68	60.08	1356.07	10.63	1329.36	9.69
1391.80	27.68	1387.04	1.90	1387.37	13.19	1371.55	19.53
1399.89	0.42	1396.17	5.51	1475.65	8.76	1396.41	4.51
1468.12	8.41	1466.57	6.67	1476.28	2.39	1465.83	11.39
1475.65	3.13	1479.21	8.76	1614.34	27.98	1483.47	11.57
1625.11	36.55	1646.28	25.75	1802.65	274.84	1609.74	54.96
1785.74	291.51	1808.37	249.97	2896.05	12.21	1804.66	267.49
2784.97	47.00	2874.68	22.85	2914.10	13.93	2789.21	41.67
2907.90	19.31	2902.28	13.60	2963.76	19.66	2884.96	29.16
2968.05	17.47	2960.73	23.98	2996.60	6.57	2947.85	25.02
2989.82	12.58	2980.80	11.88	3386.22	7.73	2976.93	12.14
3352.25	1.36	3337.02	2.88	3487.63	12.43	3354.67	10.46
429.59	5.74	3404.42	5.66	3538.99	87.77	3438.02	16.98
374.69	66.80	3618.03	41.08			3622.53	51.68

[a] A scaling factor of 0.955 was employed for vibrational modes with wavenumbers greater than 2000 cm^{-1}, and a scaling factor of 0.985 was employed for all other vibrational modes.

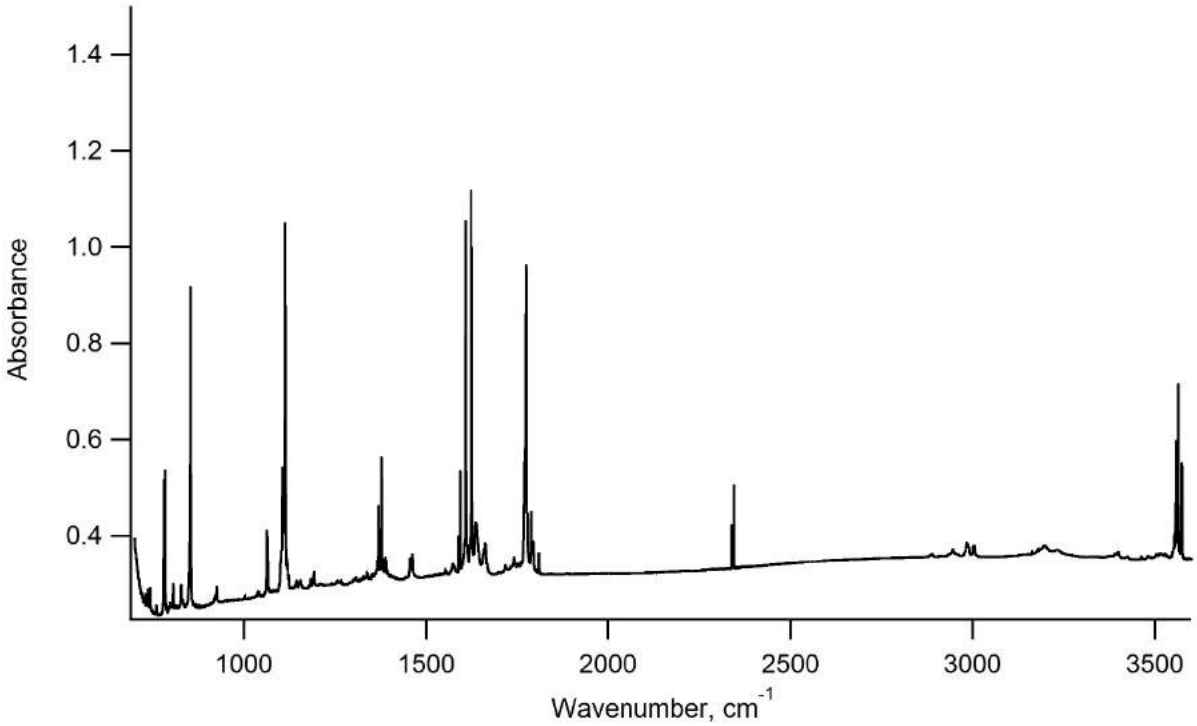

Figure B.2: The solid argon matrix isolation FTIR spectrum of α-alanine (T_{sub} = 420 K, deposition time = 30 min, flow rate = 5 ccm, T_{dep} = 18 K) measured immediately after deposition.

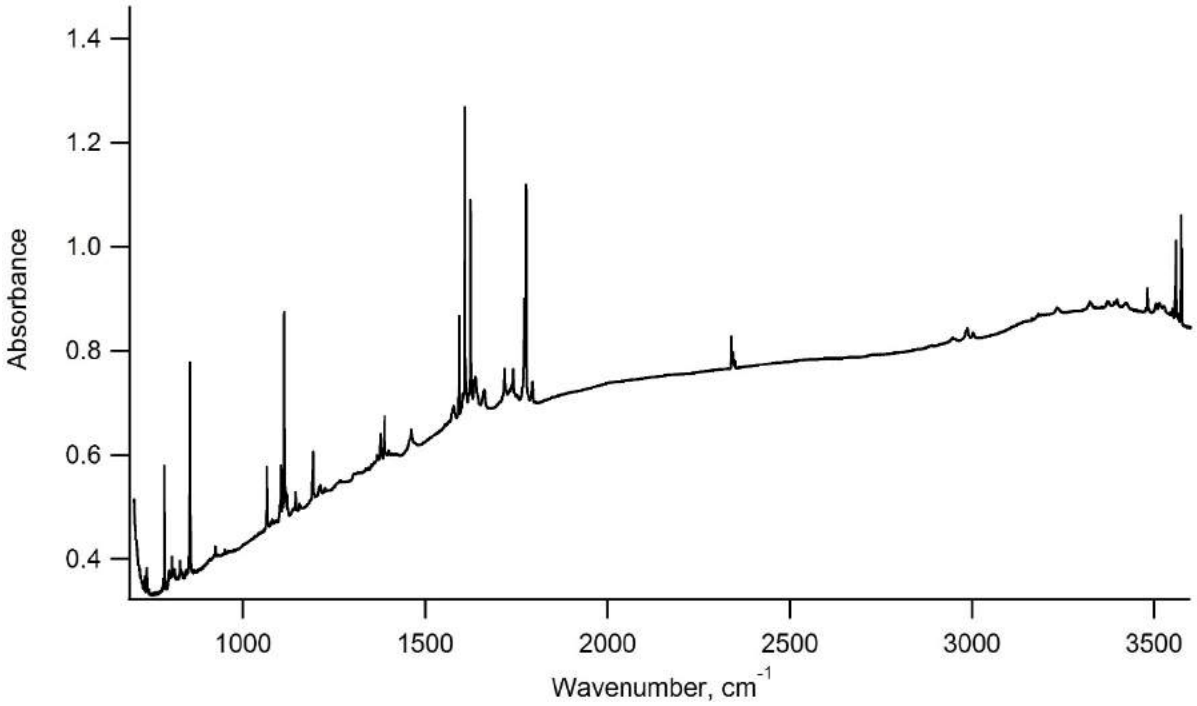

Figure B.3: FTIR spectrum of α-alanine isolated in an argon matrix (T_{sub} = 420 K, deposition time = 30 min, flow rate = 5 ccm, T_{dep} = 18 K) recorded immediately after annealing (10 min, 40 K).

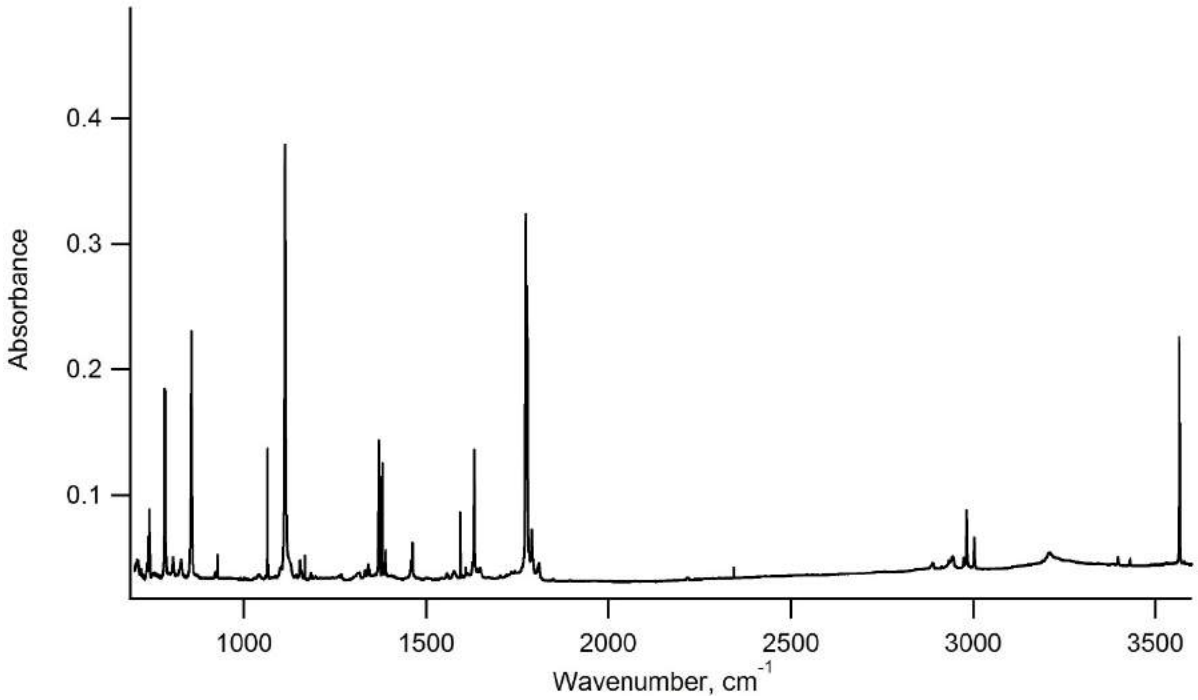

Figure B.4: FTIR spectrum of α-alanine sublimed at a temperature of 410 K and isolated in a parahydrogen matrix (deposition time = 30 min, flow rate = 5 ccm, T_{dep} = 4 K).

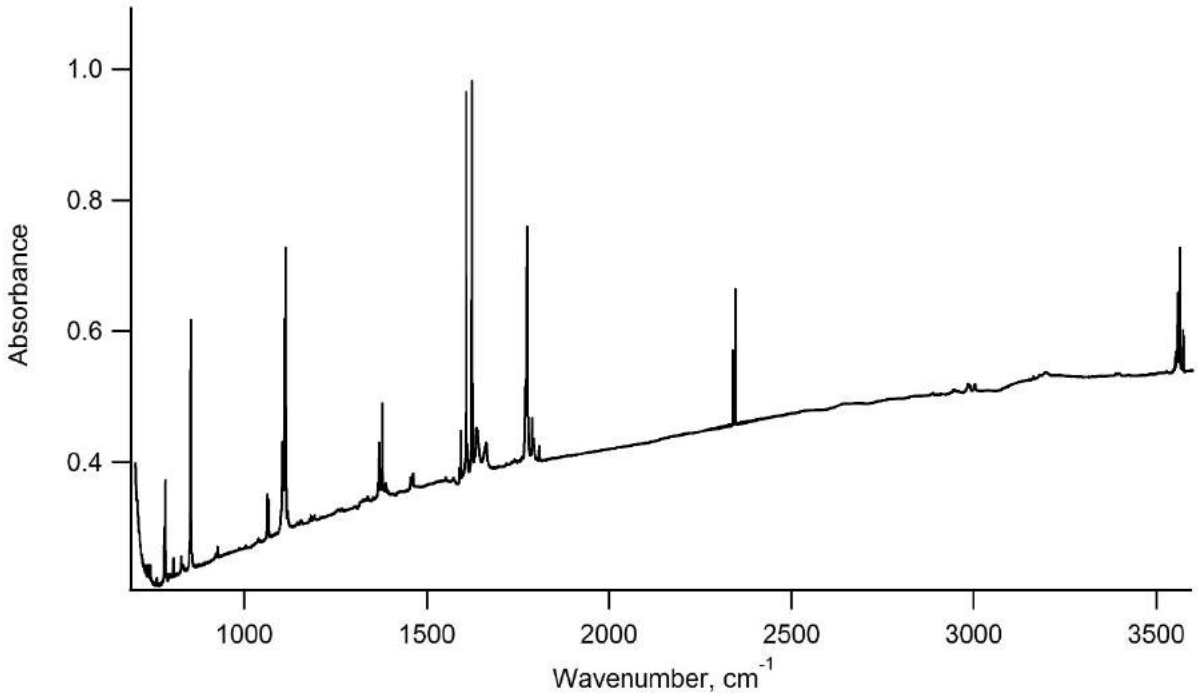

Figure B.5: FTIR spectrum of α-alanine sublimed at a temperature of 410 K and isolated in an argon matrix (deposition time = 30 min, flow rate = 5 ccm, T_{dep} = 18 K).

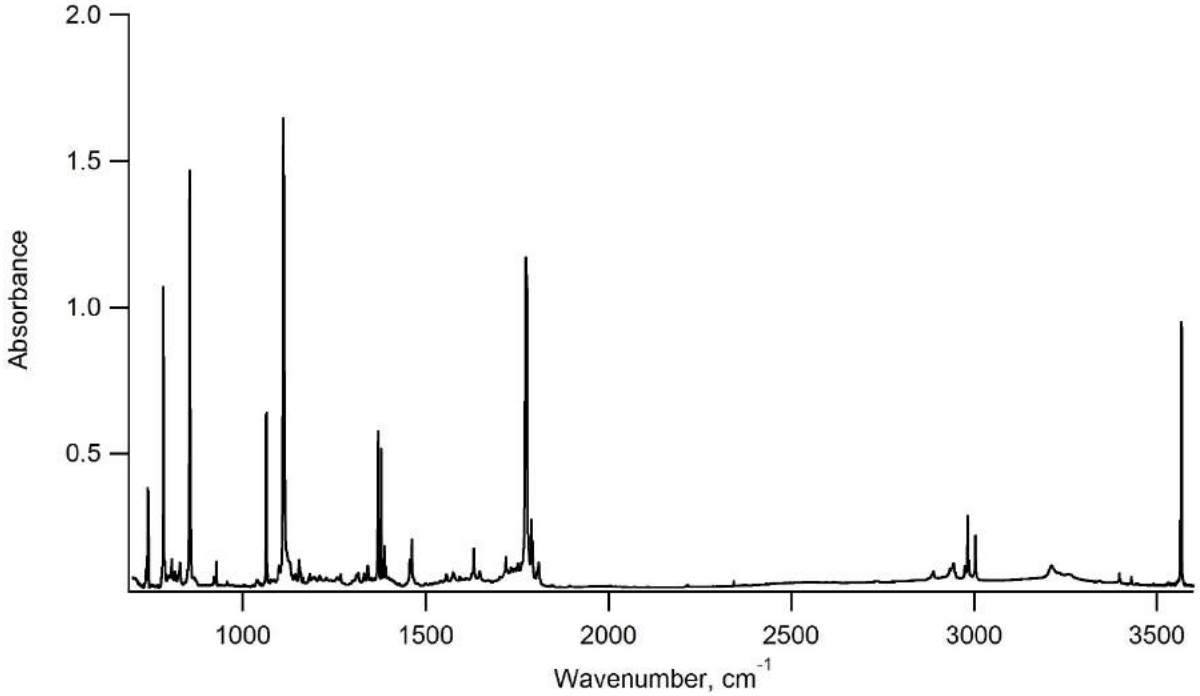

Figure B.6: FTIR spectrum of α-alanine sublimed at a temperature of 430 K and isolated in a parahydrogen matrix (deposition time = 30 min, flow rate = 5 ccm, T_{dep} = 4 K).

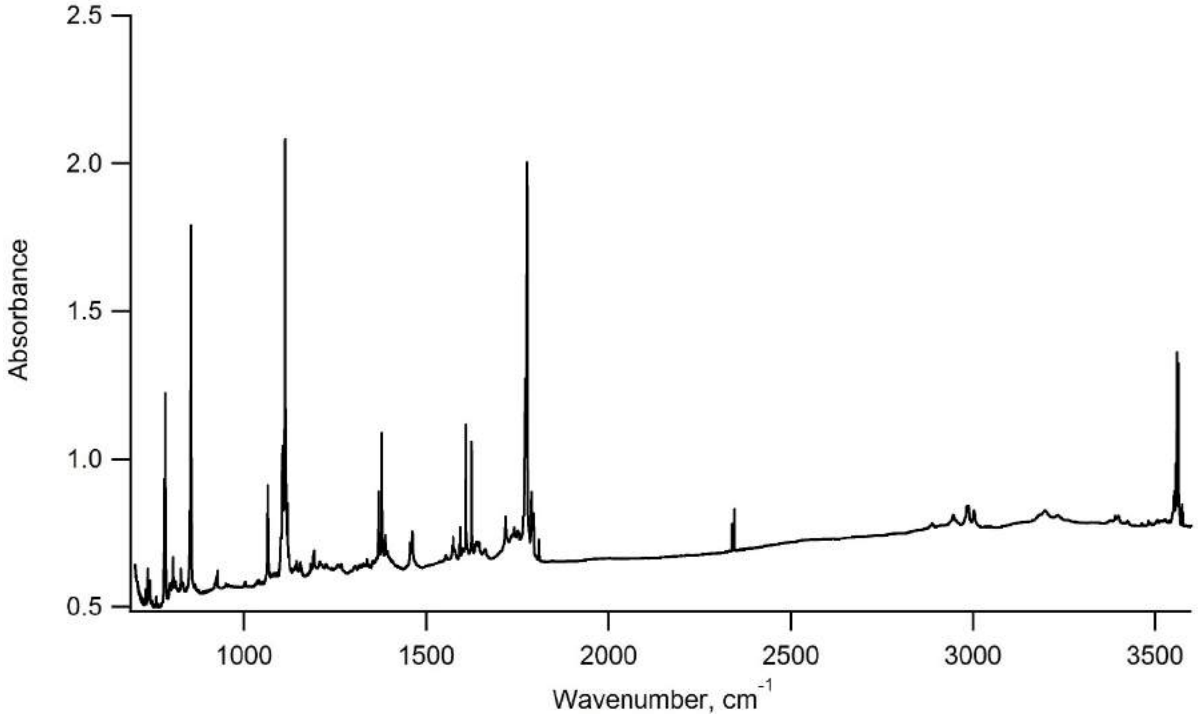

Figure B.7: FTIR spectrum of α-alanine sublimed at a temperature of 430 K and isolated in an argon matrix (deposition time = 30 min, flow rate = 5 ccm, T_{dep} = 18 K).

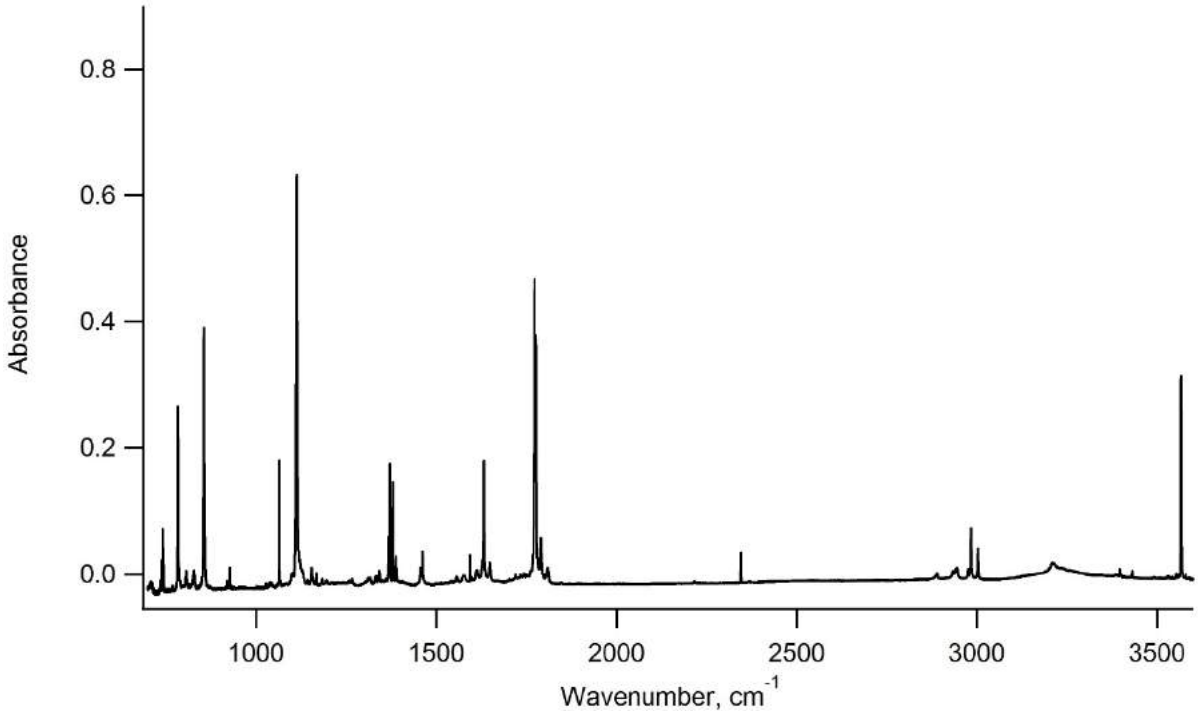

Figure B.8: FTIR spectrum of α-alanine trapped in a parahydrogen matrix recorded immediately after deposition and before UV-irradiation (deposition time = 30 min, flow rate = 5 ccm, T_{sub} = 420 K, T_{dep} = 4 K).

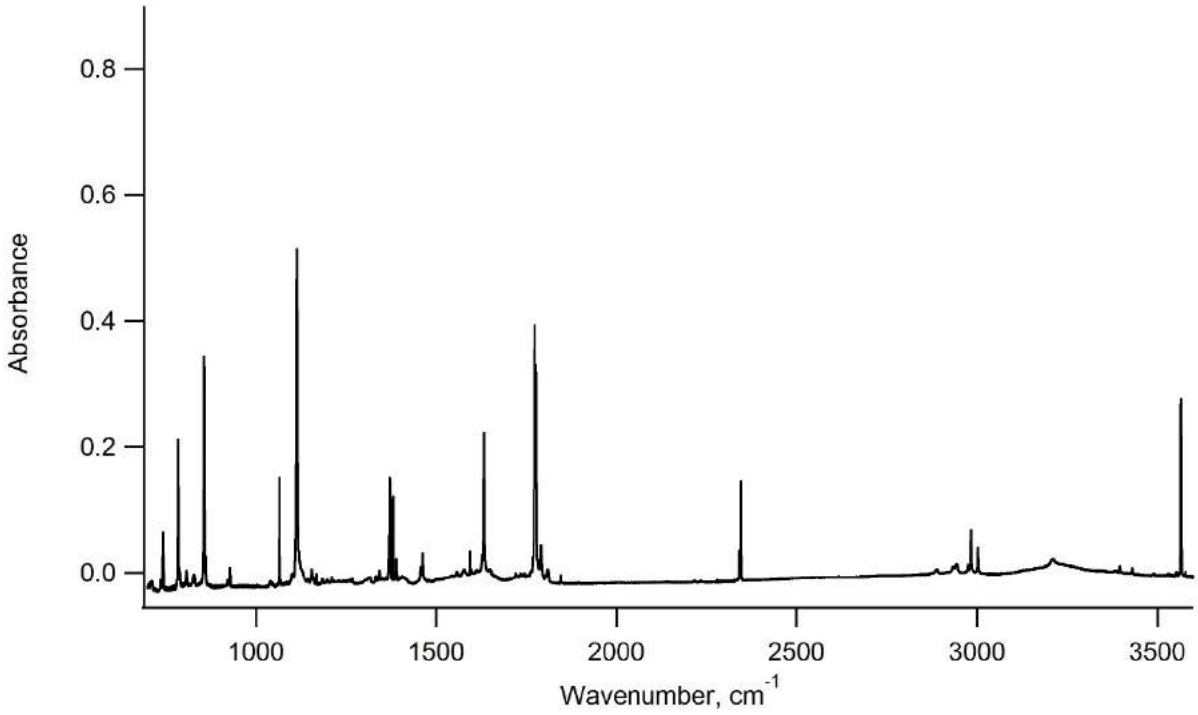

Figure B.9: Solid parahydrogen matrix isolation spectrum of α-alanine measured after 1 hr of UV-irradiation (deposition time = 30 min, flow rate = 5 ccm, T_{sub} = 420 K, T_{dep} = 4 K).

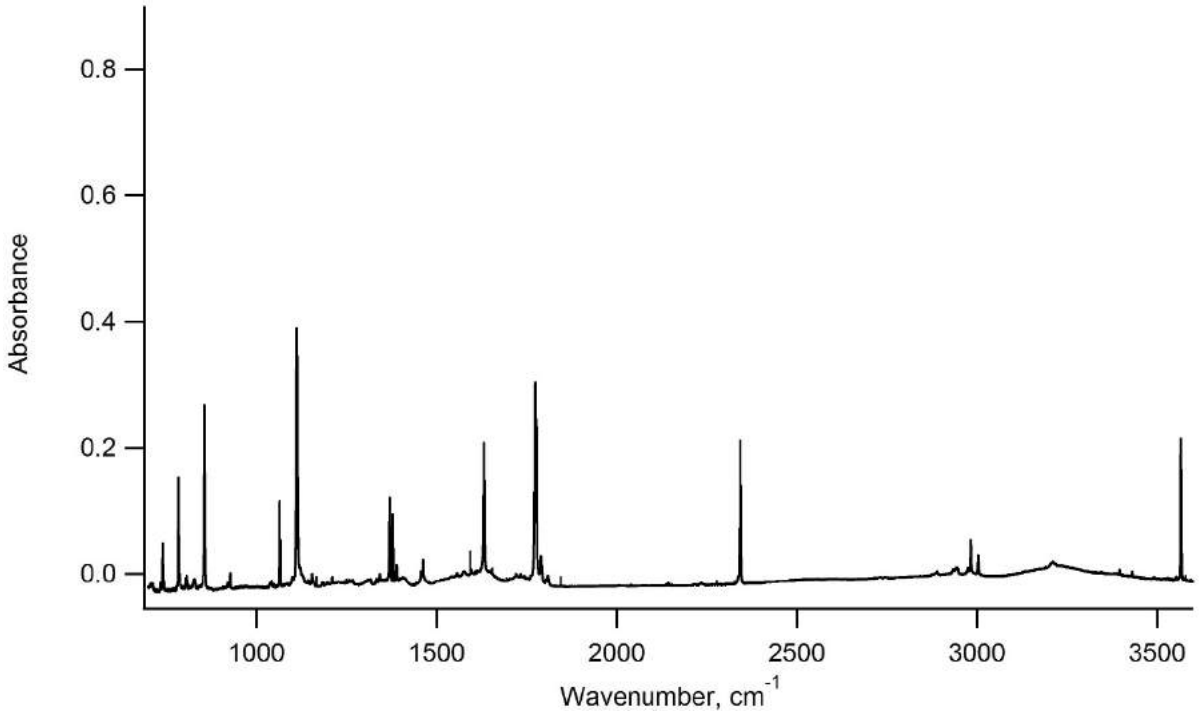

Figure B.10: Solid parahydrogen matrix isolation spectrum of α-alanine measured after 2 hrs of UV-irradiation (deposition time = 30 min, flow rate = 5 ccm, T_{sub} = 420 K, T_{dep} = 4 K).

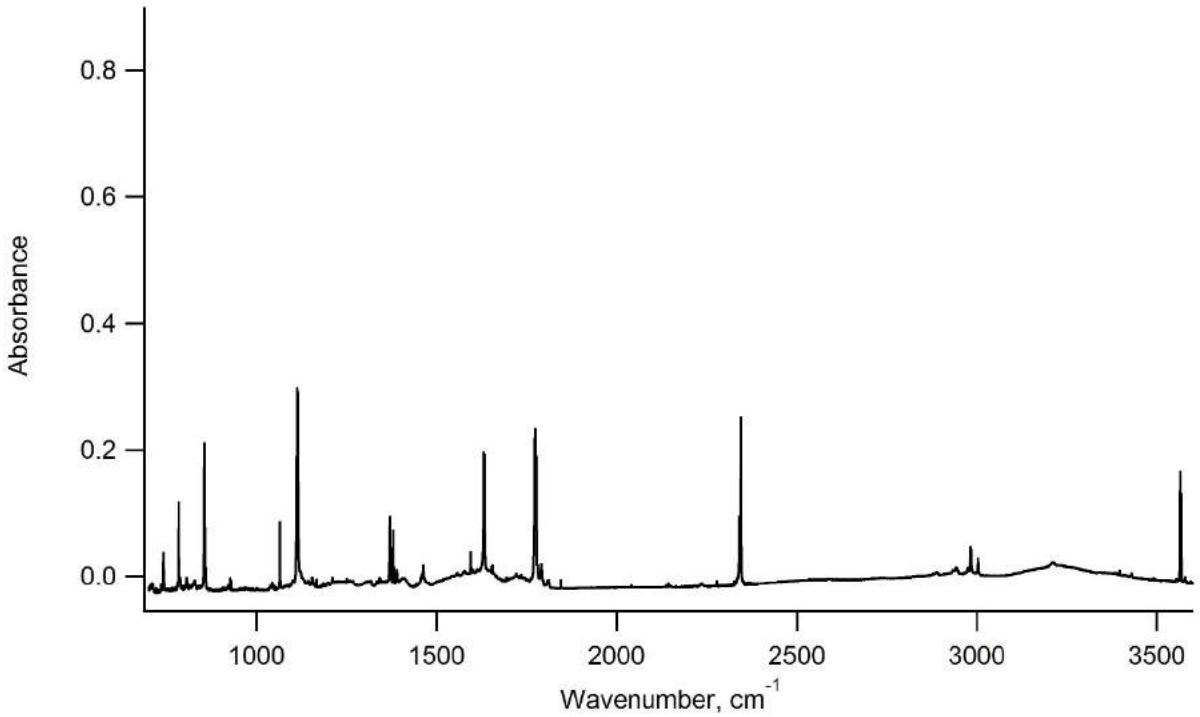

Figure B.11: Solid parahydrogen matrix isolation spectrum of α-alanine measured after 3 hrs of UV-irradiation (deposition time = 30 min, flow rate = 5 ccm, T_{sub} = 420 K, T_{dep} = 4 K).

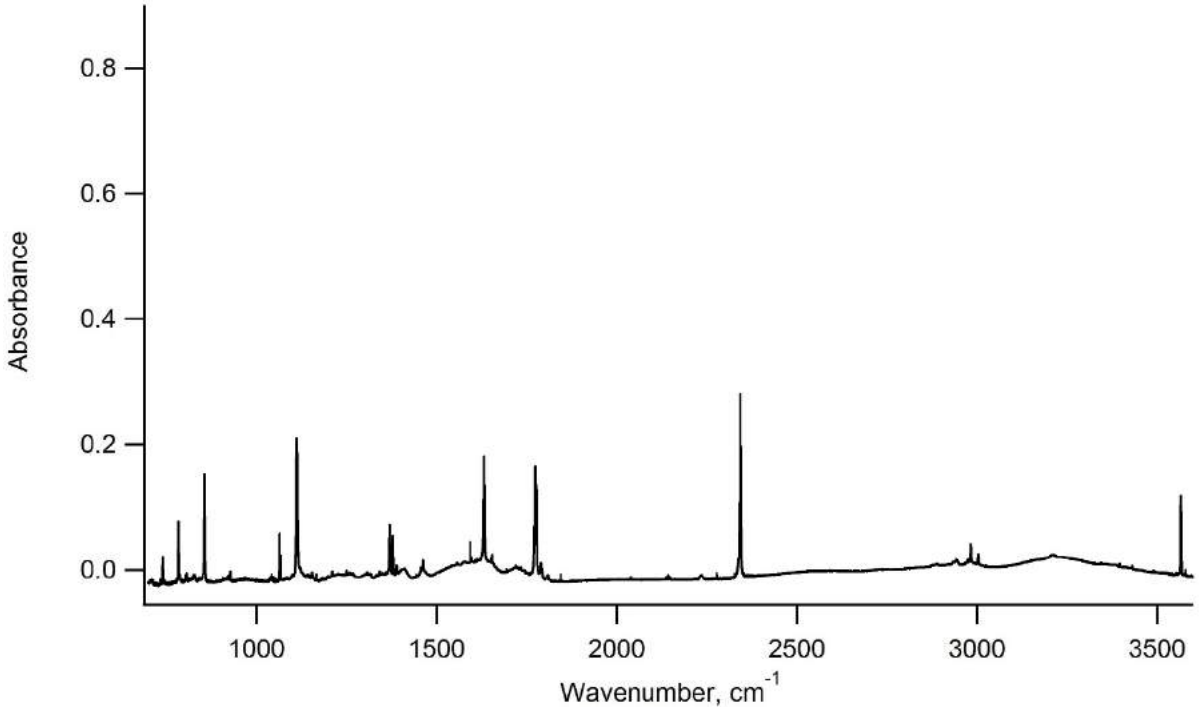

Figure B.12: Solid parahydrogen matrix isolation spectrum of α-alanine measured after 4 hrs of UV-irradiation (deposition time = 30 min, flow rate = 5 ccm, T_{sub} = 420 K, T_{dep} = 4 K).

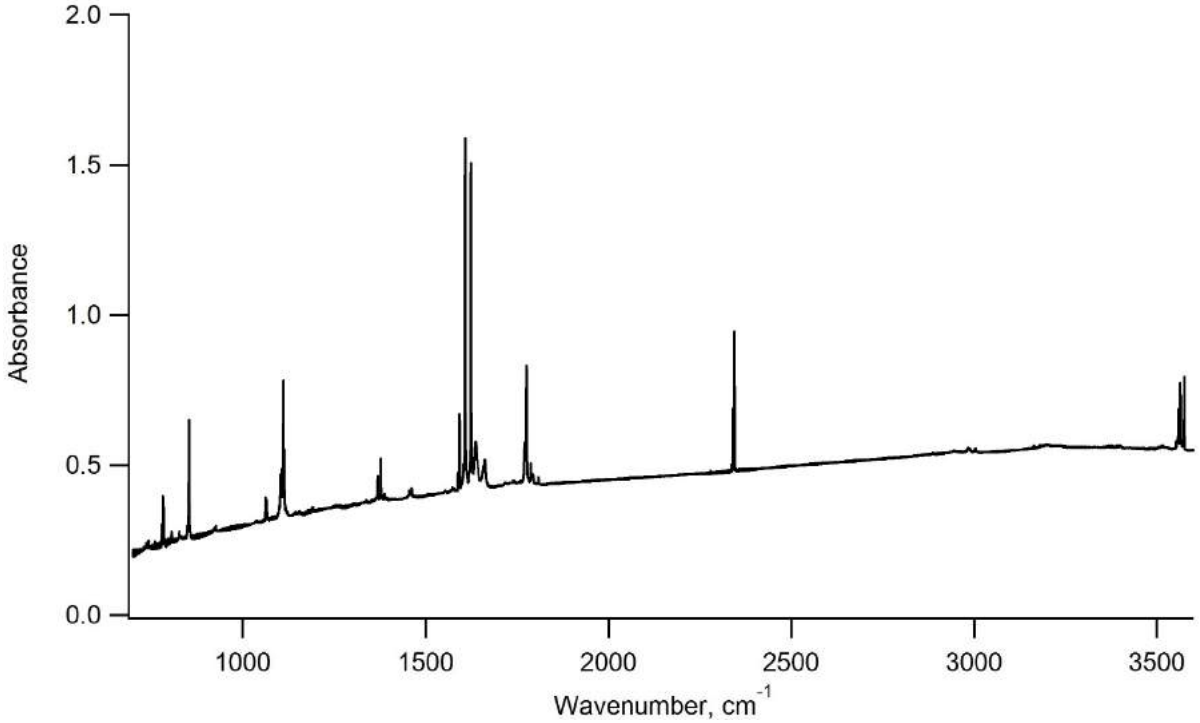

Figure B.13: FTIR spectrum of α-alanine trapped in an argon matrix recorded immediately after deposition and before UV-irradiation (deposition time = 30 min, flow rate = 5 ccm, T_{sub} = 420 K, T_{dep} = 18 K).

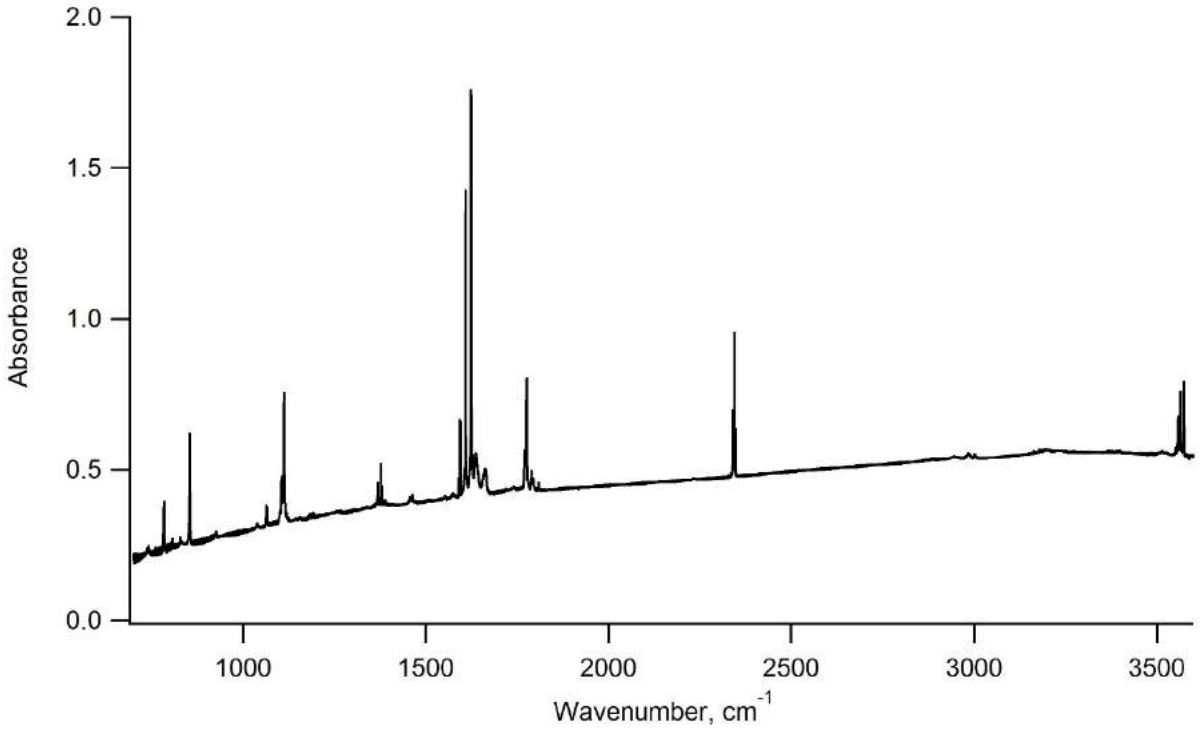

Figure B.14: Solid argon matrix isolation spectrum of α-alanine measured after 1 hr of UV-irradiation (deposition time = 30 min, flow rate = 5 ccm, T_{sub} = 420 K, T_{dep} = 18 K).

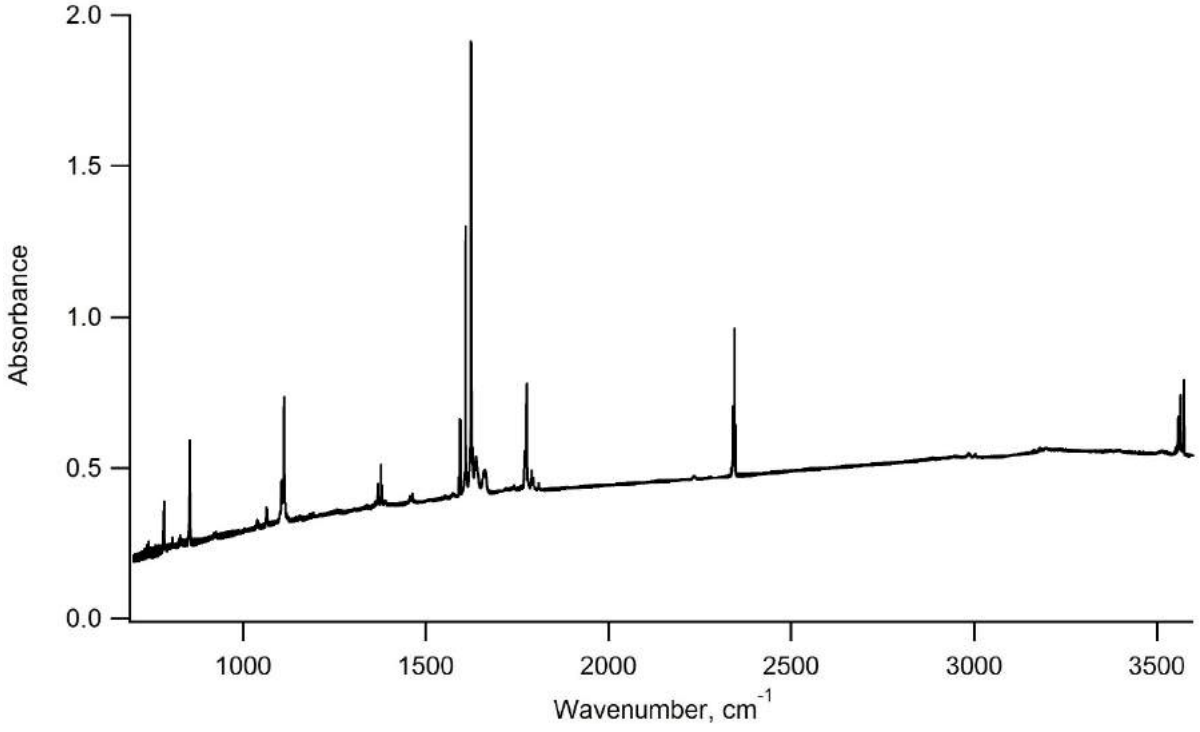

Figure B.15: Solid argon matrix isolation spectrum of α-alanine measured after 2 hrs of UV-irradiation (deposition time = 30 min, flow rate = 5 ccm, T_{sub} = 420 K, T_{dep} = 18 K).

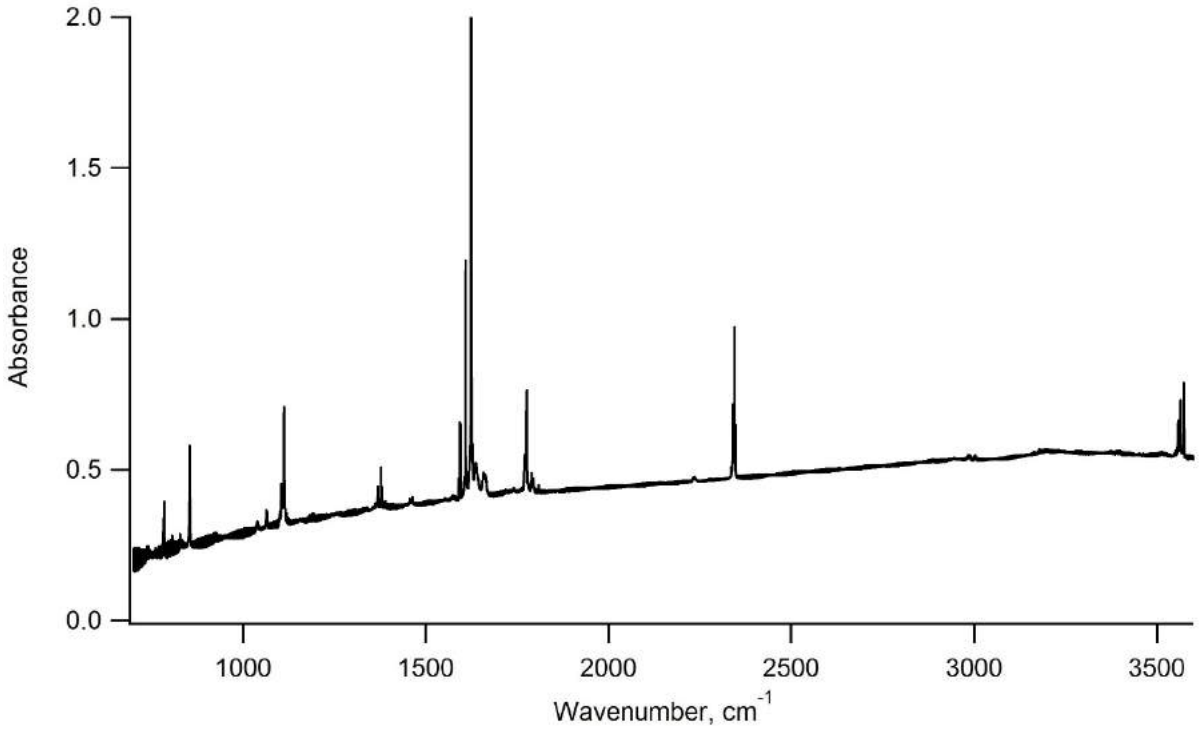

Figure B.16: Solid argon matrix isolation spectrum of α-alanine measured after 3 hrs of UV-irradiation (deposition time = 30 min, flow rate = 5 ccm, T_{sub} = 420 K, T_{dep} = 18 K).

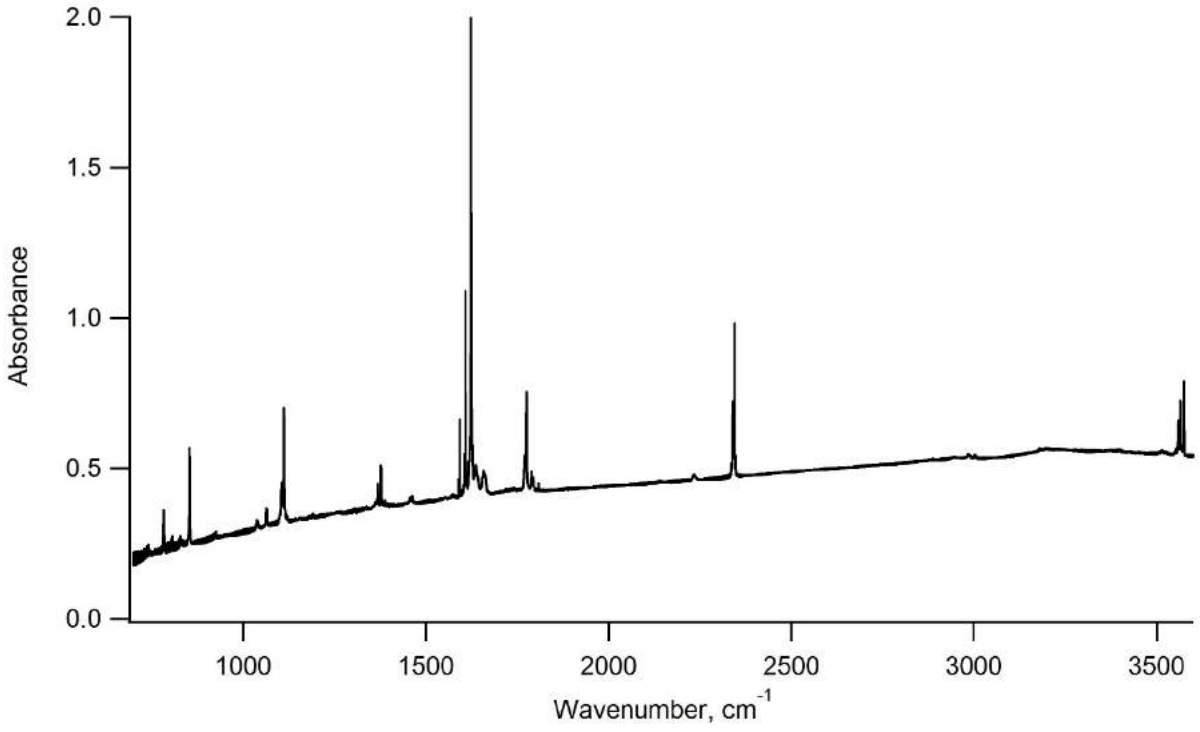

Figure B.17: Solid argon matrix isolation spectrum of α-alanine measured after 4 hrs of UV-irradiation (deposition time = 30 min, flow rate = 5 ccm, T_{sub} = 420 K, T_{dep} = 18 K).

Appendix C

Supplementary Material: UV Photolysis of Deuterated α-alanine in Solid Parahydrogen

The following presents raw data from the deuterated α-alanine UV photolysis studies discussed in Section 5.3. These include full FTIR spectra taken for each procedure, and tables of theoretically calculated wavenumbers and associated intensities tabulated for each deuterated α-alanine conformer candidate and also for each photoproduct candidate.

Table C.1: Theoretical wavenumbers (cm^{-1}) and intensities ($km \cdot mol^{-1}$) of the twelve deuterated α-alanine conformers (Conformer I to VIII: considering both L- and D- form with labels "A" and "B", respectively) calculated at the B3LYP/aug − cc − pVTZ level of theory in the region of 700 - 4800 cm^{-1}.

Conformer I		Conformer IIA		Conformer IIB		Conformer IIIA	
Wavenumber[a], cm^{-1}	Intensity, $km\ mol^{-1}$	Wavenumber[a], cm^{-1}	Intensity, $km\ mol^{-1}$	Wavenumber[a], cm^{-1}	Intensity, $km\ mol^{-1}$	Wavenumber[a], cm^{-1}	Intensity, $km\ mol^{-1}$
718.20	25.07	724.06	16.83	724.06	16.83	731.58	12.52
755.63	8.01	757.12	5.79	757.12	5.79	760.96	17.67
833.36	108.29	824.46	77.23	824.46	77.23	812.82	110.27
861.64	1.96	850.80	31.99	850.80	31.98	846.64	37.48
915.78	38.46	859.23	48.27	859.23	48.28	900.60	33.69
936.41	8.89	901.69	25.93	901.69	25.93	934.34	3.27
1041.39	110.26	931.31	8.49	931.31	8.49	1052.08	2.95
1053.71	5.72	1037.39	9.34	1037.39	9.34	1053.84	16.18
1058.53	0.72	1055.33	6.98	1055.33	6.98	1056.67	18.47
1089.79	98.97	1059.33	3.28	1059.33	3.28	1109.54	30.07
1131.89	87.60	1091.67	0.99	1091.67	0.99	1140.34	175.21
1191.82	25.86	1140.22	20.25	1140.22	20.25	1156.09	29.07
1275.10	2.52	1193.52	42.82	1193.52	42.82	1268.21	6.59
1312.68	28.84	1261.60	3.21	1261.60	3.21	1311.45	28.46
1635.00	22.54	1373.04	375.43	1373.04	375.43	1628.26	29.43
1765.27	299.38	1622.90	35.19	1622.90	35.19	1761.54	318.67
2137.65	7.05	1793.64	337.01	1793.64	337.01	2137.04	6.23
2200.92	5.98	2134.60	8.27	2134.60	8.27	2218.84	4.30
2251.42	10.38	2190.26	9.68	2190.26	9.68	2252.57	11.14
2269.20	5.18	2244.65	10.78	2244.65	10.77	2263.76	5.23
3317.47	1.75	2269.58	3.37	2269.58	3.37	3323.32	1.78
3385.69	4.71	3301.70	246.89	3301.69	246.89	3397.19	5.08
3542.98	56.16	3339.96	1.40	3339.96	1.40	3551.37	68.02
		3412.55	11.08	3412.55	11.08		

Table C.1 Continued

Conformer IVA		Conformer IVB		Conformer VA		Conformer VB	
Wavenumber[a], cm^{-1}	Intensity, km mol^{-1}	Wavenumber[a], cm^{-1}	Intensity, km mol^{-1}	Wavenumber[a], cm^{-1}	Intensity, km mol^{-1}	Wavenumber[a], cm^{-1}	Intensity, km mol^{-1}
714.69	18.87	707.60	42.22	704.16	42.45	719.29	37.51
759.96	23.07	756.69	37.88	748.12	44.48	762.04	6.28
804.14	139.85	809.92	87.42	826.11	53.08	799.45	105.11
863.30	21.47	868.42	3.05	866.59	0.39	848.02	48.57
921.02	7.72	920.86	11.11	923.56	14.81	906.59	10.09
941.83	9.62	951.84	7.24	960.50	17.27	934.11	7.94
1025.55	14.81	1015.67	13.78	1018.31	20.19	1044.56	4.04
1054.62	3.29	1052.64	3.46	1050.48	4.78	1052.97	8.66
1056.37	3.95	1056.36	4.43	1053.14	5.81	1056.09	4.17
1090.20	16.85	1089.61	20.47	1093.80	3.37	1106.37	16.52
1115.07	223.20	1121.63	255.93	112.12	277.51	1131.32	229.80
1188.91	56.43	1210.14	13.61	1179.75	29.33	1149.17	26.06
1266.51	4.82	1273.94	8.53	1281.80	8.93	1262.42	4.37
1349.84	40.58	1348.02	33.01	1351.39	29.51	1339.47	52.38
1603.15	61.72	1600.54	62.24	1614.35	38.62	1614.99	32.16
1770.62	282.22	1766.00	298.75	1775.88	291.48	1773.25	322.50
2129.75	7.55	2106.16	24.79	2096.55	28.36	2129.08	6.76
2192.72	9.31	2140.68	7.74	2142.67	7.59	2218.63	3.63
2248.07	8.91	2253.47	9.75	2253.49	10.05	2247.55	9.05
2252.61	11.11	2269.34	7.78	2271.22	6.06	2250.92	11.71
3324.63	6.25	3336.58	5.22	3331.19	1.34	3322.08	2.10
3405.28	9.97	3418.07	12.44	3408.07	5.74	3398.85	4.79
3547.59	67.25	3552.20	71.11	3552.25	66.89	3552.00	68.78

Table C.1 Continued

Conformer VI		Conformer VII		Conformer VIIIA		Conformer VIIIB	
Wavenumber[a], cm^{-1}	Intensity, km mol^{-1}	Wavenumber[a], cm^{-1}	Intensity, km mol^{-1}	Wavenumber[a], cm^{-1}	Intensity, km mol^{-1}	Wavenumber[a], cm^{-1}	Intensity, km mol^{-1}
721.21	6.31	723.1240	10.0681	716.04	3.79	717.20	7.61
759.59	4.43	762.9701	7.1751	768.11	7.38	761.63	49.09
838.42	70.48	854.9644	7.3802	804.36	160.55	813.49	81.28
863.45	20.00	888.3371	11.4419	855.82	3.89	865.34	3.40
915.37	38.81	932.9461	2.0126	932.15	0.59	920.67	8.85
938.91	8.70	1039.3015	8.4306	943.81	16.37	949.61	7.54
1035.54	92.11	1054.7570	7.6520	1016.52	8.95	1016.73	9.20
1048.42	4.59	1056.5206	4.1889	1052.11	3.89	1045.41	3.07
1058.63	0.87	1094.0580	2.3620	1056.04	3.13	1059.36	4.71
1091.52	16.07	1129.3218	11.3972	1091.52	4.75	1094.89	1.60
1140.31	2.09	1172.9743	28.2068	1121.28	44.72	1130.29	39.18
1187.61	33.75	1226.8538	21.9011	1182.87	22.80	1199.92	67.86
1266.84	310.55	1294.4682	358.7570	1251.29	256.87	1258.30	201.68
1277.82	20.19	1604.5146	27.4477	1317.80	124.22	1316.58	132.88
1636.38	25.12	1792.4217	277.3595	1603.69	58.48	1599.94	56.57
1797.73	253.30	2136.4074	7.9291	1800.53	238.30	1795.28	267.93
2136.76	6.14	2198.0830	5.4371	2128.40	7.17	2100.15	24.82
2169.88	14.42	2247.3067	10.6453	2146.84	25.62	2128.98	11.12
2248.47	11.59	2276.9671	3.2476	2241.27	12.61	2233.41	15.62
2264.59	5.19	3364.9131	7.2193	2254.57	8.07	2262.37	5.82
3316.03	3.03	3465.6871	12.5280	3322.36	11.14	3333.58	10.42
3382.99	5.85	3516.7791	37.6617	3404.57	13.38	3416.40	16.94
3595.32	41.03			3596.54	43.47	3599.74	51.48

[a] A scaling factor of 0.955 was employed for vibrational modes with wavenumbers greater than 2000 cm^{-1}, and a scaling factor of 0.985 was employed for all other vibrational modes.

Table C.2: Experimental wavenumbers (cm^{-1}) and intensities (arbitrary unit) of all the photoproducts observed in the solid parahydrogen spectra upon subjecting deuterated α-alanine to 3 hrs of UV-irradiation.

Wavenumber, cm^{-1}	Intensity, abr. unit	Wavenumber, cm^{-1}	Intensity, abr. unit	Wavenumber, cm^{-1}	Intensity, abr. unit
783.2	0.008	1412.3	0.002	2238.3	0.003
911.4	0.011	1704.3	0.004	2250.3	0.002
954.1	0.004	1723.1	0.021	2274.6	0.002
964.4	0.005	1730.1	0.008	2276.7	0.001
967.9	0.009	1734.2	0.004	2278.3	0.028
972.7	0.003	1768.6	0.104	2278.9	0.013
981.2	0.010	1845.0	0.060	2279.1	0.008
982.0	0.012	2019.1	0.004	2323.1	0.001
991.5	0.004	2019.3	0.003	2326.8	0.017
992.3	0.018	2025.1	0.001	2327.4	0.008
1006.6	0.005	2102.5	0.002	2327.6	0.005
1105.9	0.007	2134.4	0.001	2857.3	0.001
1112.1	0.033	2137.6	0.004	2942.2	0.001
1123.3	0.002	2140.3	0.002	3411.2	0.002
1167.8	0.017	2143.0	0.012	3553.7	0.002
1191.4	0.002	2143.7	0.005	3595.5	0.002
1210.3	0.025	2145.4	0.004	3605.0	0.004
1289.2	0.023	2146.0	0.006	3605.5	0.003
1290.7	0.007	2151.1	0.001	3612.1	0.082
1308.4	0.016	2162.2	0.001	3626.9	0.002
1313.3	0.003	2163.7	0.006	3628.8	0.004
1390.5	0.003	2203.4	0.002	3633.5	0.001

Table C.3: Theoretical wavenumbers (cm^{-1}) and intensities ($km \cdot mol^{-1}$) of the seventeen predicted photoproducts of deuterated α-alanine calculated at the B3LYP/aug − cc − pVTZ level of theory in the region of 700 - 4800 cm^{-1}.

N_3H		HCN		DCN		D_3C-C≡N	
Wavenumber[a], cm^{-1}	Intensity, km mol^{-1}	Wavenumber[a], cm^{-1}	Intensity, km mol^{-1}	Wavenumber[a], cm^{-1}	Intensity, km mol^{-1}	Wavenumber[a], cm^{-1}	Intensity, km mol^{-1}
1012.96	141.87	750.15	36.10	1907.35	8.24	829.49	1.45
1643.68	15.71	750.15	36.10	2609.85	28.36	853.84	0.50
1643.68	15.71	2100.80	1.52			853.84	0.50
3313.21	4.02	3289.02	65.81			1046.54	4.65
3426.89	4.39					1046.54	4.65
3426.89	4.39					1114.77	0.22
						2090.09	1.63
						2203.31	0.66
						2203.31	0.66
						2256.46	11.38

Table C.3 Continued

H_2N-CHD-CD_3		D_3C-CD=NH		H_2DC-NH_2		D_3C-NH_2	
Wavenumber[a], cm^{-1}	Intensity, km mol^{-1}	Wavenumber[a], cm^{-1}	Intensity, km mol^{-1}	Wavenumber[a], cm^{-1}	Intensity, km mol^{-1}	Wavenumber[a], cm^{-1}	Intensity, km mol^{-1}
735.00	29.53	744.73	3.57	771.02	134.89	765.02	130.61
800.37	75.02	911.13	4.79	839.85	0.39	791.46	0.46
880.64	0.36	915.72	0.83	1012.67	7.76	868.07	3.12
949.17	22.70	1007.06	43.18	1092.91	10.48	988.03	6.56
980.42	13.37	1014.65	9.11	1231.12	2.03	1061.12	2.70
1058.27	6.09	1048.23	4.40	1321.06	1.65	1083.66	2.83
1065.46	5.52	1051.71	17.79	1354.13	2.64	1136.12	13.30
1075.85	1.63	1124.11	11.09	1486.83	4.31	1241.80	0.00
1153.10	18.17	1292.17	86.97	1642.94	20.87	1640.65	21.15
1205.86	2.79	1678.17	85.37	2138.53	23.82	2064.07	38.96
1339.59	0.45	2070.82	2.19	2889.61	59.05	2161.05	20.54
1384.90	6.77	2152.23	20.32	2922.57	34.77	2177.77	19.17
1633.27	27.60	2168.39	5.68	3376.15	0.53	3376.05	0.50
2065.87	45.71	2195.97	11.75	3447.67	6.12	3447.56	6.40
2075.06	11.42	3250.28	4.05				
2175.98	15.58						
2192.09	14.13						
2904.51	35.10						
3332.00	0.94						
3406.34	0.97						

Table C.3 Continued

HN=C=CD_2		DHC=NH		D_2C=NH		DC≡C-NH_2	
Wavenumber[a], cm^{-1}	Intensity, km mol^{-1}	Wavenumber[a], cm^{-1}	Intensity, km mol^{-1}	Wavenumber[a], cm^{-1}	Intensity, km mol^{-1}	Wavenumber[a], cm^{-1}	Intensity, km mol^{-1}
817.98	64.35	908.96	14.64	866.02	17.01	1051.77	17.35
840.04	0.24	948.34	0.00	867.80	11.47	1181.00	0.07
931.41	0.27	1139.43	60.29	1051.69	47.38	1620.41	25.82
1016.03	228.46	1263.16	62.17	1080.27	1.90	2000.48	70.82
1239.99	0.78	1398.09	3.73	1287.53	60.47	2590.02	137.35
1995.11	368.83	1654.28	22.87	1630.47	21.02	3375.59	17.91
2213.10	76.69	2133.40	39.45	2104.61	38.11	3454.88	40.20
2308.40	0.40	2956.71	26.98	2212.87	22.76		
3316.58	22.29	3277.59	0.54	3277.36	0.52		

Table C.3 Continued

H_2N-˙CD-CD_3 radical		D_3C-CD(-NH_2)-CD(-NH_2)-CD_3		NH_2-CHD-CD_2- CD_2-CDH- NH_2	
Wavenumber[a], cm^{-1}	Intensity, km mol^{-1}	Wavenumber[a], cm^{-1}	Intensity, km mol^{-1}	Wavenumber[a], cm^{-1}	Intensity, km mol^{-1}
751.42	2.92	735.23	51.53	709.88	10.43
811.76	2.11	746.99	0.03	782.99	81.71
884.82	1.49	764.12	105.39	803.69	149.67
934.44	0.89	796.05	28.34	855.45	0.34
1044.57	3.13	830.62	7.42	872.00	3.57
1055.07	4.42	831.58	137.96	885.59	24.01
1097.54	1.43	863.68	10.39	911.93	21.62
1221.33	6.33	903.88	0.11	942.97	14.77
1337.73	39.11	926.93	10.80	966.75	17.01
1624.74	40.45	937.31	0.44	968.78	7.51
2021.65	37.40	1025.85	18.51	1013.77	8.56
2107.29	21.40	1058.54	0.94	1047.65	2.81
2180.87	8.30	1060.66	7.66	1071.13	3.62
2231.16	12.38	1067.55	9.75	1106.57	1.40
3361.76	2.92	1069.84	0.30	1111.80	2.45
3460.83	11.72	1079.47	0.00	1151.56	1.95
		1117.32	12.62	1163.54	28.20
		1145.66	3.91	1234.00	5.93
		1163.45	5.12	1272.68	5.53
		1175.46	20.09	1309.01	0.76
		1263.55	8.78	1322.47	7.96
		1299.21	7.32	1332.42	1.90
		1627.58	35.79	1371.73	4.43
		1632.87	5.55	1633.16	27.65
		2073.80	0.38	1638.51	22.20
		2073.81	19.46	2050.09	37.82
		2109.30	7.72	2078.67	20.89
		2114.42	23.26	2103.56	9.66
		2173.12	1.47	2124.86	12.97
		2174.42	35.24	2141.75	0.69
		2196.52	1.20	2146.12	52.59
		2196.77	18.51	2896.92	8.69
		3330.25	1.45	2903.60	46.38
		3331.21	0.53	3329.86	1.90
		3411.64	1.26	3333.69	0.86
		3412.81	0.32	3402.37	0.87

Table C.3 Continued

HN=C=CD$_2$		DHC=NH		D$_2$C=NH		DC≡C-NH$_2$	
Wavenumber[a], cm^{-1}	Intensity, km mol^{-1}	Wavenumber[a], cm^{-1}	Intensity, km mol^{-1}	Wavenumber[a], cm^{-1}	Intensity, km mol^{-1}	Wavenumber[a], cm^{-1}	Intensity, km mol^{-1}
817.98	64.35	908.96	14.64	866.02	17.01	1051.77	17.35
840.04	0.24	948.34	0.00	867.80	11.47	1181.00	0.07
931.41	0.27	1139.43	60.29	1051.69	47.38	1620.41	25.82
1016.03	228.46	1263.16	62.17	1080.27	1.90	2000.48	70.82
1239.99	0.78	1398.09	3.73	1287.53	60.47	2590.02	137.35
1995.11	368.83	1654.28	22.87	1630.47	21.02	3375.59	17.91
2213.10	76.69	2133.40	39.45	2104.61	38.11	3454.88	40.20
2308.40	0.40	2956.71	26.98	2212.87	22.76		
3316.58	22.29	3277.59	0.54	3277.36	0.52		

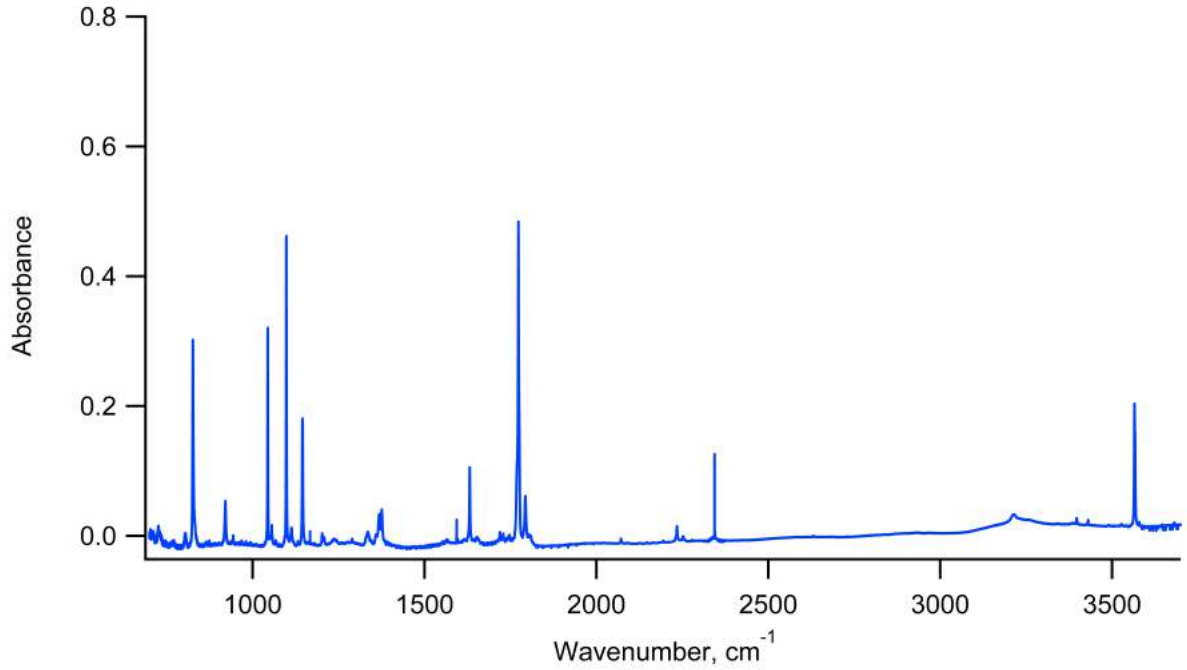

Figure C.1: FTIR spectra of deuterated α-alanine trapped in a solid parahydrogen matrix recorded immediately after deposition and before UV-irradiation (deposition time = 2.5 hrs, flow rate = 5 ccm, T_{sub} = 380 K, T_{dep} = 4 K).

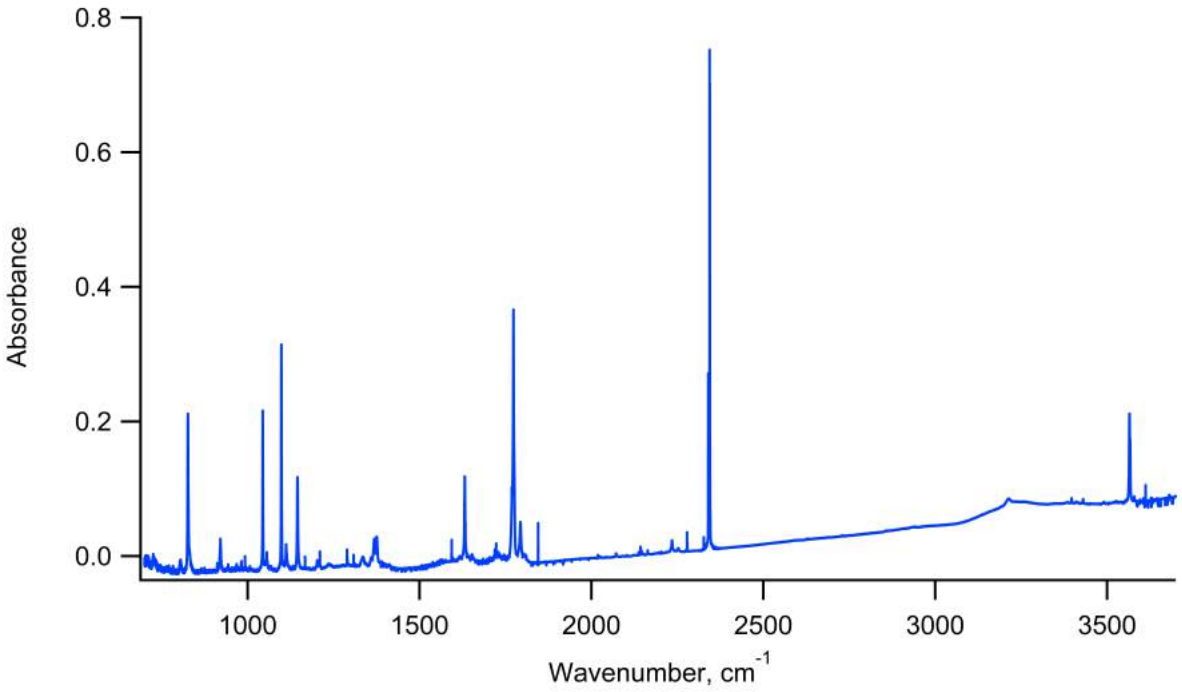

Figure C.2: Solid parahydrogen matrix isolation spectrum of deuterated α-alanine acquired after 3 hrs of UV-irradiation (deposition time = 2.5 hrs, flow rate = 5 ccm, T_{sub} = 380 K, T_{dep} = 4 K).

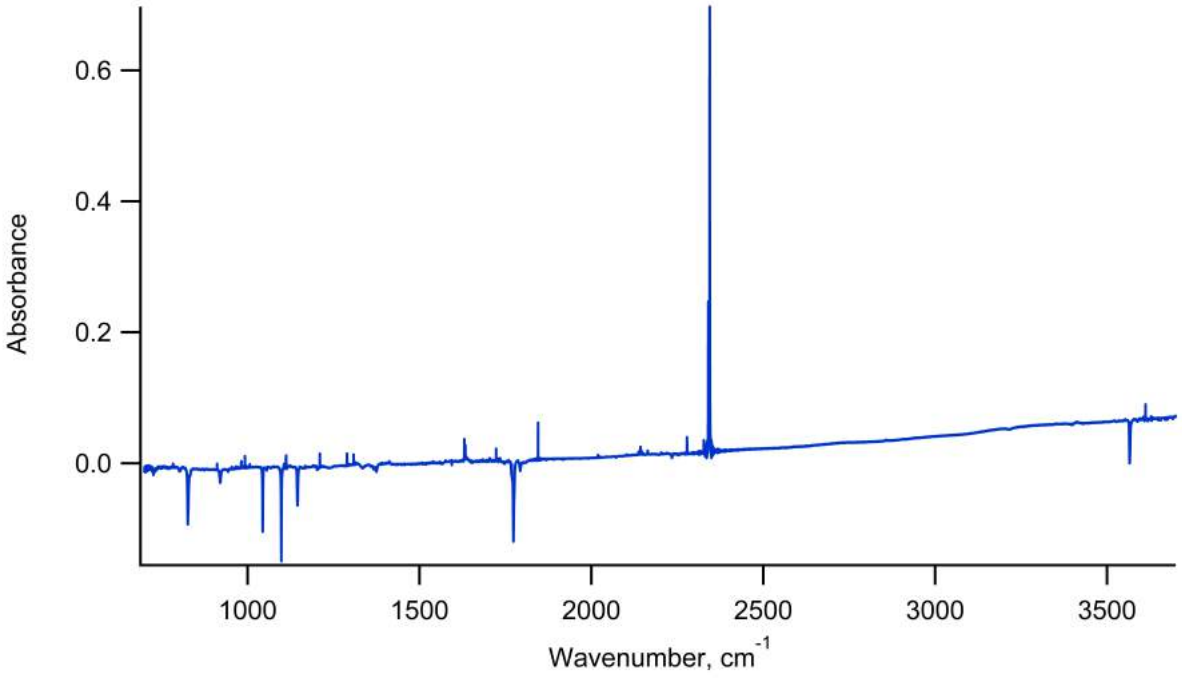

Figure C.3: Difference spectrum of deuterated α-alanine obtained by subtracting the spectrum acquired immediately after deposition (Figure C.1) from the UV-irradiation spectrum after 3 hrs of irradiation (Figure C.2).

Appendix D

Supplementary Material: Study of Amino Acid Zwitterions in Solid Parahydrogen

The following presents raw data from the β-alanine zwitterion studies discussed in Section 5.4. These include full FTIR spectra taken for each procedure.

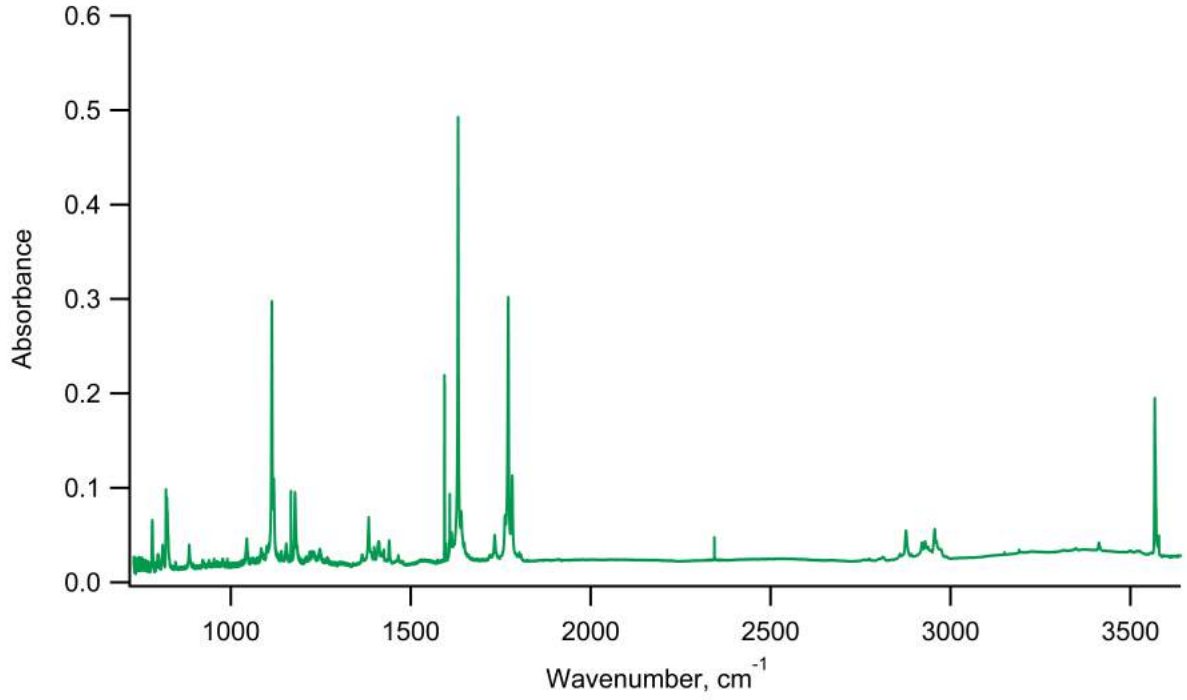

Figure D.1: FTIR spectrum of β-alanine trapped in a solid parahydrogen matrix without water dosage recorded immediately after deposition (deposition time = 1.5 hrs, flow rate = 5 ccm, T_{sub} = 390 K, T_{dep} = 4 K).

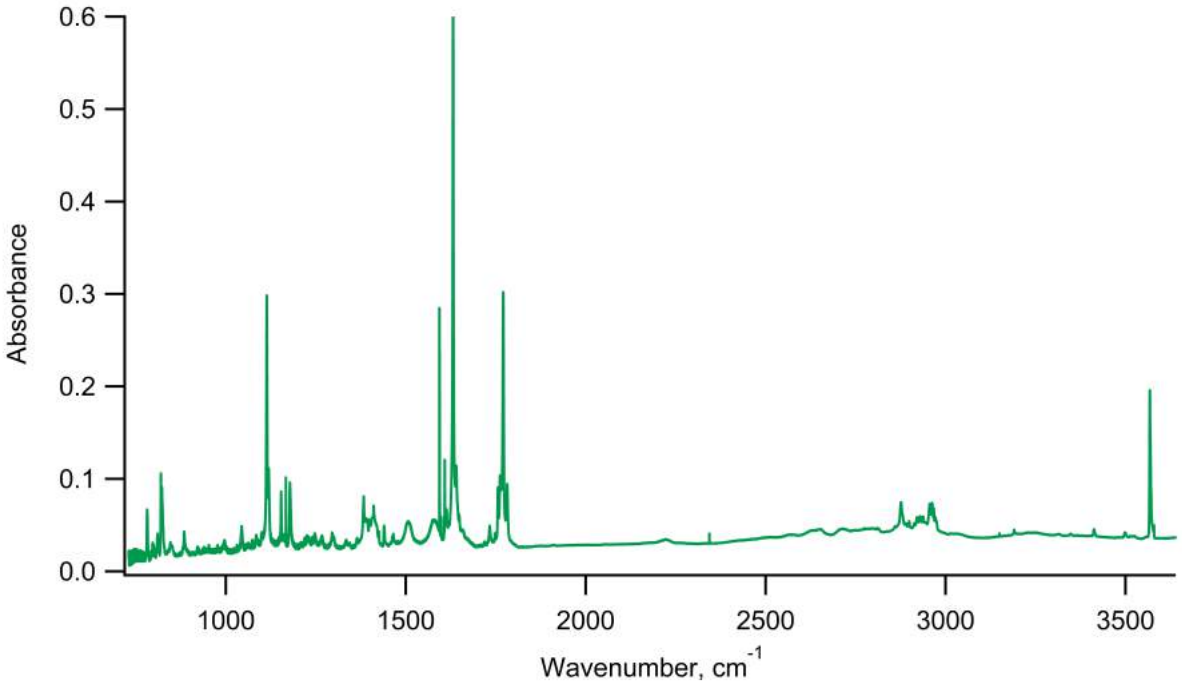

Figure D.2: FTIR spectrum of β-alanine trapped in a solid parahydrogen matrix with 100 ppm water dopant recorded immediately after deposition (deposition time = 1.5 hrs, flow rate = 5 ccm, T_{sub} = 390 K, T_{dep} = 4 K).

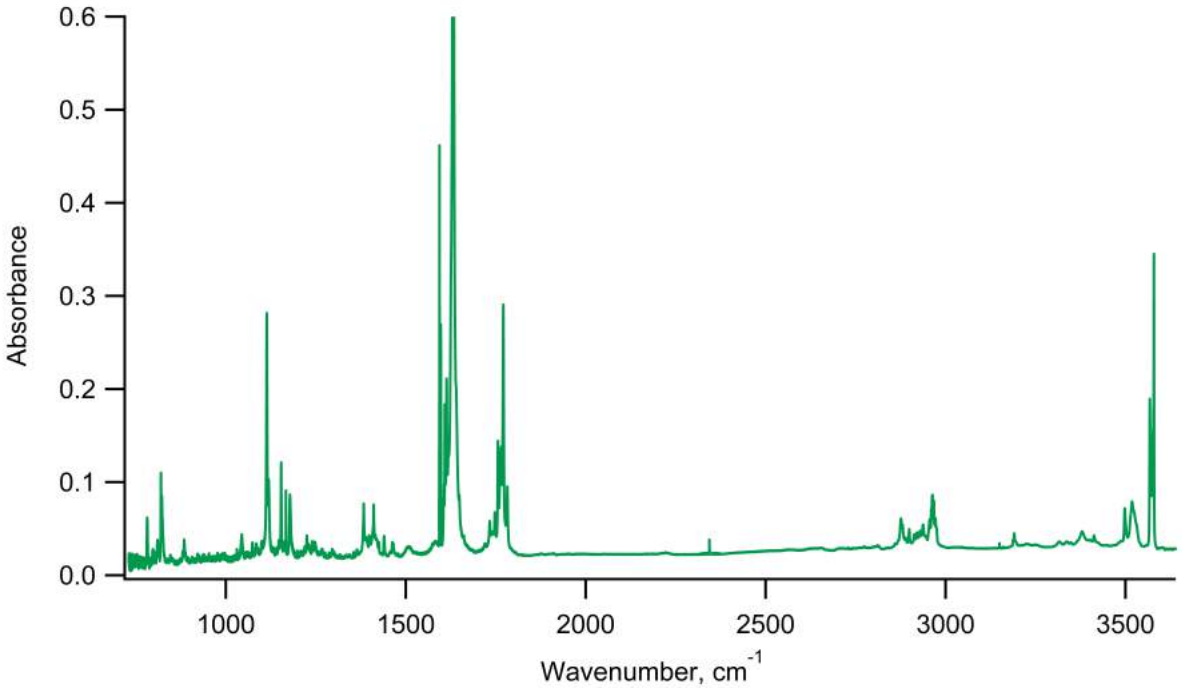

Figure D.3: FTIR spectrum of β-alanine trapped in a solid parahydrogen matrix with 500 ppm water dopant recorded immediately after deposition (deposition time = 1.5 hrs, flow rate = 5 ccm, T_{sub} = 390 K, T_{dep} = 4 K).